České vysoké učení technické v Praze
Fakulta elektrotechnická

Diplomová práce

Daniel Brandtner

Let formací družic: optimální a kooperativní metody řízení

Katedra řídicí techniky

Vedoucí diplomové práce:	Kristian Hengster-Movric, Ph.D.
Studijní program:	Kybernetika a robotika
Studijní obor:	Kybernetika a robotika

Praha 2018

ZADÁNÍ DIPLOMOVÉ PRÁCE

I. OSOBNÍ A STUDIJNÍ ÚDAJE

Příjmení: **Brandtner** Jméno: **Daniel** Osobní číslo: **406383**

Fakulta/ústav: **Fakulta elektrotechnická**

Zadávající katedra/ústav: **Katedra řídicí techniky**

Studijní program: **Kybernetika a robotika**

Studijní obor: **Kybernetika a robotika**

II. ÚDAJE K DIPLOMOVÉ PRÁCI

Název diplomové práce:

Let formací družic: optimální a kooperativní metody řízení

Název diplomové práce anglicky:

Satellite formation flight: optimal and cooperative control approaches

Pokyny pro vypracování:

Seznam doporučené literatury:

[1] Goldstein, Saftko and Pool, Classical Mechanics 3rd Edition, Pearson, 2014.
[2] Moulton, Celestial Mechanics, MacMillan, 1914.
[3] Murray and Dermott, Solar System Dynamics, Cambridge University Press, 1999.
[4] Bryson and Ho, Applied Optimal Control: Optimization, Estimation and Control, Taylor and Francis, 1975.

Jméno a pracoviště vedoucí(ho) diplomové práce:

Kristian Hengster-Movric, Ph.D., katedra řídicí techniky FEL

Jméno a pracoviště druhé(ho) vedoucí(ho) nebo konzultanta(ky) diplomové práce:

Datum zadání diplomové práce: **14.02.2018** Termín odevzdání diplomové práce: **25.05.2018**

Platnost zadání diplomové práce: **30.09.2019**

Kristian Hengster-Movric, Ph.D.	prof. Ing. Michael Šebek, DrSc.	prof. Ing. Pavel Ripka, CSc.
podpis vedoucí(ho) práce	podpis vedoucí(ho) ústavu/katedry	podpis děkana(ky)

III. PŘEVZETÍ ZADÁNÍ

Diplomant bere na vědomí, že je povinen vypracovat diplomovou práci samostatně, bez cizí pomoci, s výjimkou poskytnutých konzultací. Seznam použité literatury, jiných pramenů a jmen konzultantů je třeba uvést v diplomové práci.

. _____
Datum převzetí zadání

_____
Podpis studenta

Acknowledgement

I wish to thank Kristian Hengster-Movric for his patience and support. I am very grateful for the frequent helpful consultations and his constructive feedback at all stages of my work on this thesis.

Declaration I declare that I completed the presented thesis independently and that all used sources are quoted in accordance with the Methodological Guideline for adhering to ethical principles when elaborating an academic final thesis.

Prohlašuji, že jsem předloženou práci vypracoval samostatně a že jsem uvedl veškeré použité informační zdroje v souladu s Metodickým pokynem o dodržování etických principů při přípravě vysokoškolských závěrečných prací.

In Prague, May 25th 2018 Signature
V Praze dne 25. května 2018

Title: Satellite formation flight: optimal and cooperative control approaches

Author: Daniel Brandtner

Abstract: Satellite formations are a novel concept based on cooperation of multiple satellites to achieve a common goal, which is difficult or even impossible for any single satellite to achieve. Thus, a number of smaller, less complex satellites can emulate, or even surpass, the performance of much larger, more complex orbital installations. As a foundation for subsequent control design tasks, a rigorous analysis of orbital dynamics is presented, serving to describe orbit trajectories in a restricted three-body problem with the additional perturbations due to oblateness of the main body included. The goal of the proposed thesis is to develop and compare two approaches to satellite formation control. The first uses open-loop optimal control methods to achieve its goal while minimizing the fuel expended during the manoeuvre. The other merges satellite formations with cooperative control methods, and thus provides robust, flexible control designs. The suitability of both controllers to various real-world applications is discussed and demonstrated in simulations.

Keywords: Satellite Formation Flying; Optimal control; Cooperative control

Název práce: Let formací družic: optimální a kooperativní metody řízení

Autor: Daniel Brandtner

Abstrakt: Let formací družic představuje nový obor kosmického inženýrství založený na spolupráci satelitů za účelem dosažení společného cíle. Uskupení menších, méně složitých satelitů může vyrovnat nebo dokonce překonat výkon mnohem větších, složitějších orbitálních systémů. Důsledná analýza orbitální mechaniky poslouží jako základ pro návrh dvou řídících systémů. Cílem této práce je oba přístupy systematicky popsat a mezi sebou porovnat. První regulátor využívá metody optimálního řízení v otevřené smyčce k dosažení cílového stavu při minimalizaci spotřeby paliva. Druhý návrh vychází z kooperativních metod řízení multiagentních systémů a poskytuje tak formaci robustní a flexibilní řídící systém. Na základě simulací se určí vhodnost obou regulátorů pro různé reálné aplikace.

Klíčová slova: Let formací družic; Optimální řízení; Kooperativní řízení

Contents

List of Figures

List of Tables

Introduction

Traditional space engineering views satellites and spacecraft as single-agent systems, equipped with all the material and resources necessary for completing their mission. Communication is usually only maintained with a ground station, with which the satellite can exchange data and receive instructions.

With recent advancements in communication and propulsion technology and the reducing costs of launchers, more and more satellite installations employ a formation of simpler spacecraft to work on the assigned task in cooperation. Deploying a formation of satellites offers greater flexibility, as individual satellites can be specialized in a specific subtask of the entire mission. Another advantage lies in the robustness of this system as spacecraft can be replaced or repurposed individually if malfunctioning or unnecessary. Numerous applications of this cooperative scheme include astronomical and terrestrial observations, communication, synthetic aperture radar. Examples of various satellite formations currently in orbit or in development are Landsat 7, the Callipso&CloudSat tandem, TechSat-21, Proba-3 and the GPS system. CubeSat are miniaturized satellites that could be deployed in the hundred. This emerging technology could benefit from improved distributed control algorithms.

Setting up and maintaining such formations however requires dedicated control methods. Ideally, these controllers should allow manoeuvres within the formation to be performed autonomously, using only onboard calculations and a minimum of communication. On the other hand, the efficiency of these control schemes should also be an important consideration, as fuel supplies of satellites are limited. In this thesis we explore and compare two alternative controller designs for formation flying, emphasizing their advantages and limitations in solving various problems.

In the first chapter, we derive the dynamics of a single massless particle in a gravitational field using the tools of Lagrangian mechanics. These single-particle dynamics are also relevant for formation flying, as individual satellites are independent of each other when left uncontrolled, thus obeying the single-particle equations of motion introduced in this chapter. Lagrangian mechanics is used to derive the dynamical equations because if offers an elegant way of changing the coordinate systems in which the dynamics is being considered, as well as because of its suitability in describing both the uncontrolled and controlled systems in a similar general way. The simplest model of celestial motion is the Keplerian system, which assumes revolution around a single point mass. This model is expanded to express the gravitational field around an oblate spheroid, as an approximation for a deformed rigid body. As a second type of perturbation to the Keplerian model, a second massive body is added to the system. The masses are no longer fixed in an inertial frame as they revolve around their centre of

mass. For all the described models, distinct orbital trajectories are simulated to illustrate the variety of solutions to the non-linear dynamics.

The second chapter builds on the derived models to introduce a design of an optimal controller, tasked with generating fuel-efficient transfer trajectories between the orbits presented in Chapter 1. This optimal control scheme is also applied in the third chapter, in a different context, to solve to solve various formation reconfiguration tasks. An alternative cooperative control approach is designed using distributed consensus dynamics and implemented on the dynamical models introduced in the first chapter. We adapted the canonical consensus problem by constant offsets in one special state to enable convergence toward a shape-invariant configuration, all in accordance with the general dynamical requirements for consensus. Both control schemes are compared to identify their advantages and examine potential real-world applications.

Chapter 1

Orbital mechanics of a single test body

Celestial mechanics is the branch of astronomy that deals with the motions of natural celestial objects. It has been studied since the dawn of civilization by scholars, philosophers and priests from cultures all over the world. In addition to their religious or philosophical significance, the knowledge of the motion of celestial bodies had practical uses in agriculture, naval navigation and timekeeping and management using calendars.

In the early modern period of European history, advances in mathematics and physics allowed for a more methodical description of celestial dynamics. In reality, it has been in many cases the study of the motion of celestial bodies that lead to major scientific breakthroughs. Galileo Galilei, Johannes Kepler and Isaac Newton are all major figures that helped to lay the foundation of modern science through the study of, among other things, celestial mechanics.

By the 19^{th} century, classical mechanics allowed for a precise model of the dynamics of major bodies in the Solar system. At that time, a new field of study branched from the celestial mechanics field, describing a man-made object, at that time only hypothetical, in motion around celestial bodies. Orbital mechanics not only treats the effects of gravitational forces on a body but also the design of appropriate means of controlling of those spacecraft. In the second half 20^{th} of the century, space missions have been made possible by advancements in many fields of science and technology. Orbital mechanics remains of prime importance in space engineering as even-though the principles of celestial mechanics are considered well understood, spacecraft control remains a complex problem with many considerations to account for.

In this chapter, the uncontrolled dynamics of a satellite in a gravitational field are discussed. First, in Section 1.1, we describe the coordinate systems considered in this thesis. Then, Section 1.2 introduces the mathematical tool of Lagrangian mechanics allowing for an easy derivation of dynamics in different coordinates. The derived equations of motion of satellites are presented in Section 1.3, with the additional effect of the oblateness of the principal massive body and the presence of a second body successively taken into account. Finally, distinct orbital trajectories will be displayed and commented in Section 1.4.

Understanding the natural dynamics of bodies in gravitational fields is essential in the design of control tools treated in subsequent chapters. In the context of

satellite formation flying, the individual dynamics of formation members are also important. As the gravitational interactions between satellites in a formation are negligible compared to the attractions of large celestial bodies, their uncontrolled dynamics are independent and follow the rules laid out in this chapter.

1.1 Coordinate systems

In all task of mechanics, a suitable coordinate system has to be chosen in order to express a system's dynamics. A coordinate system is a set of variables enabling the full and unique description of a position in the configuration space. In this thesis, a three-dimensional space will generally be considered, occasionally reduced to a planar space to simplify or better visualize a situation. Satellites are also considered as point particles and their orientation and rotational dynamics are not addressed. As is discussed in the section introducing Lagrangian mechanics (Section 1.2), this method of deriving equations of motion is independent on the choice of coordinates. We are therefore free to choose a coordinate system that we feel best describes the system.

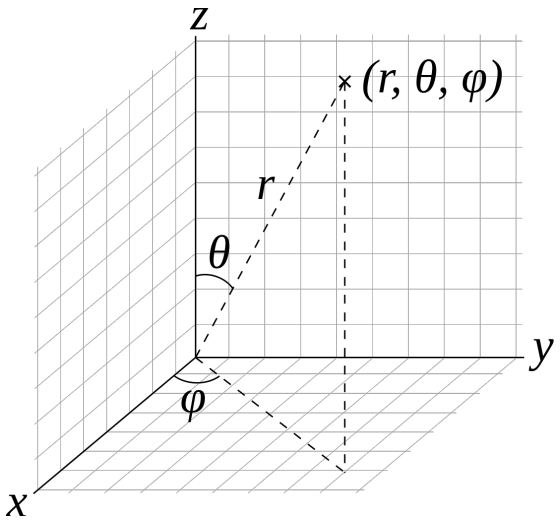

Figure 1.1: Three-dimensional spherical and Cartesian coordinates systems. Figure taken from `https://en.wikipedia.org/wiki/Spherical_coordinate_system`

A position vector given in the Cartesian coordinate system (x,y,z) denotes its distance from three planes defined by three mutually perpendicular axis (Figure 1.1). The Cartesian coordinates are useful as the kinetic energy expressed in them are not dependent on the position.

Spherical coordinates are defined by the triplet (r,ϑ,φ). r is the norm of the position vector, φ the angle between the x-axis and the projection of the vector on the xy plane and ϑ is the angle between the z-axis and the position vector. Spherical coordinates are usually more informative than Cartesian ones as orbital mechanics deal with trajectories of particles subject to central forces. By placing the origin of the coordinates at the source of the central force field, the equations of motion become more readable and allow a better understanding of the motion. The transformations between positions and velocities in the spherical

and Cartesian coordinates can be written as

$$\begin{bmatrix} x \\ \dot{x} \\ y \\ \dot{y} \\ z \\ \dot{z} \end{bmatrix} = \begin{bmatrix} r\cos\varphi\sin\vartheta \\ \dot{r}\cos\varphi\sin\vartheta - \dot{\varphi}r\sin\varphi\sin\vartheta + \dot{\vartheta}r\cos\varphi\cos\vartheta \\ r\sin\varphi\sin\vartheta \\ \dot{r}\sin\varphi\sin\vartheta + \dot{\varphi}r\cos\varphi\sin\vartheta + \dot{\vartheta}r\cos\vartheta\sin\varphi \\ r\cos\vartheta \\ \dot{r}\cos\vartheta - \dot{\vartheta}r\sin\vartheta \end{bmatrix} \tag{1.1a}$$

$$\begin{bmatrix} r \\ \dot{r} \\ \vartheta \\ \dot{\vartheta} \\ \varphi \\ \dot{\varphi} \end{bmatrix} = \begin{bmatrix} \sqrt{x^2+y^2+z^2} \\ \frac{\dot{x}x+\dot{y}y+\dot{z}z}{\sqrt{x^2+y^2+z^2}} \\ \cos^{-1}\frac{z}{\sqrt{x^2+y^2+z^2}} \\ \frac{z(\dot{x}x+\dot{y}y)-\dot{z}\left(x^2+y^2\right)}{\sqrt{x^2+y^2}(x^2+y^2+z^2)} \\ \tan^{-1}\frac{y}{x} \\ \frac{\dot{y}x-\dot{x}y}{x^2+y^2} \end{bmatrix} \tag{1.1b}$$

In order to model the dynamics of the particle, a state space vector is introduced to combine the position and velocity coordinates:

$$\boldsymbol{x} = \begin{bmatrix} x_1 \\ x_2 \\ x_3 \\ x_4 \\ x_5 \\ x_6 \end{bmatrix} = \begin{bmatrix} r \\ \dot{r} \\ \vartheta \\ \dot{\vartheta} \\ \varphi \\ \dot{\varphi} \end{bmatrix} \tag{1.2}$$

1.1.1 Hill's system

As we are interested in the relative motion of a massless particle with regards to massive bodies, it is a good idea to choose a reference frame where the bodies are fixed. This is trivial in case of a single massive body, where the origin of the coordinate system is placed at the centre of the body. In this thesis, however, we also treat the dynamics of a particle in the gravitational field of two mass points. These principal bodies are assumed to revolve around their common centre of mass on circular trajectories at a constant angular velocity Ω. By rotation of the frame around the centre of mass with the same angular velocity, the two bodies will appear as fixed. In addition, all distances are rescaled by the inverse of the constant distance between the bodies d so that this distance becomes 1.

$$x \to \frac{x}{d} \qquad y \to \frac{y}{d} \qquad z \to \frac{z}{d} \tag{1.3}$$

Masses m_1 and m_2 are also rescaled by introducing a dimensionless reduced mass μ.

$$\mu = \frac{m_2}{m_1+m_2} \qquad \begin{matrix} m_1 \to 1-\mu \\ m_2 \to \mu \end{matrix} \tag{1.4}$$

In the literature [9], such a two-body system described in a co-rotating frame is referred to as the Hill's system. The origin of this frame is usually placed at

the centre of mass. Its z-axis is set to be aligned to the rotation vector of the frame, meaning the xy plane coincides with the revolution plane of the bodies. We call this plane the *principal plane* of the system. The x-axis is aligned with the *principal axis*, the line joining the centre of mass to both bodies. The positions of the bodies and the centre of mass in Cartesian coordinates in this frame are:

$$\boldsymbol{r}_1 = \begin{bmatrix} -\mu \\ 0 \\ 0 \end{bmatrix} \qquad \boldsymbol{r}_{CM} = \begin{bmatrix} 0 \\ 0 \\ 0 \end{bmatrix} \qquad \boldsymbol{r}_2 = \begin{bmatrix} 1-\mu \\ 0 \\ 0 \end{bmatrix} \tag{1.5}$$

In this thesis, however, we will mostly be working with spherical coordinates centred at one of the bodies. The chosen body is called the *principal body* and is the one around which most orbits and transfers in this thesis will be performed. As mentioned above, orbit trajectories in spherical coordinates are generally more informative than when expressed in Cartesian ones. The bodies and centre of mass in spherical coordinates centred at the principal body in the co-rotating frame are located at

$$\boldsymbol{r}_1 = \begin{bmatrix} 0 \\ \pi/2 \\ 0 \end{bmatrix} \qquad \boldsymbol{r}_{CM} = \begin{bmatrix} \mu \\ \pi/2 \\ 0 \end{bmatrix} \qquad \boldsymbol{r}_2 = \begin{bmatrix} 1 \\ \pi/2 \\ 0 \end{bmatrix} \tag{1.6}$$

This rotating frame is however not the only useful frame of reference. Because of its non-inertiallity, it is often not intuitive to interpret the resulting motion. For this reason, all generated orbits in the Hill's system will also be displayed it two other frames Figure 1.2:

- **Rotating frame** centred at the principal. As explained above, both bodies remain fixed on the x-axis on positions given by (1.6).
- Non-rotating **inertial frame** centred at the centre of mass. Both bodies orbit around it on circular trajectories. This frame allows visualizing the three-body system from the point of view of an observer immobile with regards to the centre of mass. In realistic applications, a sidereal frame fixed by distant stars is used, as their motion can be neglected.
- **Non-rotating frame** centred around the main body. Second body and centre of mass orbit around it with constant velocity. This frame allows visualizing the three-body system from the point of view of an observer located on the main body.

Problems of celestial mechanics involving two massive bodies usually assume they orbit their common centre of mass on circular trajectories. Circular orbits are however only a special case of more general elliptic trajectories. If the elliptic case is considered, the Hill's coordinate system such as we defined it would not be applicable, as both the angular velocity $\Omega(t)$ and the distance between bodies $d(t)$ are time-variant. To overcome this, we can introduce a new *elliptic Hill's system* frame of reference that rotates with both bodies at their immediate angular velocity. The rescaling (1.3) is likewise performed using the instantaneous value of $d(t)$. In the resulting coordinate system both bodies are still fixed on their old positions (1.5) and (1.6), but the distance scale varies as a function of time as the bodies swing away and toward each other in the inertial frame. Dynamics in this elliptic Hill's system will be derived in Section 1.3.4.

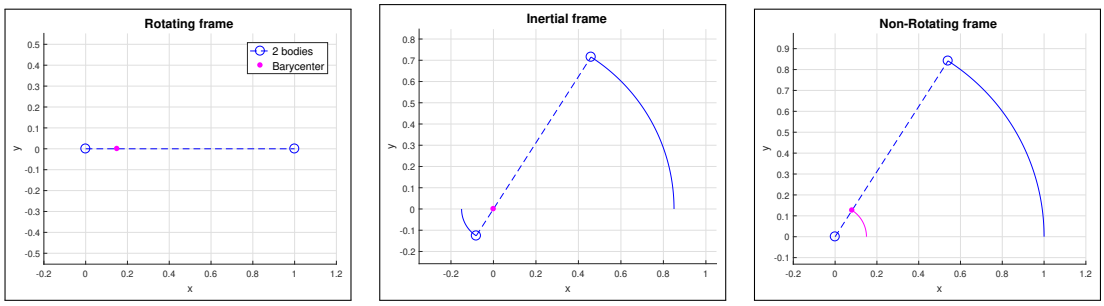

Figure 1.2: Frames used in this thesis to depict orbits in the Hill's system.

1.1.2 LVLH coordinate system

When dealing with satellite formation flying, it is useful to work in a reference frame centred at one of the satellites. If the formation has a leader, the origin is most often placed at its position. Placing the reference frame is this way allows to express the relative dynamics of the formation, which is advantageous if a certain relative formation is to be achieved or maintained. The standard way to orient a coordinate system centred at an orbiting particle is the Local Vertical Local Horizontal method, abbreviated as LVLH. Using this scheme, the z-axis is directed towards the body, the x-axis is in the direction of the movement and the y-axis perpendicular to the orbital plane according to the right-hand rule. A schematic of this coordinate system is displayed on Figure 1.3.

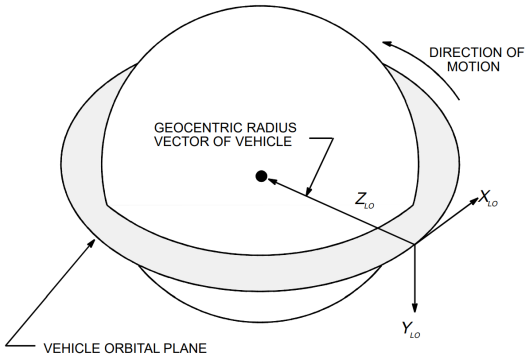

Figure 1.3: Sketch of the LVLH reference frame. Figure taken from `http://www.asi.org/adb/04/02/00/iss-coordinate-systems.pdf`

The LVLH coordinate system is used mostly on particles on circular Keplerian orbits. As the distance to the body is constant and the orientation of one of the axis is set toward it, the body remains fixed in the LVLH frame. This coordinate system is similar to the Hill's system, with two points of interest fixed by the frame's rotation, with only the location of the origin and orientation of the axis being different. As a result, the equations of motion of follower particles in a leader-centric LVLH frame can be derived in a similar manner as the dynamics of a particle in the Hill's system as treated in Section 1.3.3. The only difference is the fact that the mass of the leader satellite is neglected.

If the particle's orbit is elliptic, however, the position of the body in this frame will fluctuate between two extremes on the z-axis. Moreover, the x-axis will no longer be aligned with the velocity vector. A solution to this issue could be the

rescaling of all distances by the current body-leader distance. Similarly to the elliptic Hill's system, this new *pulsating LVLH* coordinate system would have the same properties as in the circular case, the origin at the leader, the body fixed on the z-axis, but the units of distance would be time-variant. The dynamics in this pulsating LVLH frame are derived along the same lines as in the case of the elliptic Hill's system in Section 1.3.4.

The LVLH coordinate system becomes however less useful as perturbations to the Keplerian model are introduced. If a non-spherical body is accounted for, dynamics derived in the particle-centred frame would be time-dependent, as the shape of the gravitational field would vary throughout the orbit. If solving a three-body problem, fixing the origin of the coordinate system to the particle would make the second massive body move on strange trajectories, which would be impractical.

Because of these reasons, we will not solve the satellite formation problem in Chapter 3 in the LVLH reference frame. We will however use this leader-centred coordinate system to display the resulting trajectories of particles, as motions within a formation are usually more informative in relative rather than in absolute terms.

1.2 Lagrangian mechanics

Lagrangian mechanics is a reformulation of classical Newtonian mechanics allowing the derivation of equations of motion of a system from the expressions for its potential and kinetic energy.

It can be derived from variational principle, which states that the functional action of a system observed between time t_i and t_f is at an extrema value.

$$S = \int_{t_i}^{t_f} L\left(\boldsymbol{q}\left(t\right), \dot{\boldsymbol{q}}\left(t\right)\right) \mathrm{d}t \tag{1.7}$$

where $\boldsymbol{q}\left(t\right)$ is a doubly differentiable time-varying state vector in some arbitrary coordinates and

$$L = T - V \tag{1.8}$$

is the Lagrangian function calculated form the potential V and kinetic energy T. If the action (1.7) is at an extrema, it hold true for a small deviation δ that

$$\delta \int_{t_i}^{t_f} L \mathrm{d}t = 0 \tag{1.9}$$

Together, $\boldsymbol{q}\left(t\right)$ and $\dot{\boldsymbol{q}}\left(t\right)$ specify the trajectory in the configuration space undertaken by the system in the time interval (t_i,t_f). A second trajectory between the initial and final states can be obtained by adding a small deviation from the original:

$$\begin{array}{lcl} \boldsymbol{q}\left(t\right) & \rightarrow & \boldsymbol{q}\left(t\right) + \epsilon\delta\boldsymbol{q}\left(t\right) \\ \dot{\boldsymbol{q}}\left(t\right) & \rightarrow & \dot{\boldsymbol{q}}\left(t\right) + \epsilon\delta\dot{\boldsymbol{q}}\left(t\right) \end{array} \tag{1.10}$$

with the initial and final positions conserved:

$$\begin{array}{l} \delta\boldsymbol{q}\left(t_i\right) = 0 \\ \delta\boldsymbol{q}\left(t_f\right) = 0 \end{array} \tag{1.11}$$

The expression (1.9) can be rewritten as

$$\begin{aligned}\delta\int_{t_i}^{t_f} L\mathrm{d}t &= \int_{t_i}^{t_f}\delta L\mathrm{d}t = \int_{t_i}^{t_f}\left(\frac{\partial L}{\partial \boldsymbol{q}}\delta\boldsymbol{q}+\frac{\partial L}{\partial \dot{\boldsymbol{q}}}\delta\dot{\boldsymbol{q}}\right)\mathrm{d}t \\ &= \int_{t_i}^{t_f}\left(\frac{\partial L}{\partial \boldsymbol{q}}\delta\boldsymbol{q}+\frac{\mathrm{d}}{\mathrm{d}t}\left(\frac{\partial L}{\partial \dot{\boldsymbol{q}}}\delta\boldsymbol{q}\right)-\left(\frac{\mathrm{d}}{\mathrm{d}t}\frac{\partial L}{\partial \dot{\boldsymbol{q}}}\right)\delta\boldsymbol{q}\right)\mathrm{d}t \\ &= \int_{t_i}^{t_f}\left(\frac{\partial L}{\partial \boldsymbol{q}}-\frac{\mathrm{d}}{\mathrm{d}t}\frac{\partial L}{\partial \dot{\boldsymbol{q}}}\right)\delta\boldsymbol{q}\mathrm{d}t+\int_{t_i}^{t_f}\frac{\mathrm{d}}{\mathrm{d}t}\left(\frac{\partial L}{\partial \dot{\boldsymbol{q}}}\delta\boldsymbol{q}\right)\mathrm{d}t\end{aligned} \tag{1.12}$$

The second term vanishes as the variations in position are set to zero at the extremes of the trajectory (1.11):

$$\int_{t_i}^{t_f}\frac{\mathrm{d}}{\mathrm{d}t}\left(\frac{\partial L}{\partial \dot{\boldsymbol{q}}}\delta\boldsymbol{q}\right)\mathrm{d}t = \frac{\partial L}{\partial \dot{\boldsymbol{q}}}\delta\boldsymbol{q}\left(t_f\right)-\frac{\partial L}{\partial \dot{\boldsymbol{q}}}\delta\boldsymbol{q}\left(t_i\right)=0 \tag{1.13}$$

And for the first term to equal zero, the expression between the parenthesis must be zero, leading to the well-known formula for the Lagrange equation:

$$\frac{\mathrm{d}}{\mathrm{d}t}\frac{\partial L}{\partial \dot{\boldsymbol{q}}}-\frac{\partial L}{\partial \boldsymbol{q}}=0 \tag{1.14}$$

By solving (1.14) successively for every coordinate q_i, the equations motion in the coordinate system $\boldsymbol{q}$ are obtained. This enables to easily express the dynamics of a system in different coordinate systems, as it is usually much simpler to convert the Lagrangian to the new coordinates than the equations of motion themselves. This is a useful property as, in this chapter, we will derive the dynamics of orbital systems in different coordinate frames.

1.3 Derivation of the equations of motion

In this section, we will use the tools of Lagrangian mechanics introduced in Section 1.2 to derive the dynamics for a massless particle in a gravitational field. First, the motion will be considered only around a single point mass. Then, the oblateness of the principal body is defined and taken into account. Finally, we will describe the orbital mechanics of a particle in the three-body Hill's system.

1.3.1 Two body Keplerian system

The simplest model of orbital motion assumes a massless particle in the gravitational field of a single mass point. The only interaction between them that is considered is the gravitational attractive central force exerted by the massive body on the particle. Influences of additional bodies or due to the shape of the primary body as well as collision or atmospheric interference scenarios are disregarded.

With an inertial coordinate system centred at the mass point, equation motion of the mass-less particle can be derived from the Lagrange equations (1.14). To constitute the Lagrangian function (1.8), we need the expressions for the potential and kinetic energy. This section will successively present the derivations of both functions, before combining them in the Lagrangian and deriving the particle's dynamics from it.

1.3.1.1 Gravitational potential

Isaac Newton's second law of motion gives us the effect of an external force F on a body of mass m:

$$\frac{\mathrm{d}^2\boldsymbol{r}}{\mathrm{d}t^2} = \frac{\boldsymbol{F}}{m} \tag{1.15}$$

The external force considered in orbital mechanics is the gravitational force, an attractive force F_{21} excerted by a point mass m_1 position at r_1 on a point mass m_2 at r_2:

$$\boldsymbol{F}_{21} = G\frac{m_1 m_2 \left(\boldsymbol{r}_1 - \boldsymbol{r}_2\right)}{\left|\boldsymbol{r}_1 - \boldsymbol{r}_2\right|^3} \tag{1.16}$$

where $G = 6.67408 \cdot 10^{-11} m^3 kg^{-1} s^{-2}$ is the gravitational constant. It is important to note that the correctness of Newton's laws of motion is orbital mechanics is restricted to systems with velocities much smaller than the speed of light and masses small enough that their gravitational fields are weak and stationary. If these conditions are not met, corrections from the theory of general relativity have to be taken into account to accurately model the system.

The motion of the two bodies can then be obtained by inserting (1.16) into (1.15):

$$\frac{\mathrm{d}^2\boldsymbol{r}_1}{\mathrm{d}t^2} = G\frac{m_2 \left(\boldsymbol{r}_2 - \boldsymbol{r}_1\right)}{\left|\boldsymbol{r}_2 - \boldsymbol{r}_1\right|^3} \tag{1.17a}$$

$$\frac{\mathrm{d}^2\boldsymbol{r}_2}{\mathrm{d}t^2} = G\frac{m_1 \left(\boldsymbol{r}_1 - \boldsymbol{r}_2\right)}{\left|\boldsymbol{r}_1 - \boldsymbol{r}_2\right|^3} \tag{1.17b}$$

As the mutual interactions between the two bodies are of interest to us, we can define the centre of mass $\boldsymbol{R}$, the total mass M and the relative position $\boldsymbol{r}$ as:

$$\boldsymbol{R} = \frac{m_1\boldsymbol{r}_1 + m_2\boldsymbol{r}_2}{m_1 + m_2} \tag{1.18a}$$

$$M = m_1 + m_2 \tag{1.18b}$$

$$\boldsymbol{r} = \boldsymbol{r}_1 - \boldsymbol{r}_2 \tag{1.18c}$$

Solving these equations for $\boldsymbol{r}_1$ and $\boldsymbol{r}_2$ yields

$$\boldsymbol{r}_1 = \boldsymbol{R} - \frac{m_2}{M}\boldsymbol{r} \tag{1.19a}$$

$$\boldsymbol{r}_2 = \boldsymbol{R} + \frac{m_2}{M}\boldsymbol{r} \tag{1.19b}$$

By taking the second derivative of these new variables and using (1.17b) we can decouple the system into the motion of the centre of gravity and the mutual motion of the two bodies.

$$\begin{aligned}\frac{\mathrm{d}^2\boldsymbol{R}}{\mathrm{d}t^2} &= \frac{m_1}{M}\frac{\mathrm{d}^2\boldsymbol{r}_1}{\mathrm{d}t^2} + \frac{m_2}{M}\frac{\mathrm{d}^2\boldsymbol{r}_2}{\mathrm{d}t^2} \\ &= G\frac{m_1 m_2 \left(\boldsymbol{r}_2 - \boldsymbol{r}_1\right)}{M\left|\boldsymbol{r}_2 - \boldsymbol{r}_1\right|^3} + G\frac{m_2 m_1 \left(\boldsymbol{r}_1 - \boldsymbol{r}_2\right)}{M\left|\boldsymbol{r}_1 - \boldsymbol{r}_2\right|^3} = \boldsymbol{0}\end{aligned} \tag{1.20}$$

$$\frac{\mathrm{d}^2\boldsymbol{r}}{\mathrm{d}t^2} = \frac{\mathrm{d}^2\boldsymbol{r}_2}{\mathrm{d}t^2} - \frac{\mathrm{d}^2\boldsymbol{r}_1}{\mathrm{d}t^2} = G\frac{m_1\left(\boldsymbol{r}_1 - \boldsymbol{r}_2\right)}{\left|\boldsymbol{r}_1 - \boldsymbol{r}_2\right|^3} - G\frac{m_2\left(\boldsymbol{r}_2 - \boldsymbol{r}_1\right)}{\left|\boldsymbol{r}_2 - \boldsymbol{r}_1\right|^3} = -\frac{GM}{\left|\boldsymbol{r}\right|^3}\boldsymbol{r} \tag{1.21}$$

We see from equation (1.20) that the gravitational forces from the two bodies always cancel out at their mutual centre of mass, which has a uniform velocity. The centre of mass is, therefore, an ideal candidate to be the origin of an inertial coordinate system.

The gravitational potential per unit mass of the gravitational field is derived from (1.21)

$$V\left(\mathbf{r}\right) = \int -\frac{GM}{\left|\boldsymbol{r}\right|^3}\boldsymbol{r}\mathrm{d}\boldsymbol{r} = -\frac{GM}{\left|\boldsymbol{r}\right|} \tag{1.22}$$

The problem can be simplified in case the mass of one body m_2 is negligible to the mass of the other m_1. This is a justified assumption when studying the motion of small bodies (i.e. man-made satellites or small asteroids) in the vicinity of a planet or a star. We can then approximate the above equations as follows:

$$\mathbf{R} = \mathbf{r_1} \tag{1.23a}$$
$$M = m_1 \tag{1.23b}$$
$$\mathbf{r} = \mathbf{r_2} \tag{1.23c}$$

The principal body m_1 is chosen as origin of the coordinate system, $\boldsymbol{r}$ is the location of massless particle in this coordinate system. $|\boldsymbol{r}|$, the distance from the particle to the body, can be expressed in spherical or Cartesian coordinates described in Section 1.1:

$$|\boldsymbol{r}| = \sqrt{x^2 + y^2 + z^2} = r \tag{1.24}$$

Before deriving the particle dynamics, it is useful to normalize the system so that certain quantities become dimensionless:

$$G = 1 \qquad M = 1 \tag{1.25}$$

The final expression in Cartesian and spherical coordinates is obtained by inserting (1.25) and (1.24) into (1.22):

$$V = -\frac{1}{\sqrt{x^2 + y^2 + z^2}} = -\frac{1}{r} \tag{1.26}$$

1.3.1.2 Kinetic energy

The equation for the kinetic energy per unit mass in spherical coordinates can easily be derived from the expression in Cartesian coordinates using the transformation (1.1).

$$T = \frac{1}{2}|\dot{\boldsymbol{v}}|^2 = \frac{1}{2}\left(\dot{x}^2 + \dot{y}^2 + \dot{z}^2\right) = \frac{1}{2}\left(\dot{r}^2 + r^2\dot{\vartheta}^2 + r^2\sin^2\vartheta\dot{\varphi}^2\right) \tag{1.27}$$

1.3.1.3 Particle dynamics

The Lagrangian function is obtained by combining the expressions for the potential (1.26) and kinetic (1.27) energy per unit mass.

$$L = T - V = \frac{1}{2}\left(\dot{r}^2 + r^2\dot{\vartheta}^2 + r^2\sin^2\vartheta\dot{\varphi}^2\right) + \frac{1}{r} \tag{1.28}$$

The equations of motion of a particle in a gravitational central force field can be derived from the Lagrange equation (1.14) using the above Lagrangian. Successively solving the Lagrange equation for all three spherical coordinates gives the expression for their accelerations:

$$\ddot{r} = r\dot{\vartheta}^2 - \frac{1}{r^2} + r\sin^2\vartheta\dot{\varphi}^2 \tag{1.29a}$$

$$\ddot{\vartheta} = -2\frac{\dot{r}}{r}\dot{\vartheta} + \cos\vartheta\sin\vartheta\dot{\varphi}^2 \tag{1.29b}$$

$$\ddot{\varphi} = -2\left(\frac{\dot{r}}{r} + \dot{\vartheta}\frac{\cos\vartheta}{\sin\vartheta}\right)\dot{\varphi} \tag{1.29c}$$

These dynamics can be also expressed by the derivative of the state vector (1.2):

$$\dot{\boldsymbol{x}} = \begin{bmatrix} \dot{x}_1 \\ \dot{x}_2 \\ \dot{x}_3 \\ \dot{x}_4 \\ \dot{x}_5 \\ \dot{x}_6 \end{bmatrix} = \begin{bmatrix} x_2 \\ x_1x_4^2 - \frac{1}{x_1^2} + x_1\sin^2 x_3x_6^2 \\ x_4 \\ -2\frac{x_2}{x_1}x_4 + \cos x_3\sin x_3x_6^2 \\ x_6 \\ -2\left(\frac{x_2}{x_1} + x_4\frac{\cos x_3}{\sin x_3}\right)x_6 \end{bmatrix} \tag{1.30}$$

1.3.2 Oblateness of the main body

The model proposed in Section 1.3.1 describes the motion of a massless particle in the gravitational field of a point mass. If the orbit of the particle is far enough from the body to ensure no collision or atmospheric perturbation occur, the point mass is equivalent to a spherical body with a uniform distribution of density (or a density of radial variation). In reality, celestial bodies are never perfect spheres. A wide array of internal and external forces deform them into irregular rigid bodies of uneven mass distribution and their gravitational field is impacted by it. In this section, we will include the oblateness of the body into the equations of motion of a particle in orbit around it. For most large rotating celestial bodies, oblateness, the flattening of the body at the poles, describes the principal deviation from a spherical shape.

1.3.2.1 Gravitational potential

The mutual gravitational potential between two bodies has been derived in Section 1.3.1. If we consider the principal body represented by a distribution of mass points m_i and the second by a single mass point M (Figure 1.4), the

potential can be rewritten:

$$V = -\sum_i \frac{GMm_i}{r_i} = -\sum_i \frac{GMm_i}{r\sqrt{1 + \left(\frac{r'_i}{r}\right)^2 - 2\frac{r'_i}{r}\cos\psi_i}} \tag{1.31}$$

where r_i is the distance from the mass point m_i to M, r'_i is the distance from m_i to the centre of mass of all mass points m_i, r is the distance between this centre of mass and the point M and ψ_i is the angle between $\boldsymbol{r}$ and $\boldsymbol{r'_i}$ according to Figure 1.4.

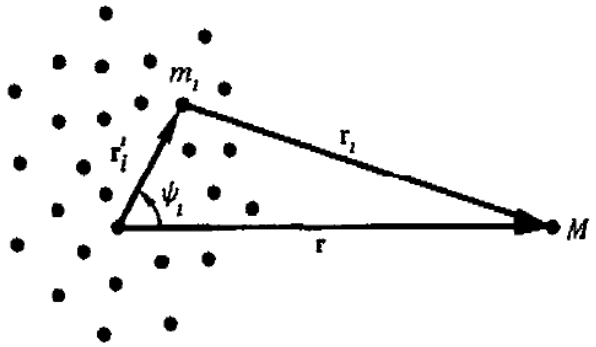

Figure 1.4: Sketch of a two body system where one body is represented by multiple mass points m_i. Figure from [2].

As the reciprocal of the square root term in (1.31) is a generating function for Legendre polynomials, we can expand the above expression in terms of its Legendre polynomials:

$$V = -\frac{GM}{r}\sum_i \sum_{n=0} m_i \left(\frac{r'_i}{r}\right)^n P_n\left(\cos\psi_i\right) \tag{1.32}$$

where $P_n\left(\cos\psi_i\right)$ are Legendre polynomials of $\cos\psi_i$. For reference, the first three Legendre polynomials are:

$$P_0\left(x\right) = 1 \qquad P_1\left(x\right) = x \qquad P_2\left(x\right) = \frac{1}{2}\left(3x^2 - 1\right) \tag{1.33}$$

In the case of a perfectly spherical principal body with a radial variation of density, all but the zero-order Legendre polynomial P_0 cancel out and vanish. The contribution of this lowest-order term polynomial to the potential corresponds to the formula (1.22) derived in the previous section.

$$V_0 = -\frac{GM}{r}\sum_i m_i \tag{1.34}$$

With deviations of a body from a sphere, some of the terms corresponding to higher polynomials of (1.32) become non-zero. Their amplitude decreases however with increasing order because of $\left(\frac{r'_i}{r}\right)^n$ and $r'_i << r$. In this thesis, we consider the first non-zero higher Legendre polynomial order as a sufficient approximation.

The first-order term P_1 is skipped since it is always zero.

$$V_1 = -\frac{GM}{r^2} \sum_i \sum_{n=0} m_i r'_i \cos\psi_i = -\frac{GM}{r^3} \boldsymbol{r} \sum_i \sum_{n=0} m_i \boldsymbol{r'_i} = 0 \tag{1.35}$$

by definition of the centre of mass.

The second-order term P_2 is retained as the first non-vanishing higher order Legendre polynomial, its contribution is given by

$$V_2 = -\frac{GM}{r} \sum_i m_i \left(\frac{r'_i}{r}\right)^2 P_2\left(\cos\psi_i\right) = -\frac{GM}{2r^3} \sum_i m_i r_i'^2 \left(3\cos^2\psi_i - 1\right) \tag{1.36}$$

The potential function (1.31) expanded to the second order Legendre polynomial is obtained by combining (1.34), (1.35) and (1.36) and then rewritten in terms of moments of inertia using tensor manipulation.

$$\begin{aligned} V =& -\frac{GM}{r} \sum_i m_i - \frac{GM}{2r^3} \sum_i m_i r_i'^2 \left(3\cos^2\psi_i - 1\right) \\ =& -\frac{GMm}{r} + \frac{GM}{2r^3} \left(3I_r - \mathrm{Tr}\boldsymbol{I}\right) \end{aligned} \tag{1.37}$$

where $m = \sum_i m_i$ is the mass of the principal body, $\boldsymbol{I}$ is the moment of inertia tensor and I_r represents the moment of inertia about the vector $\boldsymbol{r}$.

As stated above, the body is assumed oblate, thus with a rotational symmetry along the third, polar, axis, so that $I_1 = I_2$. With α, β and γ the direction cosines of $\boldsymbol{r}$ relative to this principal axis of the body, the moment of inertia I_r becomes

$$I_r = I_1\alpha^2 + I_2\beta^2 + I_3\gamma^2 = I_1 + \left(I_3 - I_1\right)\gamma^2 \tag{1.38}$$

Additionally, if the polar axis of the oblate body is aligned with the zenith direction of a spherical coordinate systems

$$\gamma = \cos\vartheta \tag{1.39}$$

which can be established without loss of generality by choosing the appropriate coordinate system.

Inserting Equations (1.38) and (1.39) into (1.37) gives the mutual gravitational potential between a point mass m and an oblate body located at the origin of a spherical coordinate system aligned with its polar axis.

$$V = -\frac{GMm}{r} + \frac{GM\left(I_3 - I_1\right)}{2r^3} \left(3\cos\vartheta - 1\right) \tag{1.40}$$

A new oblateness parameter a is introduced:

$$a = \frac{I_3 - I_1}{m} \tag{1.41}$$

Equation (1.40) can be divided by M to express the gravitational potential per unit mass, then the parameter G and m are substituted according to (1.25) to normalize it. The result is the equation in spherical coordinates for the gravitational potential per unit mass for a particle in the vicinity of an oblate body.

$$V = -\frac{1}{r} + \frac{a}{2r^3} \left(3\cos\vartheta - 1\right) \tag{1.42}$$

1.3.2.2 Particle dynamics

As the oblateness of the main body affects only the potential of a particle in its gravitational field, the formula for its kinetic energy is carried over from Section 1.3.1, Equation (1.27). It is combined with the potential per unit mass derived above in (1.42) into the Lagrangian function

$$L = T - V = \frac{1}{2}\left(\dot{r}^2 + r^2\dot{\vartheta}^2 + r^2\sin^2\vartheta\dot{\varphi}^2\right) + \frac{1}{r} - \frac{a}{2r^3}\left(3\cos^2\vartheta - 1\right) \tag{1.43}$$

The perturbation terms arising from the oblateness of the main body are emphasized in green.

Similarly as in (1.3.1.3), the equations of motion of the particle are obtained by solving the Lagrange equation (1.14):

$$\ddot{r} = r\dot{\vartheta}^2 - \frac{1}{r^2} + r\sin^2\vartheta\dot{\varphi}^2 + \frac{3}{2}\frac{a}{r^4}\left(3\cos^2\vartheta - 1\right) \tag{1.44a}$$

$$\ddot{\vartheta} = -2\frac{\dot{r}}{r}\dot{\vartheta} + \cos\vartheta\sin\vartheta\dot{\varphi}^2 + \frac{3a}{r^5}\sin\vartheta\cos\vartheta \tag{1.44b}$$

$$\ddot{\varphi} = -2\left(\frac{\dot{r}}{r} + \dot{\vartheta}\frac{\cos\vartheta}{\sin\vartheta}\right)\dot{\varphi} \tag{1.44c}$$

As the oblate body is still symmetric around its polar axis and the spherical coordinate system is aligned with this axis, the dynamics in the φ coordinate remain unperturbed. Likewise, none of the additional perturbing terms contains φ or its derivative.

The same relations can be expressed in terms of the state vector defined by (1.2):

$$\dot{\boldsymbol{x}} = \begin{bmatrix} \dot{x}_1 \\ \dot{x}_2 \\ \dot{x}_3 \\ \dot{x}_4 \\ \dot{x}_5 \\ \dot{x}_6 \end{bmatrix} = \begin{bmatrix} x_2 \\ x_1x_4^2 - \frac{1}{x_1^2} + x_1\sin^2 x_3x_6^2 + \frac{3}{2}\frac{a}{x_1^4}\left(3\cos^2 x_3 - 1\right) \\ x_4 \\ -2\frac{x_2}{x_1}x_4 + \cos x_3\sin x_3x_6^2 + \frac{3a}{x_1^5}\sin x_3\cos x_3 \\ x_6 \\ -2\left(\frac{x_2}{x_1} + x_4\frac{\cos x_3}{\sin x_3}\right)x_6 \end{bmatrix} \tag{1.45}$$

1.3.3 Circular restricted three-body problem

In Section 1.3.1, the equations of motion of a particle in the gravitational field of a point mass were derived. The influence of the body's oblateness was then added to the dynamics in Section 1.3.2. As orbital mechanics do not deal in general with orbits around isolated celestial objects but with bodies within the Solar system, the gravitational pull of these bodies also represents a force perturbing the particle's orbit. For trajectories close to the main mass, this effect is often approximated as a constant perturbation [8]. If we want to investigate orbits with a radius of a similar order of magnitude as the distance between the bodies, these perturbations must be described more exactly. This thesis will restrict itself to the effect of only a single additional massive body.

The two bodies are assumed rotating around their common centre of mass with a constant angular velocity Ω. It is helpful to treat such a system in a coordinate frame that rotates along with the bodies, such as the Hill's system introduced in Section 1.1.1.

Similarly, as in the previous sections, the equations of motion in the Hill's system will be derived using the Lagrangian method (Section 1.2). The Lagrangian function (1.8) is composed from the kinetic energy and potential. In the Hill's system, the gravitational potential will have to account for the additional gravitational pull from the second body, while the kinetic energy will have additional centrifugal and Coriolis terms emerging from the frame's rotation.

1.3.3.1 Kinetic energy

The kinetic energy of a particle in the Hill's system is easiest obtained from the expression for the kinetic energy in inertial cylindrical coordinates $[\rho,\varphi,z]$ centred at the centre of mass.

$$T = \frac{1}{2}|\dot{\boldsymbol{v}}|^2 = \frac{1}{2}\left(\dot{x}^2 + \dot{y}^2 + \dot{z}^2\right) = \frac{1}{2}\left(\dot{\rho}^2 + \rho^2\dot{\varphi}^2 + \dot{z}^2\right) \tag{1.46}$$

As the coordinate system is transformed from an inertial to one rotating with angular velocity Ω, this constant is added to the angular velocity term in the following coordinates transformation:

$$\begin{aligned} &\rho \to \rho \qquad &&\varphi \to \varphi + t\Omega \qquad &&z \to z \\ &\dot{\rho} \to \dot{\rho} \qquad &&\dot{\varphi} \to \dot{\varphi} + \Omega \qquad &&\dot{z} \to \dot{z} \end{aligned} \tag{1.47}$$

The kinetic energy from (1.46) can be now expressed in these new rotating cylindrical coordinates:

$$T = \frac{1}{2}\left(\dot{\rho}^2 + \rho^2\left(\dot{\varphi} + \Omega\right)^2 + \dot{z}^2\right) = \frac{1}{2}\left(\dot{\rho}^2 + \rho^2\dot{\varphi}^2 + \dot{z}^2 + 2\rho^2\Omega\dot{\varphi} + \rho^2\Omega^2\right) \tag{1.48}$$

Compared with the expression for the kinetic energy in the inertial frame (1.46), the equation in the rotating frame (1.48) contains two additional artefacts of the frame rotation. $\rho^2\Omega^2$ represents the energy generated by centrifugal forces, $-2\rho^2\Omega\dot{\varphi}$ corresponds to Coriolis forces.

The coordinate system is transformed into Cartesian coordinates in order to shift its origin from the centre of mass to the principal body.

$$T = \frac{1}{2}\left(\dot{x}^2 + \dot{y}^2 + \dot{z}^2 + 2\left(x\dot{y} + y\dot{x}\right)\Omega + \left(x^2 + y^2\right)\Omega^2\right) \tag{1.49}$$

This allows the shift to be performed by adjusting only a single position coordinate:

$$\begin{aligned} &x \to x + \mu \qquad &&y \to y \qquad &&z \to z \\ &\dot{x} \to \dot{x} \qquad &&\dot{y} \to \dot{y} \qquad &&\dot{z} \to \dot{z} \end{aligned} \tag{1.50}$$

Leading to the expression for the kinetic energy in Cartesian coordinates rotating centred at the principal body:

$$\begin{aligned} T =& \frac{1}{2}\left(\dot{x}^2 + \dot{y}^2 + \dot{z}^2 + 2\left(\left(x + \mu\right)\dot{y} + y\dot{x}\right)\Omega + \left(\left(x + \mu\right)^2 + y^2\right)\Omega^2\right) \\ =& \frac{1}{2}\left(\dot{x}^2 + \dot{y}^2 + \dot{z}^2 + 2\left(x\dot{y} + y\dot{x}\right)\Omega + \left(x^2 + y^2\right)\Omega^2 + 2\mu\Omega\dot{y} + 2\mu\Omega^2 x + \mu^2\Omega^2\right) \end{aligned} \tag{1.51}$$

Three new terms were added to the formula by shifting the origin, all emerging from the centrifugal and Coriolis terms (the kinetic energy in an inertial frame does not depend on the position (1.46)).

As a final step, the coordinate system is transformed once again, expressing the kinetic energy of a particle in a spherical coordinate system centred at the principal body and co-rotating with the two massive bodies.

$$\begin{aligned} T =& \frac{1}{2}\Big(\dot{r}^2 + r^2\dot{\varphi}^2\sin^2\vartheta r^2\dot{\vartheta}^2 && \text{(1.52a)}\\ &+ 2r^2\Omega\dot{\varphi}\sin^2\vartheta - 2\mu\Omega\left(\dot{r}\sin\vartheta\sin\varphi + r\dot{\vartheta}\cos\vartheta\sin\varphi + r\dot{\varphi}\sin\vartheta\cos\varphi\right)\\ &+ r^2\Omega^2\sin^2\vartheta + 2\mu\Omega^2 r\sin\vartheta\cos\varphi + \mu^2\Omega^2\Big)\\ =& \frac{1}{2}\Big(\dot{r}^2 + r^2\dot{\vartheta}^2 + r^2\sin^2\vartheta\left(\dot{\varphi}+\Omega\right)^2 - 2\mu\Omega\sin\varphi\left(\dot{r}\sin\vartheta + r\dot{\vartheta}\cos\vartheta\right) && \text{(1.52b)}\\ &-2\mu\Omega r\sin\vartheta\cos\varphi\left(\dot{\varphi}+\Omega\right) + \mu^2\Omega^2\Big) \end{aligned}$$

The first line of Equation (1.52a) describe the kinetic energy of a particle moving in an inertial frame. The second line is comprised of terms representing Coriolis forces and the third assembles the contribution of centrifugal forces. Terms containing the reduced mass μ emerged from the shift of the origin of the coordinate system from the centre of mass to the principal body. In subsequent sections, the simplified equation (1.52b) will be used.

1.3.3.2 Gravitational potential

The potential in the restricted three body system is obtained by combining the potential energies (1.22) of both mass points m_1 and m_2, normalized in terms of reduced mass to $1-\mu$ and μ according to (1.4).

$$V(\mathbf{r}) = -\frac{1-\mu}{|\boldsymbol{r}_1|} - \frac{\mu}{|\boldsymbol{r}_2|} \tag{1.53}$$

where $|\boldsymbol{r}_1|$ and $|\boldsymbol{r}_2|$ are the distances from the particle to m_1 and m_2 respectively. The location of both bodies in the Hills system is given by or (1.6).

In Cartesian coordinates centred at the centre of mass and co-rotating with the two bodies located at (1.5), the distances from them is calculated as

$$|\boldsymbol{r}_1| = \sqrt{(x+\mu)^2 + y^2 + z^2} \qquad |\boldsymbol{r}_2| = \sqrt{(x-1+\mu)^2 + y^2 + z^2} \tag{1.54}$$

Inserting (1.54) into (1.53) gives the value of the potential in the Hill's system in Cartesian coordinates.

$$V = -\frac{1-\mu}{\sqrt{x^2+y^2+z^2}} - \frac{\mu}{\sqrt{(x-1)^2+y^2+z^2}} \tag{1.55}$$

If the coordinates are chosen as spherical centred at one of the bodies, the distances to them become

$$|\boldsymbol{r}_1| = r \qquad |\boldsymbol{r}_2| = \sqrt{1 + r^2 - 2r\sin\vartheta\cos\varphi} \tag{1.56}$$

And the corresponding potential

$$V = -\frac{1-\mu}{r} - \frac{\mu}{\sqrt{1 + r^2 - 2r\sin\vartheta\cos\varphi}} \tag{1.57}$$

If the oblateness of the principal body m_1 is taken into account, an additional term from (1.42) is added to (1.57), multiplied by the appropriate weight rescaling.

$$V = -\frac{1-\mu}{r} - \frac{\mu}{\sqrt{1 + r^2 - 2r\sin\vartheta\cos\varphi}} + \frac{a\,(1-\mu)}{2r^3}\,(3\cos\vartheta - 1) \tag{1.58}$$

This holds however only in the case when the polar axis of the oblate body is perpendicular to the principal plane of the Hill's system.

1.3.3.3 Particle dynamics

In the literature ([9, 2]) equations of motion in the Hill's system are usually given in rotating Cartesian coordinates with the centre of mass as origin. They are obtained solving the Lagrange equations (1.14) with the potential (1.55) and kinetic energy (1.49).

$$L = T - V = \frac{1}{2}\left(\dot{x}^2 + \dot{y}^2 + \dot{z}^2 + 2\,(x\dot{y} + y\dot{x})\,\Omega + \left(x^2 + y^2\right)\Omega^2\right) - V \tag{1.59}$$

$$\ddot{x} - 2\dot{y}\Omega = -\frac{\partial V}{\partial x} \tag{1.60a}$$

$$\ddot{y} + 2\dot{x}\Omega = -\frac{\partial V}{\partial y} \tag{1.60b}$$

$$\ddot{z} = -\frac{\partial V}{\partial z} \tag{1.60c}$$

In this thesis however, we will mostly be working with spherical coordinates centred at the principal body. These correspond better to the orbital motions and allow an easier expression of the oblateness of the main body. We combine expressions in spherical coordinates for the kinetic (1.52) and potential (1.57) per unit mass in the Hill's system into the Lagrangian function.

$$\begin{aligned} L =& T - V = \frac{1}{2}\Big(\dot{r}^2 + r^2\dot{\vartheta}^2 + r^2\sin^2\vartheta\,(\dot{\varphi} + \Omega)^2 \\ & -2\mu\Omega\sin\varphi\left(\dot{r}\sin\vartheta + r\dot{\vartheta}\cos\vartheta\right) - 2\mu\Omega r\sin\vartheta\cos\varphi\,(\dot{\varphi} + \Omega) + \mu^2\Omega^2\Big) \\ & + \frac{1-\mu}{r} + \frac{\mu}{\sqrt{1 + r^2 - 2r\sin\vartheta\cos\varphi}} - (1-\mu)\,\frac{a}{2r^3}\left(3\cos^2\vartheta - 1\right) \end{aligned} \tag{1.61}$$

By solving the Lagrange equation (1.14), the dynamics of a particle in the Hill's

system can be derived using the Lagrangian (1.61):

$$\begin{aligned}
\ddot{r} =& r\dot{\vartheta}^2 - \frac{1-\mu}{r^2} - \frac{\mu r}{\sqrt{1+r^2-2r\sin\vartheta\cos\varphi}^3} + r\sin^2\vartheta\left(\dot{\varphi}+\Omega\right)^2 \qquad (1.62a)\\
&+ \mu\sin\vartheta\cos\varphi\left(\frac{1}{\sqrt{1+r^2-2r\sin\vartheta\cos\varphi}^3} - \Omega^2\right)\\
&+ (1-\mu)\frac{3}{2}\frac{a}{r^4}\left(3\cos^2\vartheta - 1\right)\\
\ddot{\vartheta} =& -2\frac{\dot{r}}{r}\dot{\vartheta} + \cos\vartheta\sin\vartheta\left(\dot{\varphi}+\Omega\right)^2 + (1-\mu)\frac{3a}{r^5}\sin\vartheta\cos\vartheta \qquad (1.62b)\\
&+ \frac{\mu}{r}\cos\vartheta\cos\varphi\left(\frac{1}{\sqrt{1+r^2-2r\sin\vartheta\cos\varphi}^3} - \Omega^2\right)\\
\ddot{\varphi} =& -2\left(\frac{\dot{r}}{r} + \dot{\vartheta}\frac{\cos\vartheta}{\sin\vartheta}\right)\left(\dot{\varphi}+\Omega\right) \qquad (1.62c)\\
&- \frac{\mu}{r}\frac{\sin\varphi}{\sin\vartheta}\left(\frac{1}{\sqrt{1+r^2-2r\sin\vartheta\cos\varphi}^3} - \Omega^2\right)
\end{aligned}$$

These equations can also be expressed in terms of the first order state space dynamics, using the state vector (1.2):

$$\begin{aligned}
\dot{x}_1 =& x_2\\
\dot{x}_2 =& x_1x_4^2 - \frac{1-\mu}{x_1^2} - \frac{\mu x_1}{\sqrt{1+x_1^2-2x_1\sin x_3\cos x_5}^3} + x_1\sin^2 x_3\left(x_6+\Omega\right)^2\\
&+ \mu\sin x_3\cos x_5\left(\frac{1}{\sqrt{1+x_1^2-2x_1\sin x_3\cos x_5}^3} - \Omega^2\right)\\
&+ (1-\mu)\frac{3}{2}\frac{a}{x_1^4}\left(3\cos^2 x_3 - 1\right)\\
\dot{x}_3 =& x_4\\
\dot{x}_4 =& -2\frac{x_2}{x_1}x_4 + \cos x_3\sin x_3\left(x_6+\Omega\right)^2 + (1-\mu)\frac{3a}{x_1^5}\sin x_3\cos x_3 \qquad (1.63)\\
&+ \frac{\mu}{x_1}\cos x_3\cos x_5\left(\frac{1}{\sqrt{1+x_1^2-2x_1\sin x_3\cos x_5}^3} - \Omega^2\right)\\
\dot{x}_5 =& x_6\\
\dot{x}_6 =& -2\left(\frac{x_2}{x_1} + x_4\frac{\cos x_3}{\sin x_3}\right)\left(x_6+\Omega\right)\\
&- \frac{\mu}{x_1}\frac{\sin x_5}{\sin x_3}\left(\frac{1}{\sqrt{1+x_1^2-2x_1\sin x_3\cos x_5}^3} - \Omega^2\right)
\end{aligned}$$

1.3.3.4 Jacobi integral

Let us revisit the Lagrangian function in Cartesian coordinates (1.59):

$$L = \frac{1}{2}\left(\dot{x}^2+\dot{y}^2+\dot{z}^2\right) + \left(x\dot{y}+y\dot{x}\right)\Omega + \frac{1}{2}\left(x^2+y^2\right)\Omega^2 + \frac{\mu}{r_1} + \frac{1-\mu}{r_2} \qquad (1.64)$$

The canonical coordinates $\boldsymbol{p}$ corresponding to the Cartesian generalized coordinates $\boldsymbol{q}$ can be derived from the above Lagrangian.

$$\boldsymbol{p} = \frac{\partial L}{\partial \dot{\boldsymbol{q}}} = \begin{bmatrix} \dot{x} + y\Omega \\ \dot{y} + x\Omega \\ \dot{z} \end{bmatrix} \tag{1.65}$$

The Hamiltonian function can now be introduced:

$$\begin{aligned} H =& \sum_k p_k \dot{q}_k - L\left(\boldsymbol{q}, \dot{\boldsymbol{q}}\right) \\ =& \frac{1}{2}\left(\dot{x}^2 + \dot{y}^2 + \dot{z}^2\right) - \frac{1}{2}\left(x^2 + y^2\right)\Omega^2 - \frac{\mu}{r_1} - \frac{1-\mu}{r_2} = T_{ef} + V_{ef} \end{aligned} \tag{1.66}$$

where

$$T_{ef} = \frac{1}{2}\left(\dot{x}^2 + \dot{y}^2 + \dot{z}^2\right) \tag{1.67a}$$

$$V_{ef} = -\frac{1}{2}\left(x^2 + y^2\right)\Omega^2 - \frac{\mu}{r_1} - \frac{1-\mu}{r_2} \tag{1.67b}$$

are the effective kinetic energy and effective potential respectively. The effective potential can be further divided into the centrifugal potential (first term) and the gravitational potential of both bodies (last two terms).

The Jacobi integral is a function commonly defined as twice the value of the Hamiltonian:

$$J = 2H = \dot{x}^2 + \dot{y}^2 + \dot{z}^2 - \left(x^2 + y^2\right)\Omega^2 - 2\frac{\mu}{r_1} - 2\frac{1-\mu}{r_2} \tag{1.68}$$

The Jacobi integral describes the total energy of the system and, as no dissipative force is applied, is constant. It allows the characterization of the energy level of an orbit.

1.3.3.5 Lagrange points

In the last section, we introduced the Jacobi integral, a value that denotes the energy of an orbit in the Hill's system. The Jacobi integral remains constant for the entire duration of an uncontrolled orbit. Figure 1.5 plots the effective potential (1.67b) in the principal plane of the Hill's system. It also represents the values of the Jacobi integral if $T_{ef} = 0$. As the effective potential contains three terms, we can see that the graph on Figure 1.5 is obtained by combining three shapes, one rotational paraboloid centred at the centre of mass and two hyperboloids centred at the two mass points. If a particle with zero velocity is inserted in the Hill's system, its orbit will be confined to the area inside the zero-velocity curve on which it lies.

The shape of the effective potential displayed on Figure 1.5, shows to have 5 local minima. These correspond to 5 equilibrium points, position where $\nabla E_{ef} = \mathbf{0}$. The equilibrium points in the Hill's system are called Lagrange points and are important locations for orbit placement. A particle placed in these equilibria will remain motionless in the rotating frame, while performing a circular motion around the centre of mass with the same velocity as the two bodies in the inertial

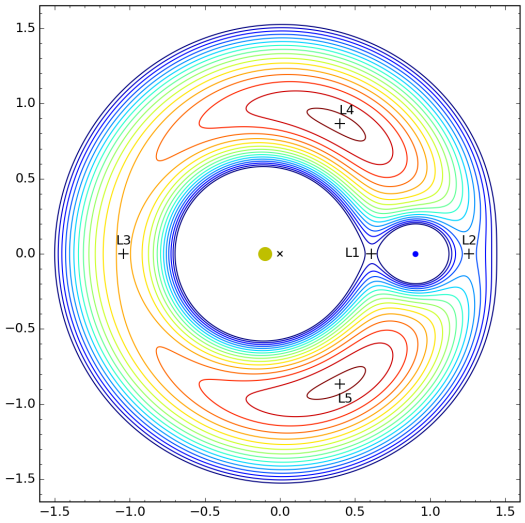

Figure 1.5: Zero-velocity curves representing the effective potential of in the principal plane of the Hill's system for $\mu = 0.1$. The yellow dot represents the principal body, the blue dot the second body, $\times$ the barycentre. Figure taken from `http://leancrew.com/all-this/2016/08/lagrange-points-redux/`.

	x_{01}	x_{02}	x_{03}	x_{04}	x_{05}	x_{06}	J
L1	0.6697405	0	$\pi/2$	0	0	0	-3.7168
L2	1.4203341	0	$\pi/2$	0	0	0	-3.5244
L3	0.9123	0	$\pi/2$	0	π	0	-3.1488
L4	1	0	$\pi/2$	0	$\pi/3$	0	-2.8725
L5	1	0	$\pi/2$	0	$-\pi/3$	0	-2.8725

Table 1.1: Table of Lagrange points locations for $\mu = 0.15$

frame, as will be seen on Figure 1.29, in Section 1.4.5.1. The formal proof of existence and the stability of Lagrange points is discussed in [9].

Points L4 and L5 are stable and located on the vertices of equilateral triangles formed by these Lagrange points and the two bodies. Their specification in spherical coordinates and corresponding value of the Jacobi integral is given in Table 1.1. Their stability signifies natural celestial bodies might be trapped on them or in the region around them. These are called Trojan and are a common sight in the solar system. The most famous and numerous group of Trojan asteroids is located at Sun-Jupiter Lagrange point L4 (the Greek camp) and L5 (the Trojan camp). To date, Earth has a single observed natural Trojan called 2010-TK7 and orbiting in a tadpole orbit around L4.

Contrary to L4 and L5, the first three are located on saddle-nodes of the potential curve and thus are unstable. They are collinear with both bodies but their exact position depends on μ and cannot be numerically calculated. Their unstable manifolds coincide with the principal axis between the two bodies. To locate them, we simulated the system numerous times along this axis with zero velocity. We observed the value of the initial radial acceleration and recorded it on Figure 1.6. Where the acceleration is zero, centrifugal and gravitational forces cancel out and the system is in equilibrium. Exact locations of Lagrange points L1-3 for $\mu = 0.15$ are given by Table 1.1. Because of their instability, natural

satellites are not found on or around these equilibria and artificial ones need to be kept there with control.

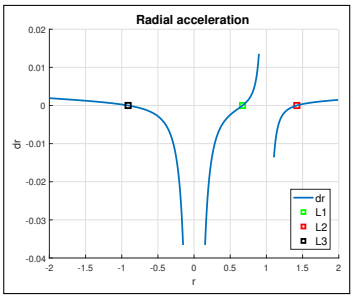

Figure 1.6: Radial acceleration along the principal axis with Lagrange points L1-3 for $\mu = 0.15$. Values close to the bodies are not included as they go to infinity.

L1 is a saddle equilibrium located on the segment between the two bodies, close to the smaller one. Artificial satellites are not placed precisely at this equilibrium point in the Sun-Earth system, because solar radiation would foil any communication with the satellite from Earth. It is however possible to place a satellite in orbits around L1 that maintain their shape in the rotating frame, at least until they are overcome by their instability. These orbits are called halo orbits and a more profound analysis will be given in Section 1.4.5.2. An example of a man-made satellite in halo orbit around L1 is the SOHO satellite, responsible for solar observation and detection of space weather before it reaches the Earth.

Similarly to L1, the L2 Lagrangian point is a saddle equilibrium with unstable manifolds on the axis of the masses. It is located a little beyond the smaller body. In the case of the Sun-Earth system, it is used for space observation, as it is partially shielded from solar radiation by the planet. This means however that L2 is also partially shaded. For this reason, halo orbits at L2 are useful as they allow to escape the Earth's shadow for better solar panel efficiency. The developed James Webb Space Telescope is planned to orbit on a halo orbit around L2.

The last Lagrange point L3 is located opposite of the smaller body at a distance from the barycentre similar to the distance from the centre of mass to the small mass. Though no natural satellite can remain at this unstable equilibrium, the possibility of a Counter-Earth, a twin planet located on the other opposite side of the Sun, has long captured the imagination of classical philosophers and science-fiction writers alike. In the Sun-Earth system, artificial satellite at L3 would be unable to communicate with the Earth because of the strong interferences from the Sun in between.

1.3.4 Elliptic restricted three-body problem

In Section 1.3.3, we derived the equations of motion of a massless test body in the gravitational field of two bodies. The two masses are orbiting around a motionless centre of mass on circular orbits. Their relative motion as it follows from Equation (1.21) does not require the bodies to revolve on circular trajectories and maintain a constant distance. In fact, two masses subjected to only their mutual gravitational attraction will follow a Keplerian orbit in the shape of a conic section: a circle, an ellipse, a parabola or a hyperbola. The different types

of Keplerian orbits will be discussed and compared in Section 1.4.1. Particles on parabolic or hyperbolic orbits have a kinetic energy large enough to overcome the gravitational potential and a move apart from each other indefinitely. On the other hand, particles on elliptic and circular orbits remain bound to each other in a periodic motion. Circular orbits can be considered a special case of elliptic orbits with eccentricity $e = 0$.

Most applications for the Hill's system involve either the Earth-Moon or Sun-Earth systems. In those cases the eccentricity of the bodies orbit is low, and dynamics derived in the circular Hill's system are usually a sufficient approximation. When dealing with bodies orbiting on more pronouncedly elliptic orbits a more general formulation of the equations of motion is required. For example the dynamics or potential exoplanets in solar systems with pulsating binary stars are governed by the equations of motion derived in this section. Even when the system has a low eccentricity, it might be worthwhile not to neglect it if a highly precise solution is required. Finally, the elliptic Hill's system can be applied to express the dynamics of a formation of satellites in a LHLV reference frame centred at a leader on an elliptic orbit, as described in 1.1.2.

In this section, we will generalise the equations of motion derived in Section 1.3.3 to express the dynamics of a massless particle in the vicinity of two massive bodies mutually describing elliptic orbits around their centre of mass. In the circular case, we expressed the equations of motion in a frame co-rotating with the two bodies around their centre of mass. This allowed for both bodies to remain fixed with regard to this reference frame. In addition, all distances are rescaled in order to normalize the distance between the bodies to 1. If the same is to be accomplished for an elliptical Hill's system, the frame's rotation and rescaling have to be time-variant, as both the mutual distance and angular velocity of the bodies are not constant.

For two bodies on elliptic trajectories around each other, their mutual distance is expressed as

$$r = \frac{a\left(1 - e^2\right)}{1 + e\cos h} \tag{1.69}$$

where a is the ellipse's semi-major axis and h is the true anomaly, the angle from the periapsis indicating the position on the orbit. The periapsis is the point where the two bodies are the closest to each other.

The conserved angular momentum is expressed as

$$r^2\Omega = \sqrt{a\left(1 - e^2\right)} \tag{1.70}$$

In the case of the standard circular Hill's system, both r and Ω are constants. Here are r is given by (1.69) and Ω indicates the time derivative of the true anomaly:

$$\Omega = \frac{\mathrm{d}h}{\mathrm{d}t} \tag{1.71}$$

1.3.4.1 Kinetic energy

We start with the expression (1.49) for the kinetic energy of a particle in a coordinate frame rotating with angular velocity $\Omega\left(t\right)$, corresponding to the time-

dependent angular velocity of revolution of the two primary bodies.

$$T = \frac{1}{2}\left(\dot{x}^2 + \dot{y}^2 + \dot{z}^2 + 2\left(x\dot{y} + y\dot{x}\right)\Omega + \left(x^2 + y^2\right)\Omega^2\right) \tag{1.72}$$

In this rotating frame, the bodies lie on one axis, but their position still fluctuate. In order to rescale the distances and fix the bodies, pulsating Cartesian coordinates are introduced

$$\xi = \frac{x}{r} \qquad \eta = \frac{y}{r} \qquad \zeta = \frac{z}{r} \tag{1.73}$$

By introducing them into the expression (1.72) , the kinetic energy in pulsating rotating coordinates is obtained:

$$\begin{aligned} T =& \frac{1}{2}\left[\left(\dot{r}\xi + r\dot{\xi}\right)^2 + \left(\dot{r}\eta + r\dot{\eta}\right)^2 + \left(\dot{r}\zeta + r\dot{\zeta}\right)^2\right. \\ &\left. + 2\Omega\left(r\xi\left(\dot{r}\eta + r\dot{\eta}\right) - r\eta\left(\dot{r}\xi + r\dot{\xi}\right)\right) + r^2\left(\xi^2 + \eta^2\right)\Omega^2\right] \\ =& \frac{1}{2}\left[r^2\left(\dot{\xi}^2 + \dot{\eta}^2 + \dot{\zeta}^2\right) + \dot{r}^2\left(\xi^2 + \eta^2 + \zeta^2\right)\right. \\ &\left. + 2r\dot{r}\left(\xi\dot{\xi} + \eta\dot{\eta} + \zeta\dot{\zeta}\right) + 2\Omega r^2\left(\xi\dot{\eta} - \eta\dot{\xi}\right) + r^2\Omega^2\left(\xi^2 + \eta^2\right)\right] \end{aligned} \tag{1.74}$$

The expression above contains time derivatives. We can transform the system to be a function of true anomaly instead of time with

$$\frac{\mathrm{d}}{\mathrm{d}t} = \frac{\mathrm{d}h}{\mathrm{d}t}\frac{\mathrm{d}}{\mathrm{d}h} = \Omega\frac{\mathrm{d}}{\mathrm{d}h} \tag{1.75a}$$

$$\mathrm{d}t = \frac{\mathrm{d}t}{\mathrm{d}h}\mathrm{d}h = \frac{1}{\Omega}\mathrm{d}h \tag{1.75b}$$

The action S becomes anomaly-dependent from time-dependent by the following transformation:

$$S = \int L\left(q,\dot{q},t\right)\mathrm{d}t \rightarrow S = \int \widetilde{L}\left(q,q',h\right)\mathrm{d}h \tag{1.76}$$

where $q' = \frac{\mathrm{d}q}{\mathrm{d}h}$ is the derivative of coordinate q with regards to the true anomaly and $\widetilde{L}$ is the anomaly dependent Lagrangian, which can be expressed using (1.75) as

$$\widetilde{L}\left(q,q',h\right) = \frac{1}{\Omega}L\left(q,\Omega q',t\left(h\right)\right) \tag{1.77}$$

The expression for the kinetic energy in anomaly-variant pulsating coordinate becomes:

$$\begin{aligned} \widetilde{T} =& \frac{1}{2}\left[r^2\Omega\left(\xi'^2 + \eta'^2 + \zeta'^2\right) + r'^2\Omega\left(\xi^2 + \eta^2 + \zeta^2\right)\right. \\ &\left. + 2rr'\Omega\left(\xi\xi' + \eta\eta' + \zeta\zeta'\right) + 2r^2\Omega\left(\xi\eta' - \eta\xi'\right) + r^2\Omega\left(\xi^2 + \eta^2\right)\right] \end{aligned} \tag{1.78}$$

With the angular momentum of the primary bodies $r^2\Omega$ multiplying the first, fourth and fifth element of (1.78) being constant, we need to further investigate

terms $r'^2\Omega$ and $2rr'\Omega$ multiplying the second and third term of the expression for the kinetic energy respectively.

$$r = \frac{a\left(1-e^2\right)}{1+e\cos h} \qquad r' = \frac{a\left(1-e^2\right)}{\left(1+e\cos h\right)^2} e\sin h \quad \rightarrow \quad \frac{r'}{r} = \frac{e\sin h}{1+e\cos h} \tag{1.79}$$

$$r'^2\Omega = r^2\Omega\left(\frac{r'}{r}\right)^2 = \sqrt{a\left(1-e^2\right)}\frac{e^2\sin^2 h}{\left(1+e\cos h\right)^2} \tag{1.80a}$$

$$2rr'\Omega = 2r^2\Omega\frac{r'}{r} = 2\sqrt{a\left(1-e^2\right)}\frac{e\sin h}{1+e\cos h} \tag{1.80b}$$

The above expressions are substituted into (1.78).

$$\begin{aligned}\widetilde{T} =& \frac{1}{2}\left[r^2\Omega\left(\xi'^2+\eta'^2+\zeta'^2\right) + 2r^2\Omega\left(\xi\eta'-\eta\xi'\right) + r^2\Omega\left(\xi^2+\eta^2\right)\right.\\ &+ 2\sqrt{a\left(1-e^2\right)}\frac{e\sin h}{1+e\cos h}\left(\xi\xi'+\eta\eta'+\zeta\zeta'\right)\\ &\left.+\sqrt{a\left(1-e^2\right)}\frac{e^2\sin^2 h}{\left(1+e\cos h\right)^2}\left(\xi^2+\eta^2+\zeta^2\right)\right]\\ =& \frac{1}{2}\sqrt{a\left(1-e^2\right)}\left[\left(\xi'^2+\eta'^2+\zeta'^2\right) + 2\left(\xi\eta'-\eta\xi'\right) + \left(\xi^2+\eta^2\right)\right.\\ &\left.+2\frac{e\sin h}{1+e\cos h}\left(\xi\xi'+\eta\eta'+\zeta\zeta'\right) + \frac{e^2\sin^2 h}{\left(1+e\cos h\right)^2}\left(\xi^2+\eta^2+\zeta^2\right)\right]\end{aligned} \tag{1.81}$$

We remark that, in the previous equation, the next-to-last term is close from being the derivative of the last, as

$$\frac{\mathrm{d}}{\mathrm{d}h}\left(\xi^2+\eta^2+\zeta^2\right) = 2\left(\xi\xi'+\eta\eta'+\zeta\zeta'\right) \tag{1.82}$$

Knowing that the Lagrangian is determined up to a total derivative, a simplified equivalent Lagrangian can be found by subtracting a derivative term from its kinetic energy.

$$\begin{aligned}&\frac{\mathrm{d}}{\mathrm{d}h}\left[\frac{e\sin h}{1+e\cos h}\left(\xi^2+\eta^2+\zeta^2\right)\right]\\ &= \frac{\mathrm{d}}{\mathrm{d}h}\left(\frac{e\sin h}{1+e\cos h}\right)\left(\xi^2+\eta^2+\zeta^2\right) + \frac{e\sin h}{1+e\cos h}\frac{\mathrm{d}}{\mathrm{d}h}\left(\xi^2+\eta^2+\zeta^2\right)\\ &= \frac{e^2\sin^2 h}{\left(1+e\cos h\right)^2}\left(\xi^2+\eta^2+\zeta^2\right) + \frac{e\sin h}{1+e\cos h}\left(\xi^2+\eta^2+\zeta^2\right)\\ &+ 2\frac{e\sin h}{1+e\cos h}\left(\xi\xi'+\eta\eta'+\zeta\zeta'\right)\end{aligned} \tag{1.83}$$

This allows us to substitute the last two terms of (1.81) with one derivative and one additional term.

$$\begin{aligned}&\frac{e^2\sin^2 h}{\left(1+e\cos h\right)^2}\left(\xi^2+\eta^2+\zeta^2\right) + 2\frac{e\sin h}{1+e\cos h}\left(\xi\xi'+\eta\eta'+\zeta\zeta'\right)\\ &= \frac{\mathrm{d}}{\mathrm{d}h}\left[\frac{e\sin h}{1+e\cos h}\left(\xi^2+\eta^2+\zeta^2\right)\right] - \frac{e\sin h}{1+e\cos h}\left(\xi^2+\eta^2+\zeta^2\right)\end{aligned} \tag{1.84}$$

The derivative term can be omitted to write a simplified expression for an equivalent kinetic energy

$$\begin{aligned}\widetilde{T}_{eq} =& \frac{1}{2}\sqrt{a\left(1-e^2\right)}\left[\left(\xi'^2+\eta'^2+\zeta'^2\right)+2\left(\xi\eta'-\eta\xi'\right)+\left(\xi^2+\eta^2\right)\right.\\ &\left.-\frac{e\sin h}{1+e\cos h}\left(\xi^2+\eta^2+\zeta^2\right)\right]\end{aligned} \tag{1.85}$$

1.3.4.2 Potential

In the previous section, an expression for the kinetic energy of a particle in pulsating rotating coordinates has been derived. In order to calculate the Lagrangian, the gravitational potential has to be expressed as well in this coordinate system. The gravitational potential in the rotating Cartesian coordinates of the circular Hill's system is given by (1.53):

$$V\left(\mathbf{r}\right) = -\frac{1-\mu}{R_1} - \frac{\mu}{R_2} \tag{1.86}$$

where R_1 and R_2 is the distance to the two bodies.

We can find the equivalent potential $\widetilde{V}$ in a pulsating coordinate system by rescaling all distances by the distance between the bodies r.

$$\begin{aligned}R_1\left(x,y,z,\mu\right) =& r\widetilde{R}_1\left(\xi,\eta,\zeta,\mu\right)\\ R_2\left(x,y,z,1-\mu\right) =& r\widetilde{R}_1\left(\xi,\eta,\zeta,1-\mu\right)\end{aligned} \tag{1.87}$$

As we switch to true anomaly-dependent pulsating coordinates, the Lagrangian is scaled by the inverse of Ω (Equation (1.77)). This term is carried over to the expression for the potential in pulsating rotating coordinates:

$$\begin{aligned}\frac{1}{\Omega}V =& \frac{1}{r\Omega}\widetilde{V} = \frac{1}{r^2\Omega}r\widetilde{V} = \frac{1}{\sqrt{a\left(1-e^2\right)}}\frac{a\left(1-e^2\right)}{1+e\cos h}\widetilde{V}\\ =& \frac{\sqrt{a\left(1-e^2\right)}}{1+e\cos h}\widetilde{V} = \frac{\sqrt{a\left(1-e^2\right)}}{1+e\cos h}\left(-\frac{1-\mu}{\widetilde{R}_1}-\frac{\mu}{\widetilde{R}_2}\right)\end{aligned} \tag{1.88}$$

where substitutions for r from (1.79) and for the angular momentum $r^2\Omega$ from (1.70) are used.

1.3.4.3 Particle dynamics

The true anomaly-dependent Lagrangian in pulsating rotating coordinates is obtained by combining Equation (1.85) for the kinetic energy and (1.88) for the gravitational potential.

$$\widetilde{L} = \sqrt{a\left(1-e^2\right)}\left(\widetilde{T}_{eq} - \frac{1}{1+e\cos h}\widetilde{V}\right) \tag{1.89}$$

The irrelevant constant angular momentum multiplier can be removed from

the equation above to give an equivalent expression for the Lagrangian

$$\begin{aligned}\widetilde{L}_{eq} =&\widetilde{T}_{eq} - \frac{1}{1+e\cos h}\widetilde{V}\\ =&\frac{1}{2}\left[\left(\xi'^2+\eta'^2+\zeta'^2\right)+2\left(\xi\eta'-\eta\xi'\right)+\left(\xi^2+\eta^2\right)\right.\\ &\left.-\frac{e\sin h}{1+e\cos h}\left(\xi^2+\eta^2+\zeta^2\right)\right]-\frac{1}{1+e\cos h}\widetilde{V}\end{aligned} \tag{1.90}$$

Rearrangements are made in the formula in order to merge the $(\xi^2+\eta^2+\zeta^2)$ and $(\xi^2+\eta^2)$ terms and simplify the expression.

$$\begin{aligned}\widetilde{L}_{eq} =&\frac{1}{2}\left[\left(\xi'^2+\eta'^2+\zeta'^2\right)+2\left(\xi\eta'-\eta\xi'\right)-\zeta^2\right]\\ &-\frac{1}{1+e\cos h}\left[\frac{1}{2}\left(\xi^2+\eta^2+\zeta^2\right)-\widetilde{V}\right]\end{aligned} \tag{1.91}$$

The equations of motion in of a particle in the gravitational field of two bodies orbiting each other on elliptic orbits can be obtained by solving the Lagrange equations

$$\frac{\mathrm{d}}{\mathrm{d}h}\frac{\partial L}{\partial q'}-\frac{\partial L}{\partial q}=0 \tag{1.92}$$

The particle dynamics are given in derivative with respect to the true anomaly of the two bodies orbits, in Cartesian coordinates of a frame co-rotating and pulsating such that the bodies maintain fixed positions.

$$\xi''-2\eta' = \frac{1}{1+e\cos h}\left(\xi-\frac{\partial\widetilde{V}}{\partial\xi}\right) \tag{1.93a}$$

$$\eta''-2\xi' = \frac{1}{1+e\cos h}\left(\eta-\frac{\partial\widetilde{V}}{\partial\eta}\right) \tag{1.93b}$$

$$\zeta'' = \frac{1}{1+e\cos h}\left(-e\cos h\xi-\frac{\partial\widetilde{V}}{\partial\xi}\right) \tag{1.93c}$$

If Ω an r are constant in time, the coordinates $[\xi,\eta,\zeta]$ are no longer pulsating, $e=0$ and the equations of motion above become equivalent to those in the circular Hill's system (1.60c), with $h=\Omega t$ being only a rescaled time.

The analysis of orbits and derivation of control tools in the elliptic Hill's system are out of the scope of this thesis. As Chapter 3 will mainly treat shape-invariant formations, these would no longer maintain their mutual distances if described in a pulsating coordinate system.

1.4 Demonstration of orbits

As the models derived in Section 1.3 are highly non-linear, qualitatively different types of orbits are expected to appear This is why, in this section, we will simulate the dynamics with various parameter configurations and initial conditions to present distinct classes of orbital trajectories. These orbits will serve as

initial or final states of orbit transfers in Chapter 2. As the uncontrolled dynamics of members of satellite formations also follow the equations derived in the previous section, their trajectories are described by the orbits presented in this section.

1.4.1 Keplerian orbits

In the Kepler two-body problem, a massless particle moves in the gravitational field of a point mass in one of four qualitatively different types of orbit corresponding to different conic sections.

As the gravitational field is symmetric with regards to the origin of coordinate system centred at the massive body, all orbital planes are equivalent. We decided in this section, without loss of generality, to execute simulations of Keplerian orbits in the equatorial plane of the principal body.

The equation for the radial motion of such a particle is given by (1.29a):

$$\ddot{r} = r\dot{\varphi}^2 - \frac{1}{r^2} \tag{1.94}$$

We can introduce the angular momentum h, which is constant for each orbit

$$h = r^2\dot{\varphi} \tag{1.95}$$

If substituted into (1.94), the resulting expression for the radial acceleration becomes dependent only on the radius r and the constant h, thus forming a one-dimensional oscillator.

$$\ddot{r} = \frac{h^2}{r^3} - \frac{1}{r^2} = -\frac{\partial V_{ef}}{\partial r} \tag{1.96}$$

The effective potential is obtained by integrating the above expression and is plotted on Figure 1.7.

$$V_{ef}\left(r\right) = \frac{1}{2}\frac{h^2}{r^2} - \frac{1}{r} \tag{1.97}$$

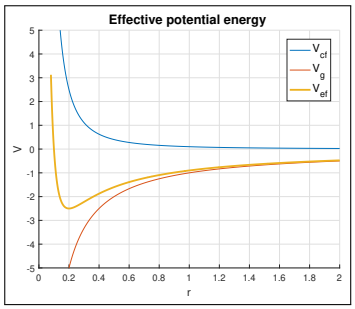

Figure 1.7: Effective potential energy curve for $h = 0.4472$.

Orbits can be distinguished into 4 qualitatively different orbit shapes according to their energy. This section will successively present all four Keplerian orbits with initial conditions according to Table 1.2. The total energy will be represented by $J = 2E = 2T + 2U$, equivalent to the Jacobi integral (1.68). As there are no dissipative forces at play in orbital mechanics if atmospheric drags are neglected, the total energy remains constant.

	x_{01}	x_{02}	x_{03}	x_{04}	x_{05}	x_{06}	J
Circular	0.2	0	$\pi/2$	0	0	10.1803	-5.0
Elliptic	0.2	0	$\pi/2$	0	0	13.4164	-2.8
Parabolic	0.2	0	$\pi/2$	0	0	15.8114	0
Hyperbolic	0.2	0	$\pi/2$	0	0	17.8885	2.8

Table 1.2: Table of initial states for Keplerian orbits

1.4.1.1 Circular orbit

With a chosen orbital plane (the equatorial) and initial radius, the radial velocity is set to zero and the only state left to specify is the angular velocity. We know that in order to maintain a radial acceleration of zero, the centripetal force must equal the gravitational:

$$\frac{mv_t^2}{r} = \frac{GMm}{r^2} \tag{1.98}$$

The tangential velocity is obtained by rearranging the above equation.

$$v_t = \sqrt{\frac{GM}{r}} \tag{1.99}$$

Using normalizing substitutions from (1.25) and the general formula $\dot{\varphi} = \frac{v_t}{r}$, the angular velocity of a circular orbit of radius r is obtained.

$$\dot{\varphi}_c = \frac{1}{\sqrt{r^3}} \tag{1.100}$$

Circular orbits have the lowest energy of all Keplerian orbits of the same angular momentum. This signifies they occupy the minimum of the potential curve on Figure 1.8, meaning only a single radius is available to them. This has been confirmed experimentally by simulating the Keplerian motion of a particle according to (1.30) with initial conditions given by Table 1.2 according to (1.100).

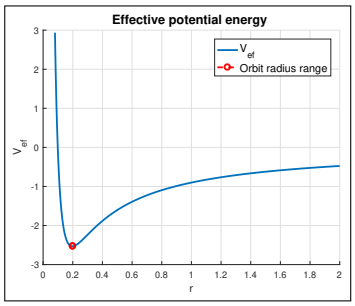

Figure 1.8: Effective potential energy curve for $h = 0.4472$.

Indeed, it can be seen on Figure 1.9 that a Keplerian orbit of circular shape maintains all its states constant (except the angular state, which grows linearly). Its kinetic and potential energy, hence also the total, are therefore also constant.

Optimal transfers between Keplerian circular orbits will be presented in Section 2.3.1. Trailing formations on circular trajectories will be reconfigured using an optimal controller in Section 3.2.1 and a close-loop cooperative one in Section 3.3.2.

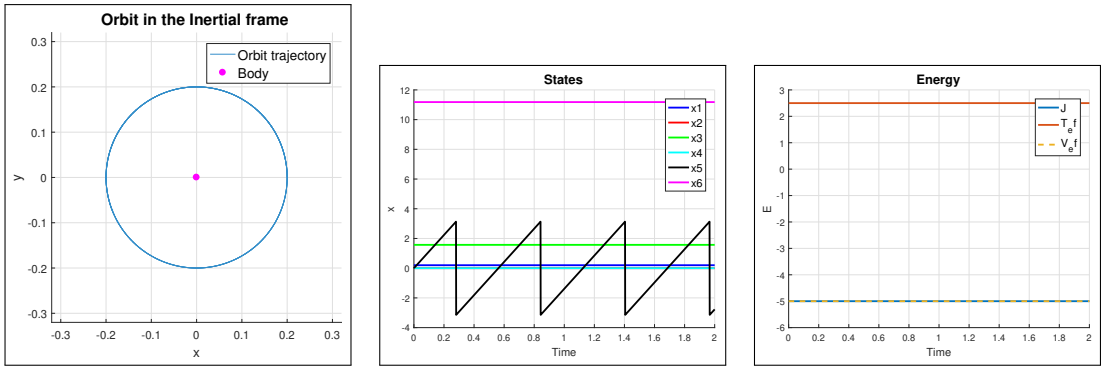

Figure 1.9: Circular orbit around a single body with no perturbation. $r = 0.2$.

1.4.1.2 Elliptic orbit

By maintaining the same initial radius as in the circular case and increasing its angular velocity, an elliptic orbit can be obtained. Its initial condition (listed in Table 1.2) are given by:

$$\dot{\varphi}_{ep} = \frac{1.2}{\sqrt{r_p}^3} = 1.2\dot{\varphi}_c \tag{1.101}$$

With φ_{ep} being the angular velocity at the periapsis of the ellipse. The periapsis is the point of the orbit, where the radius is minimal and angular velocity maximal. The apoapsis is the opposite of the periapsis, the radius is maximal there and the velocity minimal.

An uncontrolled orbit with those initial conditions (Table 1.2) is displayed on Figure 1.11. Both the trajectory, state and energy graph (Figure 1.10) show that the particle oscillates between a high-velocity periapsis position close to the body and a low-velocity apoapsis further from it on the other side. In accordance with Kepler's first law of planetary motion, the body is located at one of the focal points of the ellipse.

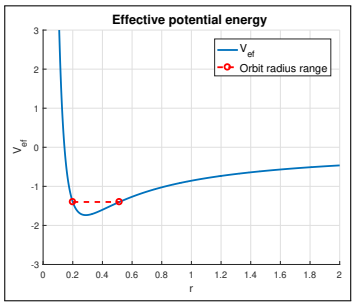

Figure 1.10: Effective potential energy curve for $h = 0.5367$.

1.4.1.3 Parabolic orbit

If the initial angular velocity is increased even further, the orbiting particle will escape the gravitational sphere of influence of the body. The critical case when this happens corresponds to the effective potential (1.97) equalling zero.

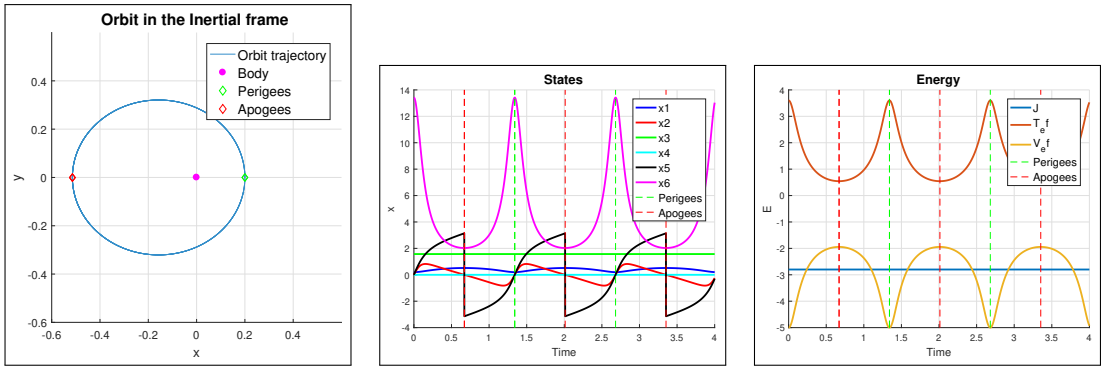

Figure 1.11: Elliptic orbit around a single body with no perturbation. $r_p = 0.2$.

For a chosen radius, the corresponding angular velocity is obtained as:

$$\dot{\varphi}_{pp} = \frac{\sqrt{2}}{\sqrt{r_p}^3} = \sqrt{2}\dot{\varphi}_c \tag{1.102}$$

The particle simulated with such initial conditions moves on a parabolic curve. It reaches a global maximum in kinetic energy (and minimum in radius) at its single periapsis (Figure 1.13). After that, it moves away from the body with ever decreasing velocity. At infinity, the particle is infinitely far away with a zero velocity. The energy graph from Figure 1.13 and Figure 1.12 testify the parabolic orbit is an orbit with zero total energy.

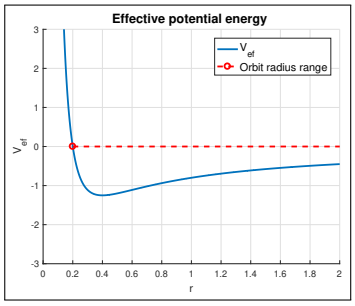

Figure 1.12: Effective potential energy curve for $h = 0.6325$.

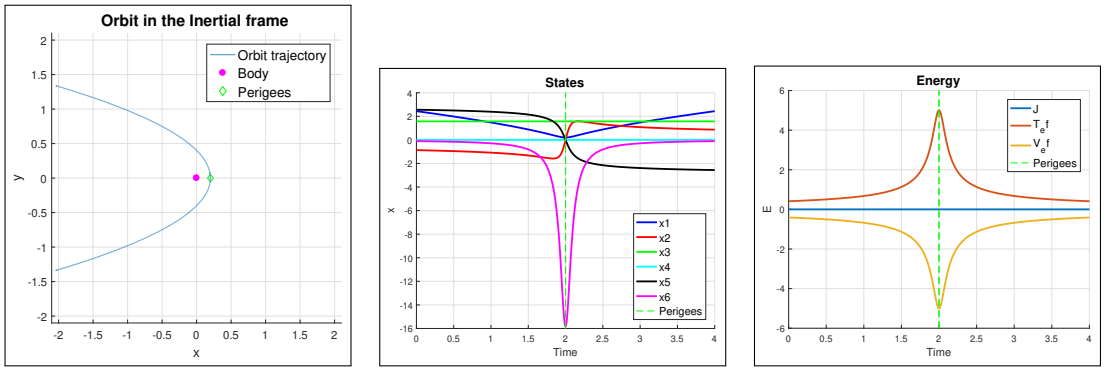

Figure 1.13: Parabolic orbit around a single body with no perturbation. $r_p = 0.2$.

1.4.1.4 Hyperbolic orbit

If a particle is given enough initial energy, it successively escaped the gravitational field of the body, achieving a constant final velocity as the gravitational pull goes to zero. With the parabolic orbit described above being the threshold case with zero total energy, a particle with a positive total energy should be able to escape (Figure 1.14). Such an orbit was simulated with initial conditions given in Table 1.2, where the angular velocity was determined by

$$\dot{\varphi}_{hp} = \frac{1.6}{\sqrt{r_p}^3} = 1.6\dot{\varphi}_c > \dot{\varphi}_{pp} \tag{1.103}$$

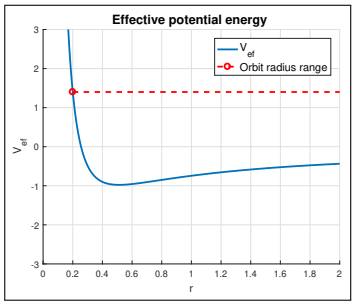

Figure 1.14: Effective potential energy curve for $h = 0.7155$.

Contrary to the parabolic orbit, a particle on this trajectory does not see its velocity decrease to zero as it moves away from the body but settles on a non-zero constant. In fact, it follows a hyperbolic curve (Figure 1.15).

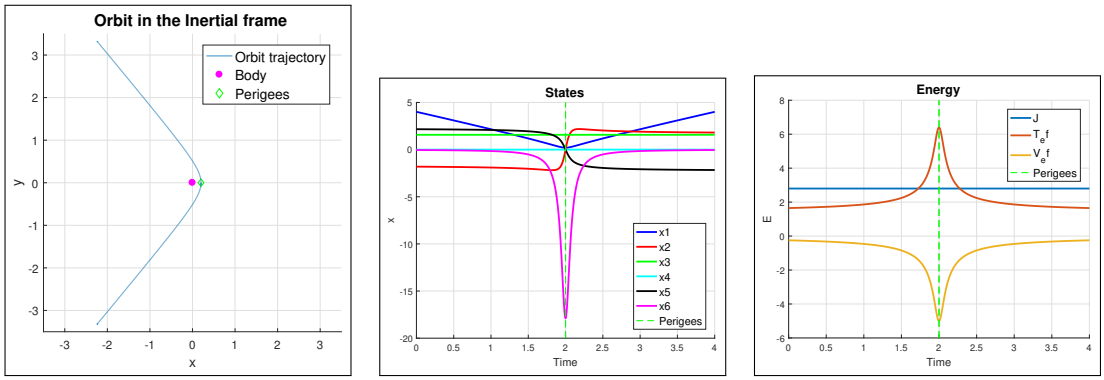

Figure 1.15: Hyperbolic orbit around a single body with no perturbation. $r_p = 0.2$.

1.4.2 Perturbations due to oblateness of the principal body

In Section 1.3.2, the effect of deformations of the massive body on the gravitational field around it was discussed. The oblateness of the body, its flattening at the poles, has been identified as its primary deviation from a perfect sphere. In this section, orbits of a massless particle around an oblate body will be simulated according to the state equations (1.45) and the results are discussed. The origin of the coordinate system is placed to the centre of the body and the xy plane is aligned with its equatorial plane.

As the body is no longer spherical, its gravitational field is not spherically symmetric any-more. This means that, contrary to the Keplerian system from the last section, orbital planes are no longer equivalent. In this section, we will simulate orbits perturbed by the oblateness of the body in its equatorial plane and in a plane inclined with regard to the equatorial. The value for the oblatness parameter is set to $a = 0.0001$. As in the previous section, locations where the kinetic energy is minimal and maximal are useful for inferring the general character or an orbit. However, they can only be called apoapsides and periapsides for Keplerian orbits. We therefore define TP_P a turning point where the kinetic energy reaches a local maximum and TP_A in case of minimum, regardless of the shape of the orbit.

	x_{01}	x_{02}	x_{03}	x_{04}	x_{05}	x_{06}	J
Circular	0.2	0	$\pi/2$	0	0	11.1803	-5.0125
Circular inclined	0.2	0	$3\pi/4$	0	0	15.8114	-4.9895

Table 1.3: Table of initial states for orbits perturbed by the oblateness of the central body

1.4.2.1 Perturbed circular orbit in the equatorial plane

In 1.4.1.1, initial conditions were derived for a circular Keplerian orbit. Using the same initial states (Table 1.3) for a particle in the gravitational field of an oblate body will uncover the perturbing effect of the oblateness on the shape of the orbit. The equations of motion (1.44) inform us that, if the initial position and velocity vectors both lie in the equatorial plane, the only perturbing term from the oblateness of the body is a positive radial acceleration proportional to the oblateness parameter and inversely proportional to the fourth power of the radius:

$$\begin{aligned} \ddot{r} &= r - \frac{1}{r^2} + r\dot{\varphi}^2 + \frac{3a}{r^4} \\ \ddot{\varphi} &= -2\frac{\dot{r}}{r}\dot{\varphi} \end{aligned} \tag{1.104}$$

As $\vartheta = \pi/2$ and $\dot{\vartheta}_0 = 0$, the equation for the angular acceleration in the polar direction can be crossed out. This is confirmed by Figure 1.16, where all states related to ϑ stay constant and the perturbation does not take the orbit away from its initial, equatorial, plane.

Due to the oblateness of the body, the intended circular shape of the orbit is deformed into an ellipse. In addition, the periapsides and apoapsides of the elliptic orbit are precessing with a constant rate in the direction of the revolution. Precession is the rotation of the axis joining the periapsis and apoapsis between each consecutive revolution.

1.4.2.2 Perturbed circular orbit inclined to the equatorial plane

As mentioned earlier, the gravitational field around an oblate body is not a central force field. We therefore expect a qualitatively different trajectory if the initial orbit is set to be inclined with regards to the equatorial plane. The initial angular speed is maintained so that a circular orbit would have been obtained in

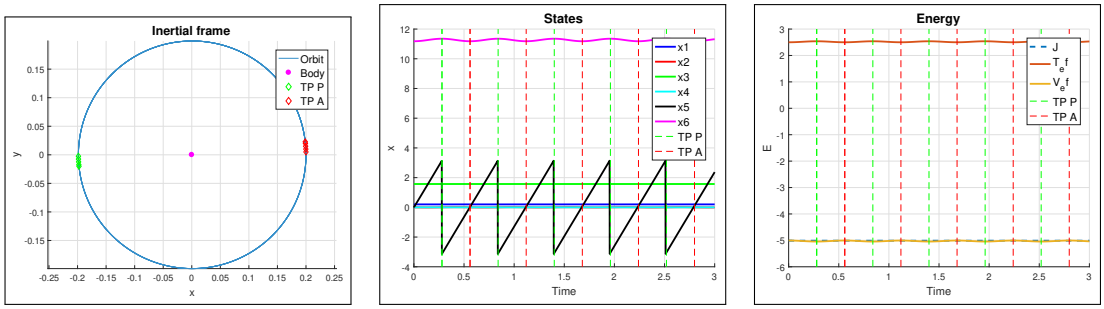

Figure 1.16: Perturbed circular orbit around a single oblate body in its equatorial plane.

an unperturbed Keplerian system. The initial states for this orbit inclined by 45° from the equator are listed in Table 1.3.

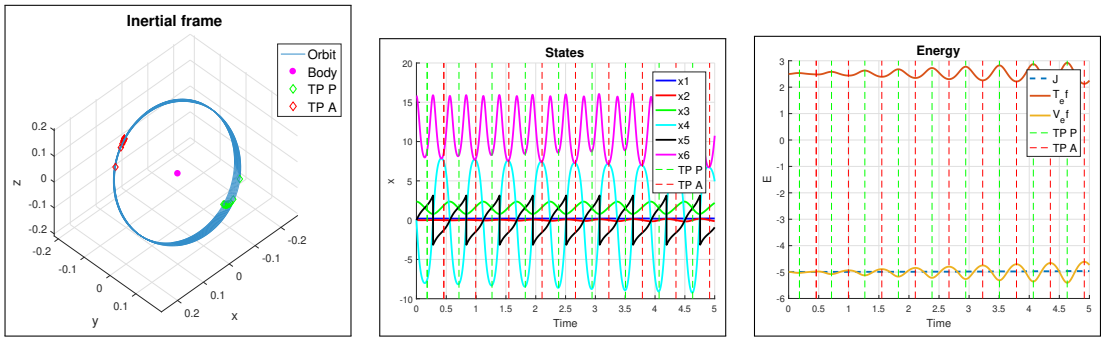

Figure 1.17: Perturbed circular orbit around a single oblate body inclined to its equatorial plane.

The perturbations to the inclined orbit appear more significant than in the case of orbits in the equatorial plane. Not only are the orbit's periapsides and apoapsides precessing, the orbital plane is also shifting. The energy graph of Figure 1.17 show the fluctuation of potential and kinetic energy increases with time, indicating the orbit becomes more and more elliptical. On Figure 1.18, we increased the simulation time to investigate the long-term behaviour of this perturbed orbit.

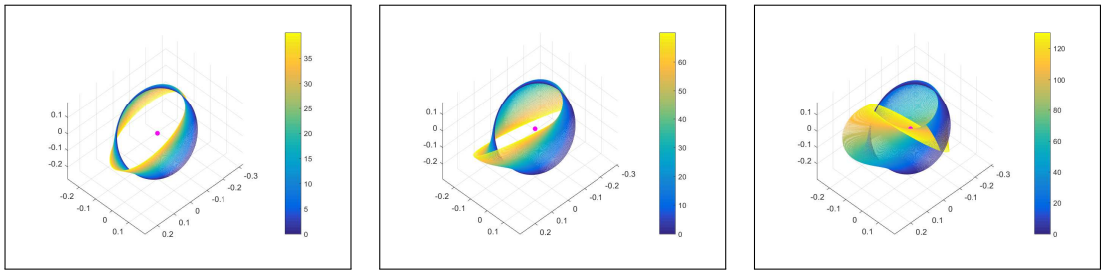

Figure 1.18: Long term behaviour of a perturbed circular orbit around a single oblate body inclined to its equatorial plane. The color scale indicate the evolution of the trajectory in time.

It appears that the orbital plane rotates around the polar axis of the oblate body, while the eccentricity of the orbit successively increases and decreases. The

initial circular shape is elongated into an ellipse of maximum eccentricity attained when the orbital plane rotated by $\pi/2$. The eccentricity then decreases until, after another $\pi/2$ rotation of the plane, a nearly circular shaped is reached again. This behaviour is repeated periodically.

1.4.3 Perturbations due to the second body

As introduced in Section 1.3.3 the Hill's problem consists in deriving the dynamics of a massless particle in the gravitational field of two massive bodies revolving on circular orbits around their mutual centre of mass. The simulations are performed in the co-rotating frame of reference described in Section 1.1.1 according to state equations (1.63). In addition to the rotating frame, the results are also displayed in the inertial centred at the barycentre and non-rotating frame centred at the main body, all three displayed in Figure 1.2. These offer additional insight in cases the motion in the co-rotating frame is not very readable.

This section will present the deformation of Keplerian orbits by the presence of the second body. Unless stated otherwise, the considered reduced mass defined by (1.4) is exaggerated to $\mu = 0.15$ for the disturbances to be clearly visible. In the solar system, only the Pluto-Charon pair have a similar mass ratio, while $\mu_{EM} = 0.01215$ of the Earth-Moon system is a degree of magnitude lower.

	x_{01}	x_{02}	x_{03}	x_{04}	x_{05}	x_{06}	J
Circular	0.2	0	$\pi/2$	0	0	9.1803	-5.4121
Circular inclined	0.2	0	$3\pi/4$	0	0	13.1632	-5.3795
Elliptic	0.2	0	$\pi/2$	0	0	11.3693	-3.7070
Elliptic inclined	0.2	0	$3\pi/4$	0	0	16.0786	-3.6744
Chaotic	0.8424	0	$\pi/2$	0	0	0.1187	-3.1788

Table 1.4: Table of initial states for orbits in the Hill's system

1.4.3.1 Perturbed circular orbit in the principal plane

A Keplerian circular orbit in the equatorial plane was described is Section 1.4.1.1. A similar orbit is simulated in the Hill's system to reveal the influence of the second body on a circular orbit in the plane of revolution of the two bodies. The initial angular velocity (1.100) have to be modified though, as it must take into account the mass of the principal body in terms of reduced mass as well as the rotation of the frame:

$$\dot{\varphi}_{c0} = \frac{1-\mu}{\sqrt{r_0^3}} - \Omega \tag{1.105}$$

The full set of initial states is given in Table 1.4.

At first glance, the orbits displayed on Figure 1.19 appear as unperturbed circles. But closer inspection of Figure 1.20 reveal periodic fluctuations in the velocity states as well as in the energies. When the corresponding turning points are indicated on the trajectory graphs, it is apparent the orbit exhibits an almost regular pear-shaped deformation in the rotating frame. Indeed, the trajectory is elongated in both directions on the principal axis, while flattened at around $\varphi = \pm\pi/3$. Higher values of μ and larger radii of the circular orbit (where

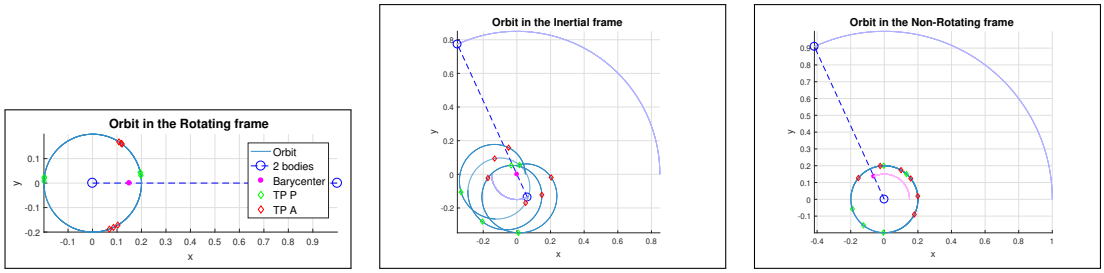

Figure 1.19: Trajectory of a perturbed circular orbit in the principal plane of the Hill's system

the particle pass closer to the second body) make this deformation even more noticeable.

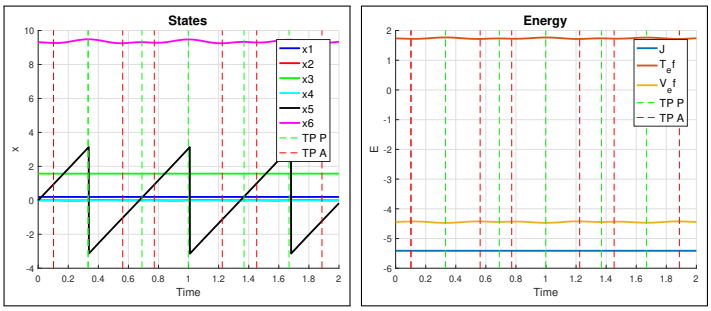

Figure 1.20: States and energy of a perturbed circular orbit in the principal plane of the Hill's system

It is also noteworthy that such an orbit does not leave the plane of revolution of the two bodies. As the initial state vector lies inside this plane and both bodies exerting gravitational pull are by definition bound to it, the force vector component perpendicular to the plane has always zero amplitude.

1.4.3.2 Perturbed circular orbit inclined to the principal plane

Similarly to perturbations due to the oblateness of the main body, orbital planes are not equivalent. Figures 1.21 and 1.22 present the trajectory, states and energy of a deformed circular orbit inclined by 45° with regards to the plane of revolution of the bodies. The orbit radius and initial speed is maintained (Table 1.4).

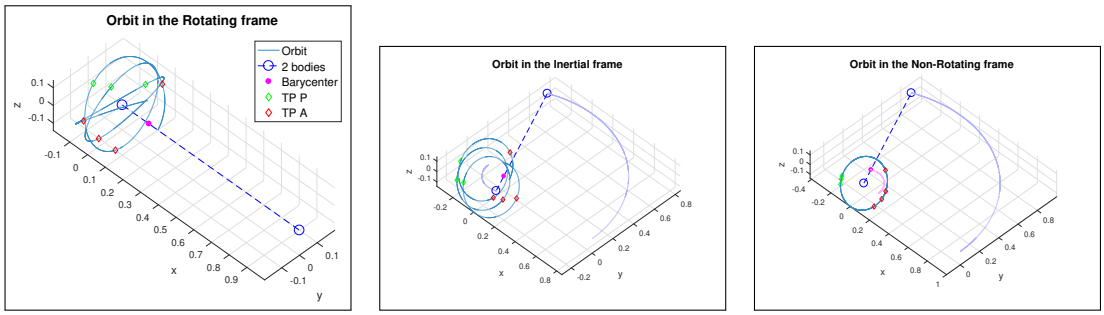

Figure 1.21: Trajectory of a perturbed circular orbit inclined to the principal plane of the Hill's system

As with the orbit in the principal plane described above, the deformation of the circular trajectory is quite small. Contrary to the previous case though, the orbital plane is not constant, as the force vector from the second body is generally not aligned with it. As observable on the trajectory graph in the non-rotating frame, the orbital plane deviate only slightly from its initial position though.

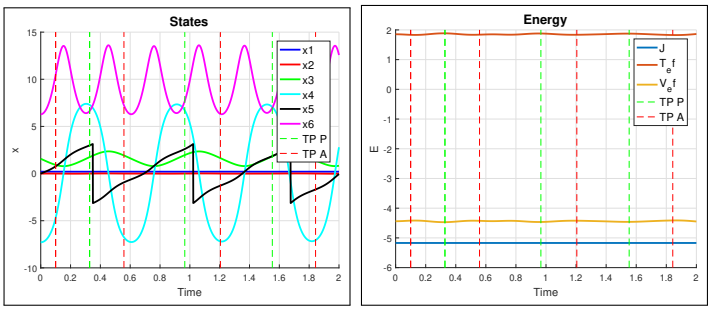

Figure 1.22: States and energy of a perturbed circular orbit inclined to the principal plane of the Hill's system

1.4.3.3 Perturbed elliptic orbit in the principal plane

Circular orbits have been shown to be susceptible to deformation from the gravitational effect or the second body, but their trajectories still maintained an almost circular shape in a plane closer to the initial. The same experiments will be now conducted for elliptic orbit, both in the rotation plane and outside of it.

An elliptic orbit in the bodies plane is simulated with initial specifications equivalent to (1.101) in the Hill's system:

$$\dot{\varphi}_{e0} = 1.2\frac{1-\mu}{\sqrt{r_0^3}} - \Omega \tag{1.106}$$

The full set of initial conditions is given in Table 1.4.

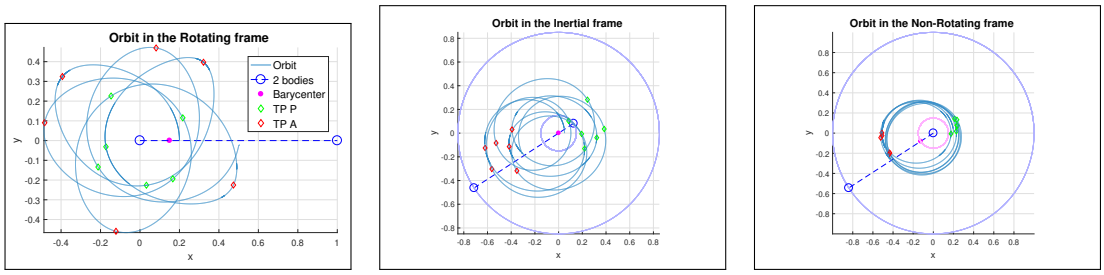

Figure 1.23: Trajectory of a perturbed elliptic orbit in the principal plane of the Hill's system

Results (Figure 1.23) show a strongly deformed elliptic orbit. Two major effects are noticeable. The periapsides and apoapsides or the ellipse precess in the direction of the frame rotation. Meaning particles orbiting in the opposite direction will precess the same way.

A purely precessing elliptic orbit would still maintain some of its regularity. However, it is clear from the trajectory graphs as well as from Figure 1.24 that this is not the case here. As orbits are more subject to perturbation from the

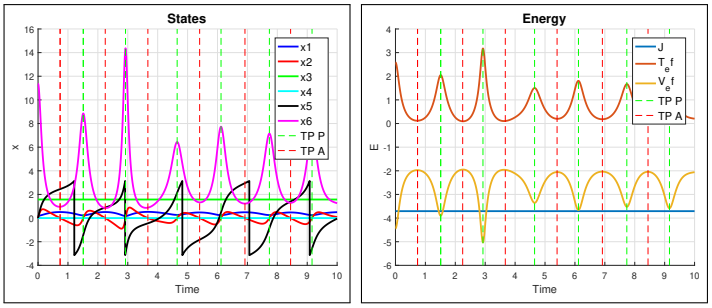

Figure 1.24: States and energy of a perturbed elliptic orbit in the principal plane of the Hill's system

second point mass when they are closer to it, an ellipse feels this effect the most when their apoapsis is directed towards the body. This causes the perturbations to vary in intensity based on the orientation of the ellipse and its shape becoming irregular.

1.4.3.4 Perturbed elliptic orbit inclined to the principal plane

Elliptic orbits in the Hill's system in an inclined plane are subject to the same deformation effect as the ellipse in the plane treated above. In addition to the precession and ellipse deformation, the orbital plane is not constant any-more. The perturbation to this orbital plane is more significant in this case compared to the circular orbit, due once again to the fact its apoapsis brings it closer to the second body, where it is influenced the most.

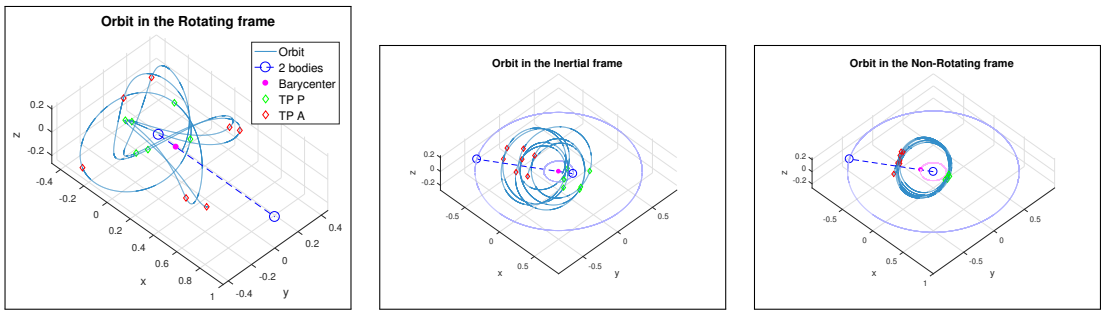

Figure 1.25: Trajectory of a perturbed elliptic orbit inclined to the principal plane of the Hill's system

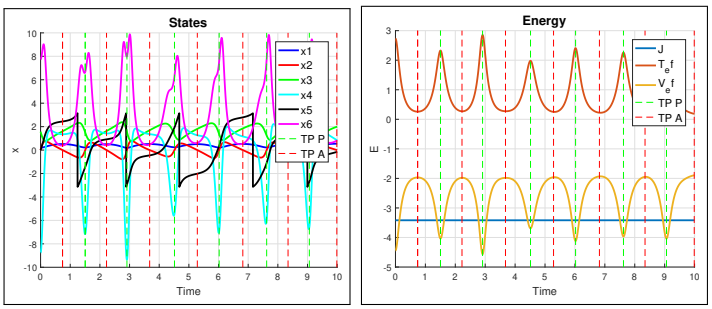

Figure 1.26: States and energy of a perturbed elliptic orbit inclined to the principal plane of the Hill's system

1.4.4 Chaotic orbit

In addition to the second body acting as a mere source of perturbation to an otherwise almost Keplerian orbit, trajectories in the restricted three-body problem can have more exotic shape and characteristics. One category of such orbits are *chaotic* orbits. The precise definition of chaotic orbits is still under debate, so for the purposes of this thesis, we will present an orbit introduced as chaotic in [10]. Its specification in terms of initial conditions and Jacobi integral is given in Table 1.4. As this orbit is said to be chaotic in the Earth-Moon system, the reduced mass is set to $\mu = 0.01215$.

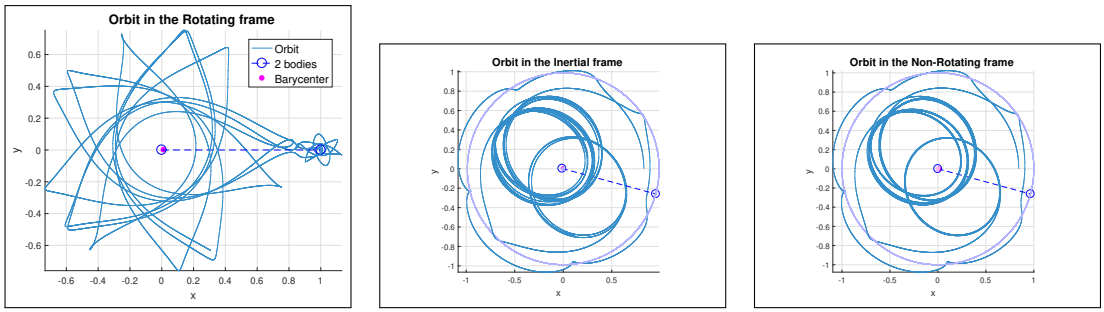

Figure 1.27: Trajectory of a chaotic orbit in the principal plane of the Hill's system

Figure 1.27 shows a complex trajectory, orbiting alternatively one body before jumping into an orbit of the another. Around the main body, it appears to follow successively three different elliptic orbits before being pulled away from them.

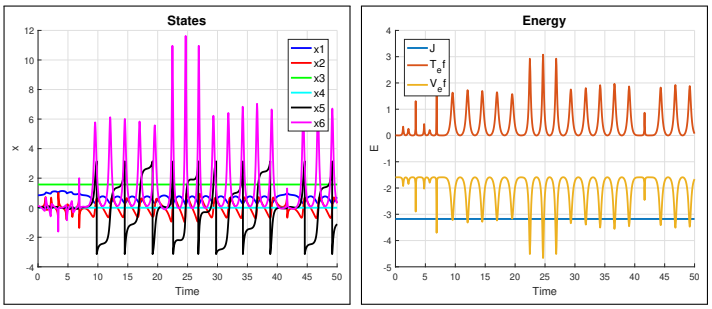

Figure 1.28: States and energy of a chaotic in the principal plane of the Hill's system

A property of chaotic orbits is sensitivity to initial conditions. A trajectory starting arbitrarily close to a chaotic orbit will quickly diverge. This makes tracking bodies on chaotic orbits difficult, as even small errors in measurement will result in large errors in their predicted trajectories. In the solar system, there exists a number of asteroids on chaotic orbits. As their long-time trajectory is not easily predictable and some of them might cross the Earth's orbits, their study is of prime importance.

In Section 2.3.5, we will present an orbit transfer simulating an attempt to intercept such an asteroid by a spacecraft.

1.4.5 Lagrange points

In Section 1.3.3.5, the term Lagrange point was introduced as a set of five equilibrium positions in the Hill's system. This section will present the trajecto-

ries of Lagrange point orbits as well as bring illustrative examples of halo orbits around those Lagrange points.

1.4.5.1 Orbits at Lagrange points

Using the method describe in Section 1.3.3, all Lagrange points for $\mu = 0.15$ are found and recorded in Section 1.3.3.5, Table 1.1. Their status as equilibria is confirmed experimentally by simulating the system (1.63) for initial conditions at the Lagrange points.

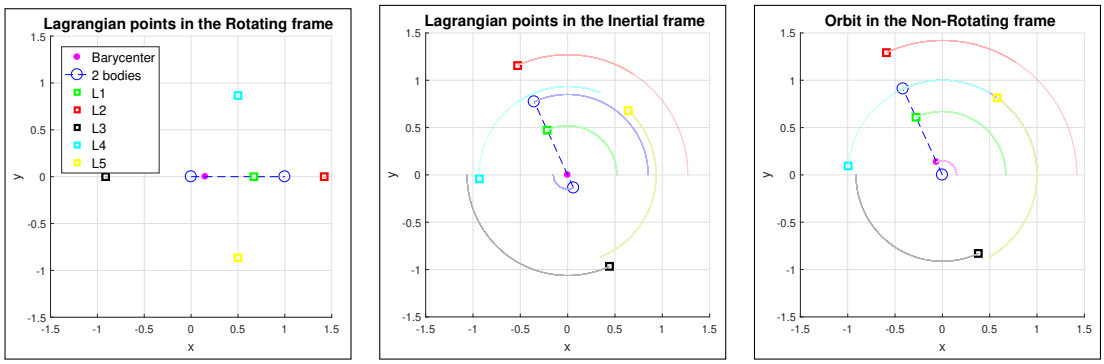

Figure 1.29: Trajectory of particles at Lagrange points

Indeed, trajectories of particles starting at Lagrange points (Figure 1.29) will stay fixed in the rotating frame. Due to the nature of the rotating frame, this will translate to a circular motion around the barycentre at the same angular speed as the bodies in the inertial frame. Transfers from circular orbits to Lagrange points will be the topic of Section 2.3.3.

1.4.5.2 Halo orbits

Placing a satellite at Lagrange point equilibria is a useful energy efficient strategy to achieve a fixed position in the rotating frame of the Hill's problem. It has its drawback however, beyond the obvious reason that each equilibrium can hold only a single satellite. It was discussed in Section 1.3.3.5 that satellite placed at the unstable Lagrange points L1-3 of a star-planet system suffer from either shading from the star by the planet (L3) or strong stellar radiation interference preventing efficient communication with the planet (L1 and L2).

It is however possible to find trajectory solutions that orbit the Lagrange points, possibly solving the above-mentioned issues. These orbits forming periodic trajectories in the rotating frame are called *halo* orbits. As halo orbits around unstable equilibriums are themselves unstable, they require station keeping to maintain their shapes. A comprehensive classification of halo orbits, their properties and stability, is offered by [3]. In this thesis, we will use initials conditions of various types of halo orbits introduced in [3] (and recorded in Table 1.5) to present a selection of distinct halo orbits. As with the chaotic orbit, the initial specifications are given in the Earth-Moon system ($\mu = 0.01215$).

In Section 2.3.4, orbit transfers to some of the following halo orbits will be discussed, indicating possible cost-optimal trajectories a spacecraft might take to reach them.

	x_{01}	x_{02}	x_{03}	x_{04}	x_{05}	x_{06}	J
L1 - Lyapunov	0.8356	0	$\pi/2$	0	0	0.1512	-3.1744
L1 - Vertical	0.9075	0	1.3583	0	0	0.2621	-2.9979
L2 - Butterfly	1.0386	0	1.4026	0	0	-0.0780	-3.0580
L3 - Vertical	0.9935	0	0.9020	0	π	0.2731	-2.5829
L3 - Lyapunov	1.3030	0	$\pi/2$	0	π	-0.4536	-2.9071

Table 1.5: Table of initial conditions for halo orbits around Lagrange points for $\mu = 0.01215$

A Lyapunov class orbit around L1 is presented on Figure 1.30 and 1.31. Halo orbits of the Lyapunov type are bean-shaped regular orbits inside the principal plane of the Hill's system. This particular orbit is very unstable, lasting only a few periods before breaking off from its Lagrange point.

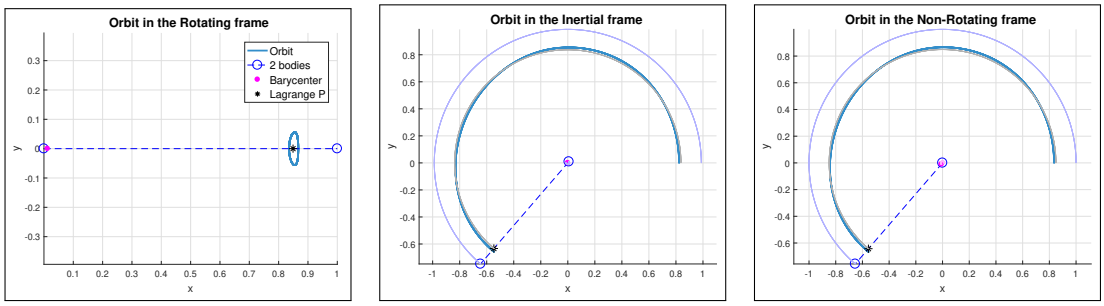

Figure 1.30: Trajectory of a Lyapunov halo orbit around L1

Even though we say the particle orbits around L1, this is not exactly correct, as L1 is a virtual mass-less point. In reality, all particles on halo orbits orbit the centre of mass of both bodies on various deformed quasi-circular orbits, as can be seen of figures in the inertial frame. However, in the rotating frame, they appear to orbit around equilibrium points.

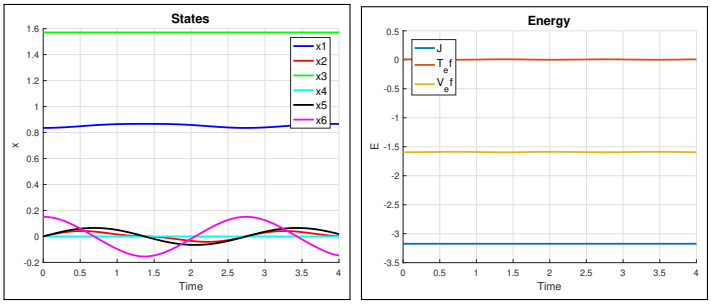

Figure 1.31: States and energy of a Lyapunov halo orbit around L1

Halo orbits are not exclusively located in the principal plane. Figures 1.32 and 1.33 show an example of a vertical halo orbit at L1. Such orbits are vertical or diagonal loops between L1 and the second body. An orbit transfer to the vertical orbit at L1 shown on Figure 1.32 will be presented in Section 2.3.4.2.

Halo orbits of the butterfly class are 8-shaped loops with both ends lifted, resembling butterfly wings. The An example of this type of orbit at L2 is depicted on Figures 1.34 and 1.35.

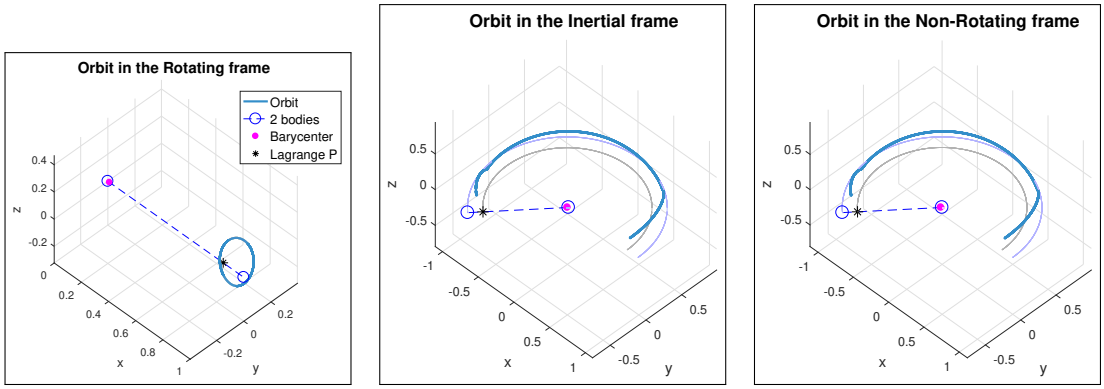

Figure 1.32: Trajectory of a vertical halo orbit around L1

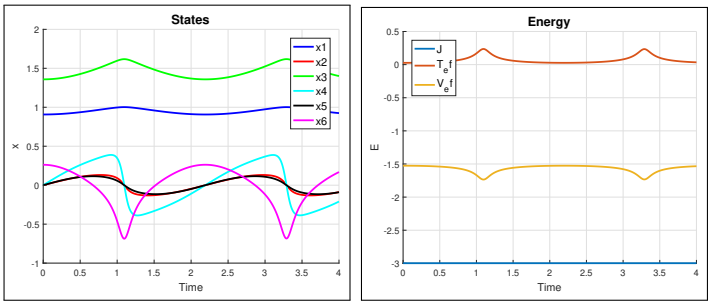

Figure 1.33: States and energy of a vertical halo orbit around L1

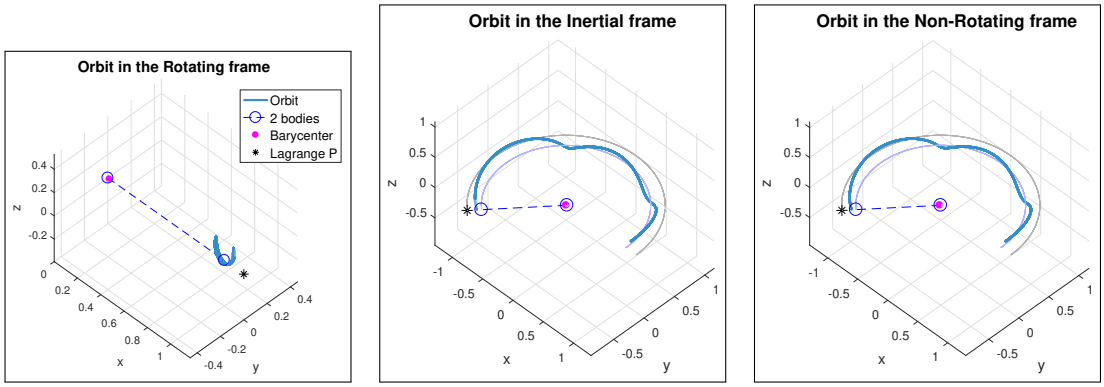

Figure 1.34: Trajectory of a butterfly halo orbit around L2

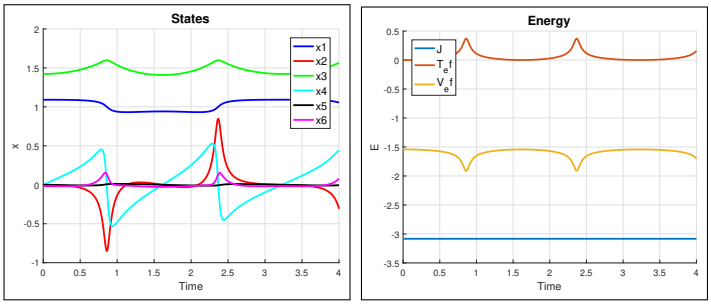

Figure 1.35: States and energy of a butterfly halo orbit around L2

Halo orbits around the Lagrange point L3 are usually more stable than their counterparts at L1 and L2 [3]. This allows them to remain longer in their original shape or, alternatively, require less orbit maintenance energy to be kept there.

Figures 1.36 and 1.37 describe a Lyapunov orbit at L3. Just like the previous Lyapunov orbit, it stays in the principal plane.

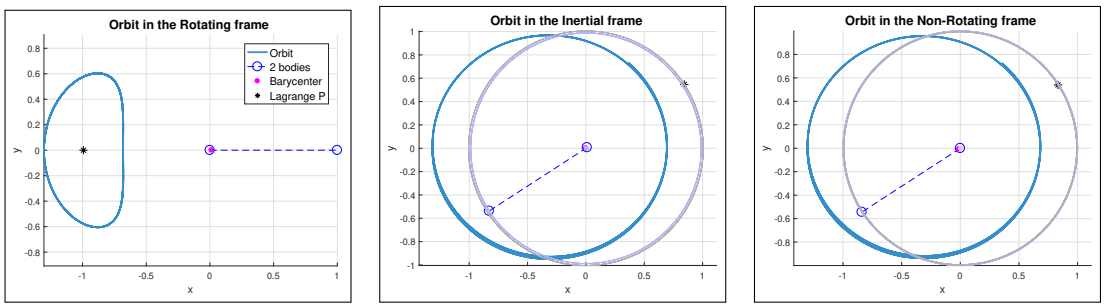

Figure 1.36: Trajectory of a Lyapunov halo orbit around L3

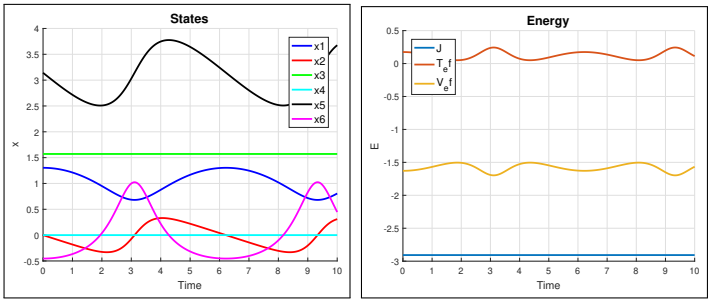

Figure 1.37: States and energy of a Lyapunov halo orbit around L3

Vertical orbits around L3 form vertical 8-shaped figures in the rotating frame with the extremities bent towards the bodies and the intersections of both loops located at L3. In the inertial frame, they are quasi-circular inclined trajectories around the barycentre.

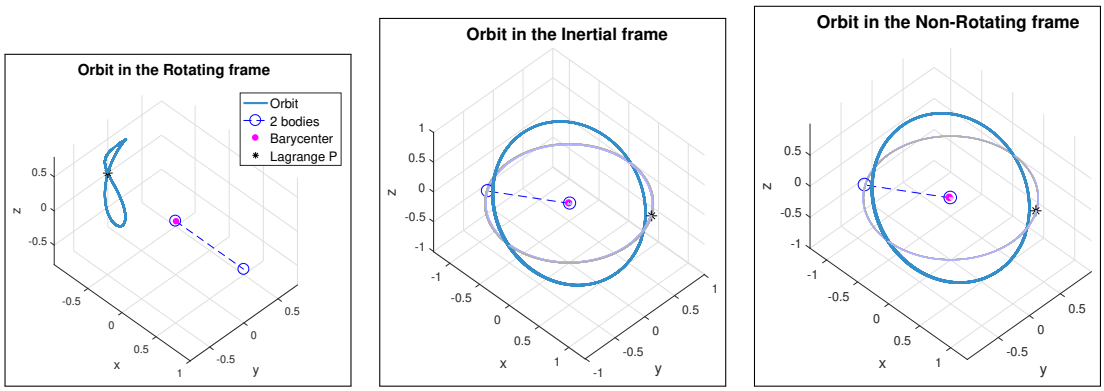

Figure 1.38: Trajectory of a vertical halo orbit around L3

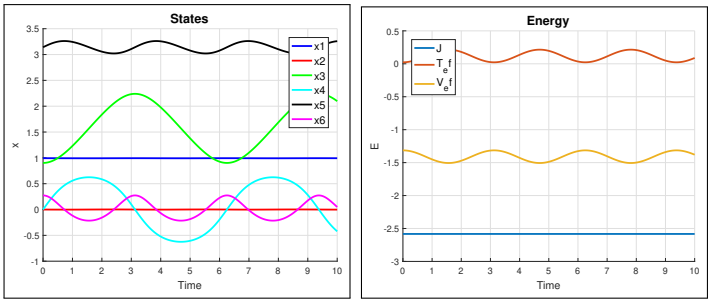

Figure 1.39: States and energy of a vertical halo orbit around L3

1.5 Conclusion

Orbital mechanics describe the motion of celestial bodies and man-made satellites in their gravitational fields. This chapter has treated the dynamics of massless particles subjected to gravitational forces.

Section 1.1 has presented the various coordinate systems used in this theses. Lagrangian mechanics, introduced in Section 1.2, presents a good methodical tool for deriving equations of motion in arbitrary coordinates. In Section 1.3, the dynamics for a massless particle in a gravitational field were obtained. Various orbital trajectories were then presented in Section 1.4 by simulating the acquired equations of motion This allowed visualizing distinct orbital shapes and the effects of perturbing elements, such as the oblateness of one of the bodies or the presence of a second mass point.

In the next chapter, an optimal controller will be designed and applied to obtain transfer trajectories between the orbits presented above. Chapter 3 will place formations of satellites on some of these orbits and perform formation reconfiguration and maintenance manoeuvre on them.

Chapter 2

Optimal control for orbit placement

The Apollo program was a successful NASA mission in the 60' aiming at taking a manned spacecraft to the Moon and back. Designing a control system to achieve this goal was no easy task. Available fuel reserves were severely limited by the size of the module and the payload capacity of the launcher. A trajectory had to be designed that was as fuel-efficient as possible. Limitations in various systems of the spacecraft also had to be taken into account, such as the limited computation power of onboard computers as well as restricted communication capabilities. Having humans on board also presented a number of considerable constraints. The cockpit, oxygen tanks and other support modules had to be accommodated in the spacecraft. The limited supplies of oxygen and sustenance signified the mission time was also an important consideration. Manned spacecraft are also constrained in their maximal acceleration so that it remains in bounds tolerable to the human body. Solving this complex task was beyond the scope of the control theory discipline at that time. Keeping fuel expenditure low while limited by time and a multitude of other constraints required the development of new tools for control. Although they built on the early works of Rudolf E. Kálmán and others, the efforts of space agencies to find solutions to complex constrained problems spearheaded the advent of the optimal control field.

Optimal control theory is a field of control engineering studying methods for finding control laws for a possibly constrained system such that a certain optimality criterion is achieved[6]. The output of an optimal controller is a sequence of control inputs that steers a system from its initial state to a desired final state while satisfying all constraints and minimizing an optimality criterion (called *Performance index* in this thesis). In order to minimize the criterion, the entire trajectory has to be designed as a whole, which signifies it is an open-loop process.

In the celestial mechanics context, optimal control is applied to find transfer trajectories between two orbits. This chapter will discuss the development of a method of optimal control for single particle transfers. Although the designed controller is applied on individual particles, it has its uses in satellite formation flying as well. Formation installation manoeuvres, where the bodies are put on the formation orbits from the launch site, or large reconfigurations are costly and usually require only the end state to form a coordinated configuration. It therefore might be a good idea to use optimal control tools to plan a large part

of the transfer trajectory before involving close-loop controllers to ensure the formation fall into place.

In Section 2.1, we will introduce the method used to derive the optimally controlled model, presented in Section 2.2. We will then perform simulation experiments to verify the designed controller by generating transfer trajectories between some of the orbits described in the previous chapter.

2.1 Theory

Even the simplest Keplerian model of orbital motion introduced in 1.3.1 is highly non-linear, thus ruling out the possibility of using standard tools of optimal control of linear dynamical systems, such as the Linear-Quadratic Regulator [5], for solving optimal transfers between two orbits. It is possible to devise a non-optimal controller linearised around a particular orbit. Its usability is however restricted to mostly small maintenance manoeuvres around the orbit. Such a regulator is derived and compared with the optimal controller introduced in this chapter in Section 3.3.

This chapter applies tools of optimal control presented in [6] in order to design a fixed-time optimal controller for minimum-fuel orbit transfer in both the Keplerian system and the more complex Hill's system with the oblateness of the principal body included. The rotating coordinate frame introduced in Section 1.1.1 facilitates the three-body task by making the system dynamics time-invariant. The equations of motion of a controlled time-invariant system can be written as

$$\dot{\boldsymbol{x}}(t) = g(\boldsymbol{x}(t), \boldsymbol{u}(t)) = f(\boldsymbol{x}(t)) + B\boldsymbol{u}(t) \tag{2.1}$$

where $\boldsymbol{x}$ is the state vector, $f(\boldsymbol{x})$ are the uncontrolled dynamics of the system (in case of the motion of a particle in the Hill's system, these equations are given by (1.63)), $\boldsymbol{u}$ is the control input vector and B is the input matrix.

A minimum-fuel system is such a control system that uses as little control input as possible to achieve a goal state. This can be formally described as a minimization of the performance index P

$$P = \int_{t_0}^{T} L(\boldsymbol{x}, \boldsymbol{u}, t)\, \mathrm{d}t \tag{2.2a}$$

$$L = \boldsymbol{u}(t)^T \boldsymbol{R}\boldsymbol{u}(t) = \sum_i R_i u_i(t)^2 \tag{2.2b}$$

where $[t_0, T]$ is the time interval allocated to the transfer, $\boldsymbol{u}(t)$ the control applied and $\boldsymbol{R}$ the weight vector of the controls. The weighting function $L(\boldsymbol{x}, \boldsymbol{u}, t)$ represents the immediate fuel consumption at time t. Sometimes, $|u_i|$ is used in (2.2) instead of $u_i(t)^2$. We decided to square the control input to make the equation easily differentiable in (2.6). Another effect of this is that an optimal solution according to this performance index will prefer smaller amplitudes of control input delivered over a longer time to shorter, more powerful bursts.

The optimal control problem consists in finding the input sequence $\boldsymbol{u}^*(t)$ on the time interval $[t_0, T]$ that drives the system (2.1) along a trajectory $\boldsymbol{x}^*(t)$ such that the performance index (2.2) is minimized, and such that the final state function

$$\psi(\boldsymbol{x}(T)) = \boldsymbol{0} \tag{2.3}$$

is satisfied. This is done by finding the Lagrange multipliers $\boldsymbol{\lambda}(t)$ enabling the system satisfy (2.3) at a specified time T. The multipliers form a time-varying vector of costates in with every element representing the Lagrange multiplier associated with a corresponding state from $\boldsymbol{x}(t)$.

We define the Hamiltonian function as

$$H(\boldsymbol{x},\boldsymbol{\lambda},\boldsymbol{u},t) = L(\boldsymbol{x},\boldsymbol{u},t) + \boldsymbol{\lambda}^T g(\boldsymbol{x},\boldsymbol{u}) \tag{2.4}$$

We can then describe the entire controlled system in terms of state and costate dynamics:

$$\dot{\boldsymbol{x}} = \frac{\partial H}{\partial \boldsymbol{\lambda}} = g(\boldsymbol{x},\boldsymbol{u}) \tag{2.5a}$$

$$\dot{\boldsymbol{\lambda}} = -\frac{\partial H}{\partial \boldsymbol{x}} = -\frac{\partial g}{\partial \boldsymbol{x}}^T \boldsymbol{\lambda} - \frac{\partial L}{\partial \boldsymbol{x}} = -\frac{\partial g}{\partial \boldsymbol{x}}^T \boldsymbol{\lambda} \tag{2.5b}$$

with the input vector given by the solution of

$$\frac{\partial H}{\partial \boldsymbol{u}} = \mathbf{0} \tag{2.6}$$

An important property of the Hamiltonian function of a time-invariant system is that it is constant throughout the transfer time interval $[t_0,T]$.

$$\frac{\mathrm{d}H}{\mathrm{d}t} = \frac{\partial H}{\partial \boldsymbol{x}}\dot{\boldsymbol{x}} + \frac{\partial H}{\partial \boldsymbol{\lambda}}\dot{\boldsymbol{\lambda}} + \frac{\partial H}{\partial \boldsymbol{u}}\dot{\boldsymbol{u}} + \frac{\partial H}{\partial t} \tag{2.7}$$

By inserting equations (2.5) and (2.6) into (2.7):

$$\frac{\mathrm{d}H}{\mathrm{d}t} = \frac{\partial H}{\partial \boldsymbol{x}}\frac{\partial H}{\partial \boldsymbol{\lambda}} - \frac{\partial H}{\partial \boldsymbol{\lambda}}\frac{\partial H}{\partial \boldsymbol{x}} + \mathbf{0}\dot{\boldsymbol{u}} + \frac{\partial H}{\partial t} = \frac{\partial H}{\partial t} = 0 \tag{2.8}$$

$\frac{\partial H}{\partial t} = 0$ holds true because our system is time-invariant, H does not depend directly on t. We can conclude that the Hamiltonian is a value that stays constant for the duration of the transfer.

2.1.1 Optimization of initial costates

As stated above, finding a solution to the optimal control problem consists in finding the costate vector $\boldsymbol{\lambda}^*(t)$ that drives the system optimally from its initial state to a final state satisfying the final state function (2.3). As variations to costates at any given time are entirely given by the current states and costates according to (2.5), only the initial set of costates is free to be chosen. This greatly simplifies the task, as the entire control sequence is defined by tuning N initial conditions for the Lagrange multipliers, where N is the number of states of the system.

There are numerous techniques available for such a parameter optimization. We opted for a gradient descent method because the gravitational field in which the controlled particle moves is largely monotonic, thus following the steepest gradient should converge to a good, if not always globally optimal, solution. There is however still a danger of falling into a local minimum. In order to minimize this risk, it is advised to run the method multiple time with various initializations

of the initial costate vector and choose the best alternative. From the performed experiments, we discovered that varying the initial costates makes the system converge to only a handful of locally optimal solutions, differing in general in the number of times the particle revolves around the body before reaching its target state. The used technique is described by Algorithm 1.

Result: Find a set of initial costates $\boldsymbol{\lambda}_{opt}$ such that the final state function is satisfied.
simulate model with $\boldsymbol{\lambda}_{init}$;
$\boldsymbol{p}_k = \boldsymbol{p}(T)$;
$\boldsymbol{\lambda}_k = \boldsymbol{\lambda}_{init}$;
while $\psi(\boldsymbol{p}_k) \neq \mathbf{0}$ **do**
  for $i := 1 : N$ **do**
    simulate model with $\delta\boldsymbol{\lambda}_k(i)$;
    $J(:,i) = \boldsymbol{p}(T) - \boldsymbol{p}_k$;
  end
  $\boldsymbol{\lambda}_k = \boldsymbol{\lambda}_k + \alpha J^{+}(\boldsymbol{p}_g - \boldsymbol{p}_k)$;
  simulate model with $\boldsymbol{\lambda}_k$;
  $\boldsymbol{p}_k = \boldsymbol{p}(T)$;
end
$\boldsymbol{\lambda}_{opt} = \boldsymbol{\lambda}_k$

Algorithm 1: Gradient descent algorithms to find an optimal set of initial costates. Costate vectors of size N are represented by $\boldsymbol{\lambda}$, modified state vectors are $\boldsymbol{p}$. α is the approach step size parameter, $\delta\boldsymbol{\lambda}_k(i)$ is the costate vector $\boldsymbol{\lambda}_k$ with a slight deviation at the i^{th} position, J is the Jacobi matrix.

The gradient descent algorithm produces an initial costate vector $\boldsymbol{\lambda}_{opt}$ that ensures that the end state satisfies 2.3. We call such a goal state $\boldsymbol{x}_g$. For some applications, $\boldsymbol{x}_g$ represents a unique solution of 2.3, as is the case for transfers to Lagrange points (Section 2.3.3) or formation reconfiguration problems (Section 3.2 of the chapter of formation flying). In other cases however, the final state function can be less specific and the goal state is not unique. An example of this situation might be a transfer to a different orbit (Section 2.3.1), where we usually don't care about the value of the true anomaly at the and of the manoeuvre.

We need however to define the goal state in some way to be able to build a gradient and stir the system towards it. The introduction of a *modified state* vector $\boldsymbol{p}(t)$ solves this issue. The modified state is obtained by transforming the actual state $\boldsymbol{x}(t)$ to be able to express a unique goal state $\boldsymbol{p}_g$. A simple example of this might be the modified state describing a circular orbit in the equatorial plane:

$$\boldsymbol{p} = \begin{bmatrix} x_1 \\ x_2 \\ x_3 \\ x_4 \\ x_6 \end{bmatrix} \tag{2.9}$$

where the modified state adopts every element of the actual state except x_5 ($x_5 = \varphi$). By omitting this state, the desired orbit can be exactly specified and the system will be steered toward any point of that circle. Introducing a modified

state also permits to define orbits inclined with regards to the equatorial plane or centred around a point different from the origin of the coordinate system (when transferring to orbits around the second body for example, as will be done in Section 2.3.2). The coordinates of the actual state might be transformed so that the target orbit is located in the principal plane of the new coordinate system and centred around its origin.

The final state function (2.3) indicating whether the goal state has been reached can then be uniquely expressed in terms of modified states:

$$\psi\left(\boldsymbol{p}\left(T\right)\right) = \boldsymbol{p} - \boldsymbol{p}_g = \mathbf{0} \tag{2.10}$$

2.2 Derivation of control laws

In the previous section, we introduced a method for generating control sequences that bring the system into a desired state while satisfying some optimality criterion. We will now apply this method to design a controlled model from the model of uncontrolled particles in a gravitational field introduced in Chapter 1, Section 1.3. These models will be used in Section 2.3 to study concrete orbit transfers.

2.2.1 Control input

Starting from the Newton's laws one has that in any Galilean system the total change of the linear momentum equals the effect of the total external force acting on the system. The idea is that the external forces come from the gravitating bodies, and are modelled through the potential. This would include the thrust force and gravity in a single consideration; allowing to join them seamlessly.

$$\begin{aligned}
\mathrm{d}p_{tot} = F_{e_tot}\mathrm{d}t &= (m - \mathrm{d}m)\,(v + \mathrm{d}v) + \mathrm{d}m\,(v - v_e) - mv \\
&= (m - \mathrm{d}m)\,(v + \mathrm{d}v) + \mathrm{d}m\,(v - v_e) - mv \\
&= mv - v\mathrm{d}m + m\mathrm{d}v + \mathrm{d}m\mathrm{d}v + v\mathrm{d}m + v_e\mathrm{d}m - mv \\
&= m\mathrm{d}v + v_e\mathrm{d}m \\
m\frac{\mathrm{d}v}{\mathrm{d}t} &= F_{e_tot} - v_e\frac{\mathrm{d}m}{\mathrm{d}t} \\
\frac{\mathrm{d}v}{\mathrm{d}t} &= f_{e_tot} - v_e\frac{1}{m}\frac{\mathrm{d}m}{\mathrm{d}t}
\end{aligned} \tag{2.11}$$

Now if one models the total external force per unit mass f_{e_tot} as coming from the potential, or describes it completely using the Lagrangian one ends up with the extra force coming from thrust.

$$\frac{\mathrm{d}v}{\mathrm{d}t} - f_{e\_tot} = -v_e\frac{1}{m}\frac{\mathrm{d}m}{\mathrm{d}t} \tag{2.12}$$

Hence the additional force per unit mass from the thrust is

$$f_{thrust} = -v_e\frac{1}{m}\frac{\mathrm{d}m}{\mathrm{d}t} = -v_e\frac{\dot{m}}{m} \tag{2.13}$$

or in Cartesian components

$$f_{thrust_x} = -v_{ex}\frac{\dot{m}}{m} \qquad f_{thrust_y} = -v_{ey}\frac{\dot{m}}{m} \qquad f_{thrust_z} = -v_{ez}\frac{\dot{m}}{m} \tag{2.14}$$

depending directly on the components of exhaust gas velocity.

All these relations are derived in Cartesian coordinates; switching to the Lagrangian framework, using the generalized coordinates, $q_i\,(x,t)$, one has the Lagrange equations with additional generalized force terms Q_i

$$\frac{\mathrm{d}}{\mathrm{d}t}\frac{\partial L}{\partial \dot{\boldsymbol{q}}} - \frac{\partial L}{\partial \boldsymbol{q}} = Q_i \tag{2.15}$$

where the expression for the generalized force, per unit mass, components in terms of the original force components are

$$Q_i = \sum_j f_j \frac{\partial x_j}{\partial q_i} \tag{2.16}$$

So, in case of spherical coordinates, the generalized forces become:

$$\begin{aligned}
Q_r &= f_x\frac{\partial x}{\partial r} + f_y\frac{\partial y}{\partial r} + f_z\frac{\partial z}{\partial r} = f_x\sin\vartheta\cos\varphi + f_y\sin\vartheta\sin\varphi + f_z\cos\vartheta \\
Q_\vartheta &= f_x\frac{\partial x}{\partial \vartheta} + f_y\frac{\partial y}{\partial \vartheta} + f_z\frac{\partial z}{\partial \vartheta} = f_x r\cos\vartheta\cos\varphi + f_y r\cos\vartheta\sin\varphi - f_z\sin\vartheta \\
Q_\varphi &= f_x\frac{\partial x}{\partial \varphi} + f_y\frac{\partial y}{\partial \varphi} + f_z\frac{\partial z}{\partial \varphi} = f_x r\sin\vartheta\sin\varphi + f_y r\sin\vartheta\cos\varphi + f_z\cdot 0
\end{aligned} \tag{2.17}$$

according to the coordinate transformation (1.1).

After appropriate divisions, used in obtaining the original second order differential equations from the spherical polar coordinates, these generalized force per unit mass components express the control inputs labelled simply as u_1, u_2 and u_3.

2.2.2 Optimal control in the two-body Keplerian system

The state-space model of a controlled particle in the Keplerian system described in Section 1.3.1 is obtained by combining the uncontrolled dynamics (1.30) and the control input vector into the general relation (2.1)

$$\dot{\boldsymbol{x}} = \begin{bmatrix} \dot{x}_1 \\ \dot{x}_2 \\ \dot{x}_3 \\ \dot{x}_4 \\ \dot{x}_5 \\ \dot{x}_6 \end{bmatrix} = \begin{bmatrix} x_2 \\ x_1 x_4^2 - \frac{1}{x_1^2} + x_1\sin^2 x_3 x_6^2 \\ x_4 \\ -2\frac{x_2}{x_1}x_4 + \cos x_3 \sin x_3 x_6^2 \\ x_6 \\ -2\left(\frac{x_2}{x_1} + x_4\frac{\cos x_3}{\sin x_3}\right)x_6 \end{bmatrix} + \begin{bmatrix} 0 & 0 & 0 \\ 1 & 0 & 0 \\ 0 & 0 & 0 \\ 0 & 1 & 0 \\ 0 & 0 & 0 \\ 0 & 0 & 1 \end{bmatrix} \begin{bmatrix} u_1 \\ u_2 \\ u_3 \end{bmatrix} \tag{2.18}$$

The Hamiltonian function of this model is derived by inserting the above state

equation into (2.4):

$$\begin{aligned} H =& R_1 u_1^2 + R_2 u_2^2 + R_3 u_3^2 \\ &+\lambda_1 x_2 \\ &+\lambda_2 \left(x_1 x_4^2 - \frac{1}{x_1^2} + x_1 \sin^2 x_3 x_6^2 \right) \\ &+\lambda_3 x_4 \\ &+\lambda_4 \left(-2\frac{x_2}{x_1} x_4 + \cos x_3 \sin x_3 x_6^2 \right) \\ &+\lambda_5 x_6 \\ &+\lambda_6 \left(-2 \left(\frac{x_2}{x_1} + x_4 \frac{\cos x_3}{\sin x_3} \right) x_6 \right) \end{aligned} \tag{2.19}$$

The expression for the costate dynamics of a controlled particle in a Keplerian system is obtained from (2.5)

$$\begin{bmatrix} \dot{\lambda}_1 \\ \dot{\lambda}_2 \\ \dot{\lambda}_3 \\ \dot{\lambda}_4 \\ \dot{\lambda}_5 \\ \dot{\lambda}_6 \end{bmatrix} = \begin{bmatrix} -\lambda_2 \left(\frac{2}{x_1^3} + x_4^2 + x_6^2 \sin^2 x_3 \right) - 2\lambda_4 \frac{x_2 x_4}{x_1^2} - 2\lambda_6 \frac{x_2 x_6}{x_1^2} \\ -\lambda_1 + 2\lambda_4 \frac{x_4}{x_1} + 2\lambda_6 \frac{x_6}{x_1} \\ -\lambda_2 x_1 x_6^2 \sin 2x_3 - \lambda_4 x_6^2 \cos 2x_3 + \lambda_6 \frac{4 x_4 x_6}{\cos 2x_3 - 1} \\ -2\lambda_2 x_1 x_4 - \lambda_3 + 2\lambda_4 \frac{x_2}{x_1} + 2\lambda_6 x_6 \frac{\cos x_3}{\sin x_3} \\ 0 \\ -2\lambda_2 x_1 x_6 \sin^2 x_3 - 2\lambda_4 x_6 \sin x_3 \cos x_3 - \lambda_5 + 2\lambda_6 \left(\frac{x_2}{x_1} + x_4 \frac{\cos x_3}{\sin x_3} \right) \end{bmatrix} \tag{2.20}$$

The control input vector in spherical coordinates, as described in Section 2.2.1, is calculated by solving (2.6)

$$\begin{bmatrix} u_1 \\ u_2 \\ u_3 \end{bmatrix} = \begin{bmatrix} -\lambda_2 \frac{1}{2R_1} \\ -\lambda_4 \frac{1}{2R_2} \\ -\lambda_6 \frac{1}{2R_3} \end{bmatrix} \tag{2.21}$$

2.2.3 Optimal control in the three-body Hill's system

The model of a controlled particle in the Hill's system is derived using the same procedure as in the previous section. Compared to the Keplerian case however, the expressions below are longer and more complicated, which is why we computed them using Matlab's Symbolic Math Toolbox and present them below in their unsimplified form.

The space-state equations are obtained by insertion of the uncontrolled model

(1.63) into Equation (2.1)

$$
\begin{aligned}
\dot{x}_1 =& x_2 \\
\dot{x}_2 =& x_1 x_4^2 - \frac{1-\mu}{x_1^2} - \frac{\mu x_1}{\sqrt{1 + x_1^2 - 2x_1 \sin x_3 \cos x_5}^3} + x_1 \sin^2 x_3 \left(x_6 + \Omega\right)^2 \\
& + \mu \sin x_3 \cos x_5 \left(\frac{1}{\sqrt{1 + x_1^2 - 2x_1 \sin x_3 \cos x_5}^3} - \Omega^2 \right) \\
& + (1-\mu) \frac{3}{2} \frac{a}{x_1^4} \left(3\cos^2 x_3 - 1\right) + u_1 \\
\dot{x}_3 =& x_4 \\
\dot{x}_4 =& -2\frac{x_2}{x_1} x_4 + \cos x_3 \sin x_3 \left(x_6 + \Omega\right)^2 + (1-\mu) \frac{3a}{x_1^5} \sin x_3 \cos x_3 \\
& + \frac{\mu}{x_1} \cos x_3 \cos x_5 \left(\frac{1}{\sqrt{1 + x_1^2 - 2x_1 \sin x_3 \cos x_5}^3} - \Omega^2 \right) + u_2 \\
\dot{x}_5 =& x_6 \\
\dot{x}_6 =& -2 \left(\frac{x_2}{x_1} + x_4 \frac{\cos x_3}{\sin x_3} \right) \left(x_6 + \Omega\right) \\
& - \frac{\mu}{x_1} \frac{\sin x_5}{\sin x_3} \left(\frac{1}{\sqrt{1 + x_1^2 - 2x_1 \sin x_3 \cos x_5}^3} - \Omega^2 \right) + u_3
\end{aligned}
\tag{2.22}
$$

The Hamiltonian function, a value that remains constant for the duration of the transfer, is calculated with the above state-space expression according to (2.4):

$$
\begin{aligned}
H =& R_1 u_1^2 + R_2 u_2^2 + R_3 u_3^2 + \lambda_1 x_2 + \lambda_3 x_4 + \lambda_5 x_6 \\
& + \lambda_2 \left(x_1 x_4^2 - \frac{1-\mu}{x_1^2} - \frac{\mu x_1}{\sqrt{1 + x_1^2 - 2x_1 \sin x_3 \cos x_5}^3} + x_1 \sin^2 x_3 \left(x_6 + \Omega\right)^2 \right. \\
& \quad + \mu \sin x_3 \cos x_5 \left(\frac{1}{\sqrt{1 + x_1^2 - 2x_1 \sin x_3 \cos x_5}^3} - \Omega^2 \right) \\
& \quad \left. + (1-\mu) \frac{3}{2} \frac{a}{x_1^4} \left(3\cos^2 x_3 - 1\right) + u_1 \right) \\
& + \lambda_4 \left(-2\frac{x_2}{x_1} x_4 + \cos x_3 \sin x_3 \left(x_6 + \Omega\right)^2 + (1-\mu) \frac{3a}{x_1^5} \sin x_3 \cos x_3 \right. \\
& \quad \left. + \frac{\mu}{x_1} \cos x_3 \cos x_5 \left(\frac{1}{\sqrt{1 + x_1^2 - 2x_1 \sin x_3 \cos x_5}^3} - \Omega^2 \right) + u_2 \right) \\
& + \lambda_6 \left(-2 \left(\frac{x_2}{x_1} + x_4 \frac{\cos x_3}{\sin x_3} \right) \left(x_6 + \Omega\right) \right. \\
& \quad \left. - \frac{\mu}{x_1} \frac{\sin x_5}{\sin x_3} \left(\frac{1}{\sqrt{1 + x_1^2 - 2x_1 \sin x_3 \cos x_5}^3} - \Omega^2 \right) + u_3 \right)
\end{aligned}
\tag{2.23}
$$

The costate vector is an auxiliary state vector describing the applied optimal

control. It is calculated from (2.5):

$$
\begin{aligned}
\dot{\lambda}_1 =& \frac{2\lambda_2\mu}{{x_1}^3} - \lambda_2 {x_4}^2 - \frac{6a\lambda_2}{{x_1}^5} - \frac{2\lambda_2}{{x_1}^3} + \frac{\lambda_2\mu}{({x_1}^2 - 2\cos x_5 \sin x_3 x_1 + 1)^{\frac{3}{2}}} - \lambda_2\Omega^2 \sin {x_3}^2 \\
& - \lambda_2 {x_6}^2 \sin {x_3}^2 + \frac{18a\lambda_2 \cos {x_3}^3}{{x_1}^5} - \frac{3\lambda_2\mu {x_1}^2}{({x_1}^2 - 2\cos x_5 \sin x_3 x_1 + 1)^{\frac{5}{2}}} \\
& + \frac{15a\lambda_4 \sin(2x_3)}{2{x_1}^6} + \frac{6a\lambda_2\mu}{{x_1}^5} - \frac{2\lambda_6\Omega x_2}{{x_1}^2} - \frac{2\lambda_4 x_2 x_4}{{x_1}^2} - \frac{2\lambda_6 x_2 x_6}{{x_1}^2} - 2\lambda_2\Omega x_6 \sin {x_3}^2 \\
& + \frac{3\lambda_4\mu \cos x_3 \cos x_5}{({x_1}^2 - 2\cos x_5 \sin x_3 x_1 + 1)^{\frac{5}{2}}} - \frac{3\lambda_6\mu \sin x_5}{\sin x_3 ({x_1}^2 - 2\cos x_5 \sin x_3 x_1 + 1)^{\frac{5}{2}}} \\
& - \frac{18a\lambda_2\mu \cos {x_3}^3}{{x_1}^5} - \frac{15a\lambda_4\mu \sin(2x_3)}{2{x_1}^6} - \frac{3\lambda_2\mu \cos {x_5}^2 \sin {x_3}^2}{({x_1}^2 - 2\cos x_5 \sin x_3 x_1 + 1)^{\frac{5}{2}}} \\
& + \frac{3\lambda_6\mu \cos x_5 \sin x_5}{x_1({x_1}^2 - 2\cos x_5 \sin x_3 x_1 + 1)^{\frac{5}{2}}} + \frac{\lambda_6\mu\Omega^2 \sin x_5}{{x_1}^2 \sin x_3} - \frac{\lambda_4\mu\Omega^2 \cos x_3 \cos x_5}{{x_1}^2} \\
& - \frac{\lambda_6\mu \sin x_5}{{x_1}^2 \sin x_3 ({x_1}^2 - 2\cos x_5 \sin x_3 x_1 + 1)^{\frac{3}{2}}} + \frac{6\lambda_2\mu x_1 \cos x_5 \sin x_3}{({x_1}^2 - 2\cos x_5 \sin x_3 x_1 + 1)^{\frac{5}{2}}} \\
& + \frac{\lambda_4\mu \cos x_3 \cos x_5}{{x_1}^2({x_1}^2 - 2\cos x_5 \sin x_3 x_1 + 1)^{\frac{3}{2}}} - \frac{3\lambda_4\mu \cos x_3 \cos {x_5}^2 \sin x_3}{x_1({x_1}^2 - 2\cos x_5 \sin x_3 x_1 + 1)^{\frac{5}{2}}} \\
\dot{\lambda}_2 =& - \frac{-2\lambda_6\Omega + \lambda_1 x_1 - 2\lambda_4 x_4 - 2\lambda_6 x_6}{x_1}
\end{aligned}
\tag{2.24}
$$

$$
\begin{aligned}
\dot{\lambda}_3 =&\lambda_4\Omega^2{\sin x_3}^2 - \lambda_4{x_6}^2{\cos x_3}^2 - \lambda_4\Omega^2{\cos x_3}^2 + \lambda_4{x_6}^2{\sin x_3}^2 - \frac{2\lambda_6 x_4 x_6}{{\sin x_3}^2} \\
&- \frac{3a\lambda_4{\cos x_3}^2}{{x_1}^5} - \frac{27a\lambda_2{\sin x_3}^3}{2{x_1}^4} + \frac{3a\lambda_4{\sin x_3}^2}{{x_1}^5} - \lambda_2\Omega^2 x_1 \sin(2x_3) \\
&- \lambda_2 x_1{x_6}^2 \sin(2x_3) - 2\lambda_4\Omega x_6{\cos x_3}^2 + \frac{27a\lambda_2 \sin x_3}{2{x_1}^4} + 2\lambda_4\Omega x_6{\sin x_3}^2 - \frac{2\lambda_6\Omega x_4}{{\sin x_3}^2} \\
&- \frac{\lambda_2\mu\cos x_3\cos x_5}{({x_1}^2 - 2\cos x_5\sin x_3 x_1 + 1)^{\frac{3}{2}}} - \frac{27a\lambda_2\mu\sin x_3}{2{x_1}^4} - 2\lambda_2\Omega x_1 x_6\sin(2x_3) \\
&+ \frac{3a\lambda_4\mu{\cos x_3}^2}{{x_1}^5} + \frac{27a\lambda_2\mu{\sin x_3}^3}{2{x_1}^4} - \frac{3a\lambda_4\mu{\sin x_3}^2}{{x_1}^5} + \lambda_2\mu\Omega^2\cos x_3\cos x_5 \\
&- \frac{3\lambda_4\mu{\cos x_3}^2{\cos x_5}^2}{({x_1}^2 - 2\cos x_5\sin x_3 x_1 + 1)^{\frac{5}{2}}} + \frac{\lambda_4\mu\cos x_5\sin x_3}{x_1({x_1}^2 - 2\cos x_5\sin x_3 x_1 + 1)^{\frac{3}{2}}} \\
&- \frac{\lambda_4\mu\Omega^2\cos x_5\sin x_3}{x_1} + \frac{3\lambda_2\mu{x_1}^2\cos x_3\cos x_5}{({x_1}^2 - 2\cos x_5\sin x_3 x_1 + 1)^{\frac{5}{2}}} \\
&- \frac{\lambda_6\mu\cos x_3\sin x_5}{x_1{\sin x_3}^2({x_1}^2 - 2\cos x_5\sin x_3 x_1 + 1)^{\frac{3}{2}}} + \frac{3\lambda_6\mu\cos x_3\cos x_5\sin x_5}{\sin x_3({x_1}^2 - 2\cos x_5\sin x_3 x_1 + 1)^{\frac{5}{2}}} \\
&- \frac{\lambda_6\mu\Omega^2\cos x_3\sin x_5}{x_1({\cos x_3}^2 - 1)} - \frac{3\lambda_2\mu x_1\cos x_3{\cos x_5}^2\sin x_3}{({x_1}^2 - 2\cos x_5\sin x_3 x_1 + 1)^{\frac{5}{2}}} \\
\dot{\lambda}_4 =&\frac{2\lambda_4 x_2}{x_1} - \lambda_3 - 2\lambda_2 x_1 x_4 + \frac{2\lambda_6\Omega\cos x_3}{\sin x_3} + \frac{2\lambda_6 x_6\cos x_3}{\sin x_3} \\
\dot{\lambda}_5 =&\Bigg(\lambda_6\frac{\cos x_5}{x_1} + \lambda_6 x_1\cos x_5 - 2\lambda_6{\cos x_5}^2\sin x_3 + \lambda_2{\sin x_3}^2\sin x_5 \\
&- 3\lambda_6\sin x_3{\sin x_5}^2 + \lambda_4\frac{\cos x_3\sin x_3\sin x_5}{x_1} - 2\lambda_2{x_1}^2{\sin x_3}^2\sin x_5 \\
&+ \lambda_4 x_1\cos x_3\sin x_3\sin x_5 + \lambda_2 x_1\cos x_5{\sin x_3}^3\sin x_5 \\
&+\lambda_4\cos x_3\cos x_5{\sin x_3}^2\sin x_5\Bigg)\frac{\mu}{\sin x_3({x_1}^2 - 2\cos x_5\sin x_3 x_1 + 1)^{\frac{5}{2}}} \\
&- \lambda_6\Omega^2\mu\frac{\cos x_5}{x_1\sin x_3} - \lambda_2\Omega^2\mu\sin x_3\sin x_5 - \lambda_4\Omega^2\mu\frac{\cos x_3\sin x_5}{x_1} \\
\dot{\lambda}_6 =&\frac{2\lambda_6 x_2}{x_1} - \lambda_5 - \lambda_4\Omega\sin(2x_3) - \lambda_4 x_6\sin(2x_3) - 2\lambda_2 x_1 x_6{\sin x_3}^2 \\
&+ \frac{2\lambda_6 x_4\cos x_3}{\sin x_3} - 2\lambda_2\Omega x_1{\sin x_3}^2
\end{aligned}
\tag{2.25}
$$

The control input vector specifies the sequence of control input applied to achieve the optimal transfer trajectory. It is computed by solving (2.6), giving the same result as in the Keplerian case.

$$
\begin{bmatrix} u_1 \\ u_2 \\ u_3 \end{bmatrix} = \begin{bmatrix} -\lambda_2\frac{1}{2R_1} \\ -\lambda_4\frac{1}{2R_2} \\ -\lambda_6\frac{1}{2R_3} \end{bmatrix} \tag{2.26}
$$

2.3 Demonstration of optimal orbit transfers

In this section, tools for optimal control derived in 2.2 using the principles described in 2.1 will be applied to demonstrate a various single particle orbit transfers. Unless specified otherwise, the initial state of the controlled particle lies on a circular trajectory (or approximately circular if its orbit is perturbed) around the principal body. The goal state is specified in terms of modified states to correspond to some of the orbits presented in Section 1.4.

First, orbit transfers around the main body are discussed. Then, transfers to various orbits specific to the three-body Hill's system, such as orbits around the second body or one of the Lagrange points, are presented.

All figures of orbits include uncontrolled trajectories of the particle depicting its motion before and after the transfer takes place. This improves the comprehensibility but also serves to confirm the precision of the transfer. The shape of the final orbit is greatly susceptible to deviations of the final state of the transfer from its goal state. If controls are interrupted upon completion of the transfer, the resultant motion should match the desired final orbit if the transfer was performed successfully and precisely.

2.3.1 Transfers around the main body

In this first part, orbits around the principal body are treated. First, the second body is ignored to introduce the optimization method in the simpler Keplerian system derived in Section 2.2.2. Then, orbits transfers are performed in the Hill's system to take into account the perturbations from the second body.

Initial states	x_{01}	x_{02}	x_{03}	x_{04}	x_{05}	x_{06}	J_0
Circular $r = 0.2$	0.2	0	$\pi/2$	0	0	11.1803	-5.0
Circular inclined $r = 0.2$	0.2	0	$3\pi/4$	0	0	15.8114	-5.0

Table 2.1: Table of initial states for transfers between Keplerian orbits

2.3.1.1 Transfer between two circular Keplerain orbits of different radii

The simplest example of orbit transfer is a transfer between two circular orbits of different radii in the same plane. As explained in Section 2.1, the initial state is chosen arbitrarily on the initial orbit (Table 2.1). Just like in Section 1.4.1 of the previous chapter, the xy plane of the coordinate system is chosen to coincide with the orbital plane. As it is done by the example given in Section 2.9, the modified state is chosen such as to disregard the angular state, which should be linearly growing in a circular orbit.

$$\boldsymbol{p} = \begin{bmatrix} x_1 \\ x_2 \\ x_3 \\ x_4 \\ x_6 \end{bmatrix} \tag{2.27}$$

Goal modified state	p_{g1}	p_{g2}	p_{g3}	p_{g4}	p_{g5}	J_g
Circular $r = 0.3$	0.3	0	$\pi/2$	0	6.0858	-3.3333
Circular $r = 0.2$	0.3	0	$\pi/2$	0	11.1803	-5.0

Table 2.2: Table of goal costates for transfers between Keplerian orbits

The second orbit is expressed in terms of modified states given in Table 2.2

Figures 2.1, 2.2 and 2.3 display a transfer between two circular orbits optimized with the method described in Section 2.1. On Figure 2.1, the trajectory in the inertial frame is plotted. Figure 2.3 present the states of the particle throughout the transfer, its modified states (including their target values), and values of costates. Finally Figure 2.3 displays the applied control vector components, the performance index evolution during the transfer and the changes to the Jacobi integral.

The success of a transfer is determined by the satisfaction of the final state function (2.10), which occurs when all modified states converge to their goal value. It can also be verified by assessing whether the final trajectory and Jacobi integral correspond to the desired orbit.

The control input graph informs us of how this transfer was performed. The angular control grows roughly linearly to increase the particle's angular momentum. At the beginning of the manoeuvre, radial thrust is exerting a negative (towards the body) radial force to gain kinetic energy by approaching the body. In the intermediate part of the transfer, the particle's velocity is maximal as it bridges the gap between the two orbits. Finally, at the end of the manoeuvre, negative radial control is applied once more to decelerate the particle and allow it to gain its final circular orbit. It is important to note that the entire transfer between two orbits in the same plane is also performed in that plane.

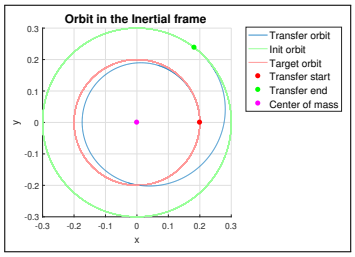

Figure 2.1: Trajectory of a transfer orbit between two Cartesian circular orbits of different radii. $T = 0.7$

In the previous introductory example, the time interval length of the transfer was set to $T = 0.7$. The transfer time can be seen as a parameter of the fixed-time optimization. In some applications, T is set and fixed by the problem to solve. For example, in case of a rendezvous problem, the goal state is time-dependent, hence the transfer has to be performed within a specified time window. In other cases however, the task can be to reach a certain orbit without time specification. In order to find an acceptable trade-off between the time of transfer and fuel consumed, the transfer between to circular orbits in the same plane is performed multiple times with a varying T. The resulting dependence of the performance index on transfer time is captured on Figure 2.4.

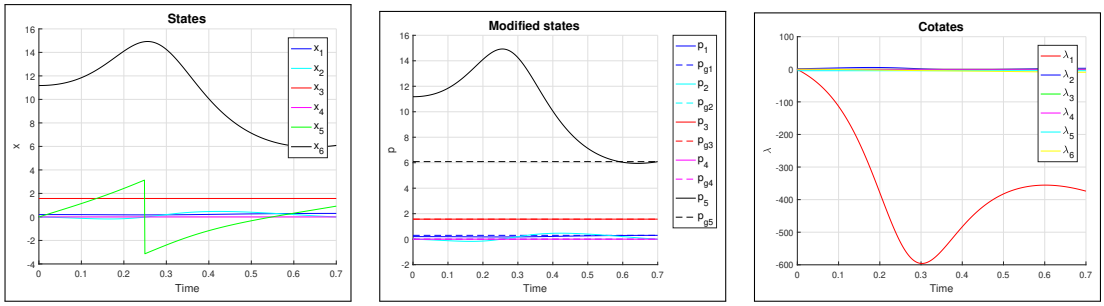

Figure 2.2: States, modified states and costates of a transfer orbit between two Cartesian circular orbits of different radii. $T = 0.7$

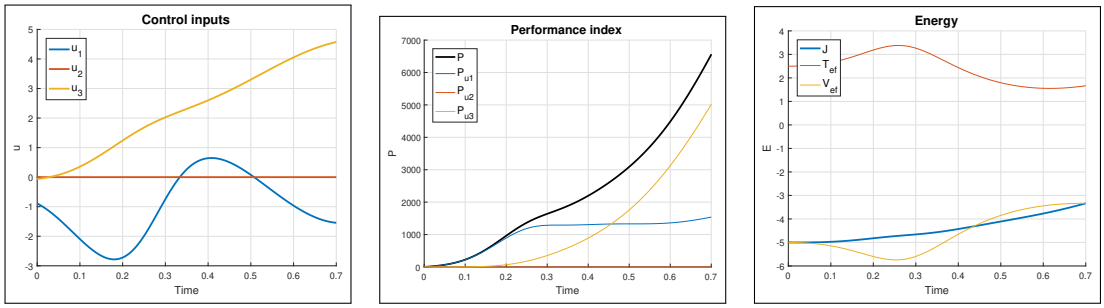

Figure 2.3: Control input, performance index and energy during a transfer orbit between two Cartesian circular orbits of different radii. $T = 0.7$

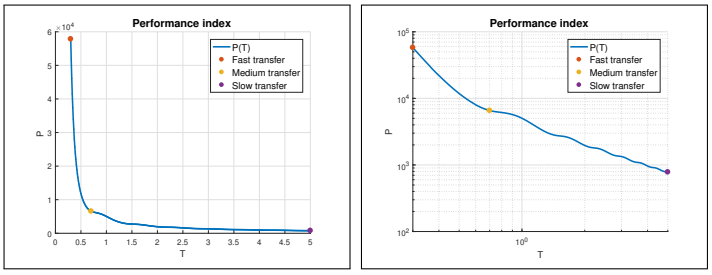

Figure 2.4: Performance index as a function of transfer time T for a transfer between two Keplerian circular orbits of different radii, displayed in both a linear an logarithmic scale

According to Figure 2.4, the performance index assigned to a transfer between two circular Keplerian orbits of different radii decreases roughly exponentially with increasing transfer time. This curve allows us to find a trade-off that satisfies our mission specifications.

Three orbit transfers of varying length for the same transfer task are compared to illustrate options available in the trade-off, a short, long and intermediate one. The intermediate time transfer was chosen with $T = 0.7$ and presented on Figures 2.1, 2.2 and 2.3 above.

Figures 2.5, 2.6 and 2.7 illustrate a short costly transfer between two circular orbits. A large amount of radial control thrust has to be expended in order to first quickly gather enough momentum to approach the target orbit and second to decelerate the particle not to overshoot it. A good indication of the fact this transfer might not be energy efficient is the fact that the Jacobi integral (representing the total energy) overshoots its final value and has to be decreased.

The extra kinetic energy gained during the acceleration phase of the transfer is so great it is not entirely converted into potential, and the particle has to be decelerated to lose some of its total energy.

In orbital mechanics, control is seldom considered cheap as fuel capacities of real satellites are always limited. For this reason, short manoeuvres using a lot of energy are generally not advised.

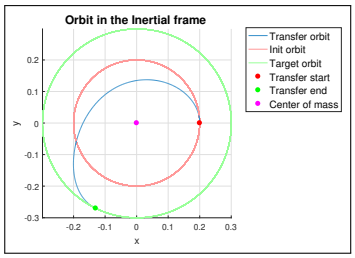

Figure 2.5: Trajectory of a transfer orbit between two Cartesian circular orbits of different radii. $T = 0.3$

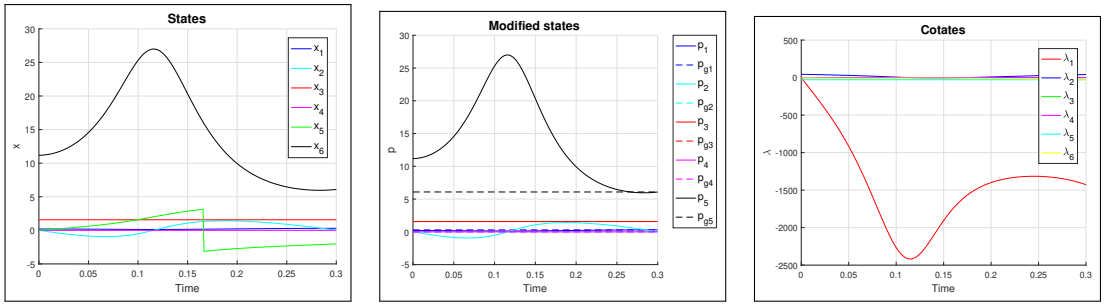

Figure 2.6: States, modified states and costates of a transfer orbit between two Cartesian circular orbits of different radii. $T = 0.3$

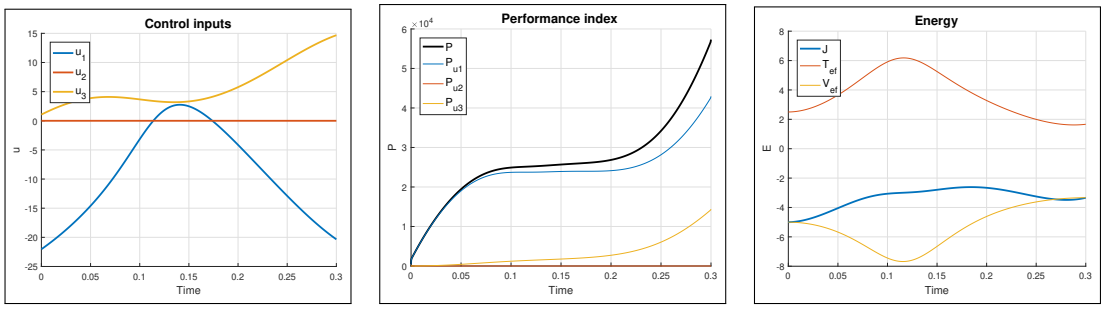

Figure 2.7: Control input, performance index and energy during a transfer orbit between two Cartesian circular orbits of different radii. $T = 0.3$

The other extreme offered by Figure 2.4 is a long transfer performed with only minimal fuel expenditure. If setting $T = 5.0$, the particle spirals away from the initial orbit, gradually increasing its distance to the body until the target orbit is reached (Figure 2.8). The control input graph of Figure 2.10 indicates this movement is conducted by progressively, roughly linearly, increasing the angular thrust. The use of radial control is very limited, as it is applied only in small amplitudes and does almost not contribute to the overall performance index.

Such long and cheap in fuel orbit transfers are in practice more useful than the very short ones. In some cases, thrusters capacities or fuel supplies of satellites is very limited, these kinds of transfers might be the only available. In fact, propulsion technologies such as ion thrusters are intended for these types of transfers as they are suited for short in amplitude but sustained control action.

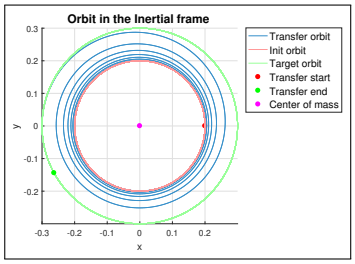

Figure 2.8: Trajectory of a transfer orbit between two Cartesian circular orbits of different radii. $T = 5.0$

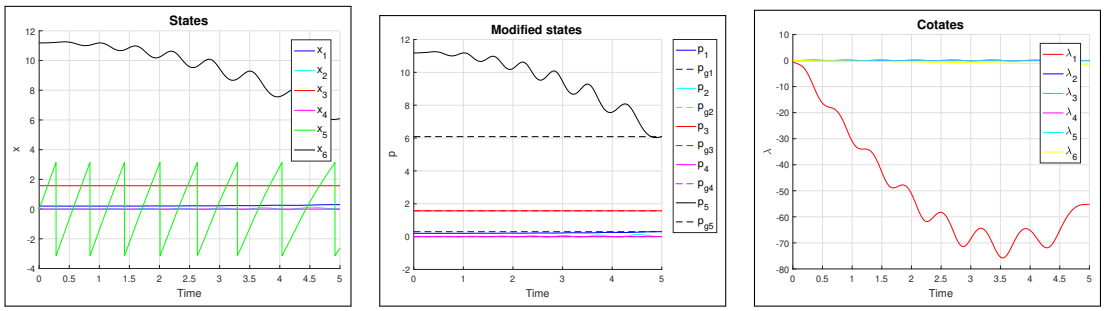

Figure 2.9: States, modified states and costates of a transfer orbit between two Cartesian circular orbits of different radii. $T = 5.0$

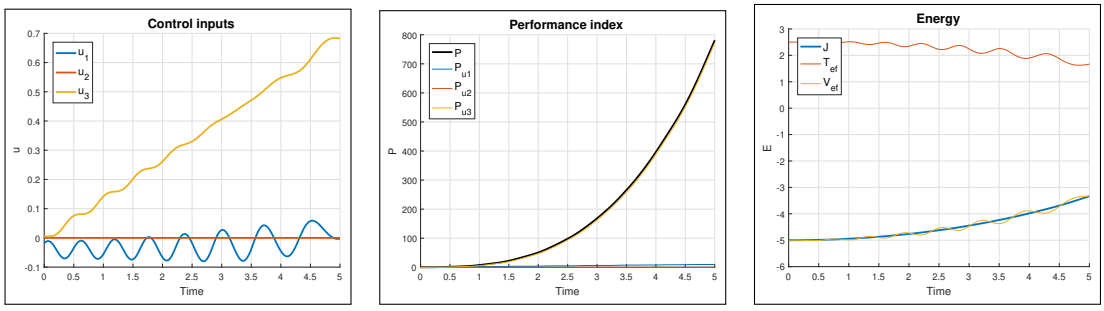

Figure 2.10: Control input, performance index and energy during a transfer orbit between two Cartesian circular orbits of different radii. $T = 5.0$

The orbit transfer problem between two circular orbits of radii r_{c1} and r_{c2} in the same plane has, in fact, a known globally optimal solution in terms of fuel efficiency, called the Hohmann transfer. It is performed with two large instantaneous bursts of thrust, both in the direction of the velocity vector. The first serves to put the controlled particle from the initial circular orbit into an elliptic one with periapsis and apoapsis radii $r_{ep} = r_{c1}$ and $r_{ea} = r_{c2}$ respectively. Once the apoapsis is reached, located on the target circular orbit and opposite to the

initial position, the second burst is fired. This second push redresses the ellipse into the final circular orbit.

We tried to recreate the Hohmann transfer using our method of optimal control. In order to do that, only the angular control input is considered. Disregarding the radial control is done by reassigning weights in the performance index equation (2.2) such as

$$R_1 >> R_3 \tag{2.28}$$

Then, the correct transfer time has to be determined such as to find the transfer that reaches the goal orbit at the point opposite to its initial.

The resulting transfer orbit lasting $T = 0.377$ is presented on Figures 2.11, 2.12 and 2.13. The general elliptic shape of the orbit is maintained and there are similarities between the controls bursts of the Hohmann transfer described above and those plotted on Figure 2.13. Although not in instantaneous impulses, the angular control is applied in the direction of revolution at the beginning and end of the transfer. We assess that the reason why the control is diluted to a longer interval is that the control input is squared in the expression for the performance index (2.2), meaning high amplitude impulses are penalized. In reality, the Hohmann transfer remains a theoretical manoeuvre as instantaneous impulses are not realizable. In addition, even if the instantaneous burst is replaced by a short one with the same energy, restrictions on maximal instantaneous thrust can represent another issue, depending on the used propulsion technology.

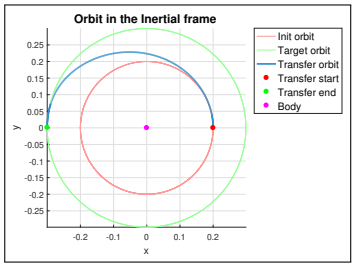

Figure 2.11: Trajectory of a Hohmann-like transfer orbit between two Cartesian circular orbits of different radii. $T = 0.377$

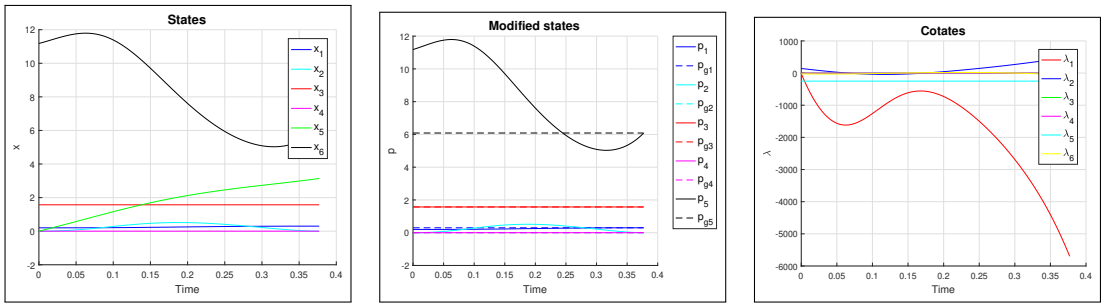

Figure 2.12: States, modified states and costates of a Hohmann-like transfer orbit between two Cartesian circular orbits of different radii. $T = 0.377$

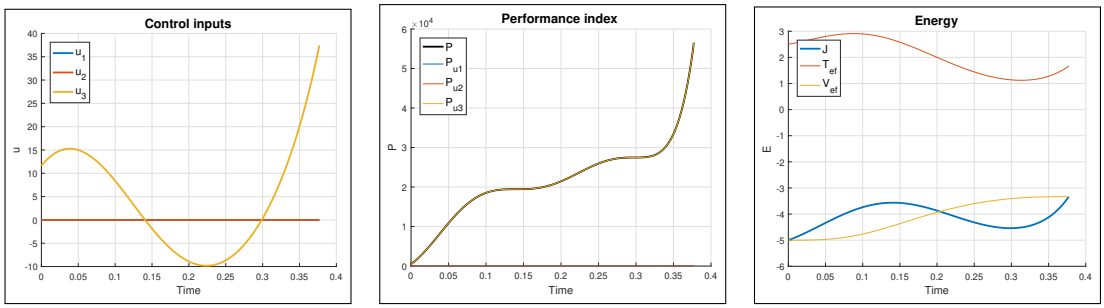

Figure 2.13: Control input, performance index and energy during a Hohmann-like transfer orbit between two Cartesian circular orbits of different radii. $T = 0.377$

2.3.1.2 Transfer between two mutually inclined circular Keplerian orbits

In the examples above, we treated transfers between a pair of circular Keplerian orbit with distinct radii in the same plane. As seen, for the transfer to be optimal, it must itself lie entirely in this plane. We will now present an example of optimal orbit transfer between two orbits of the same radii but with orbital planes inclined by 45° with respect to each other. The initial orbit inclined to the equatorial plane is defined using initial conditions given in Table 2.1. By virtue or all orbital planes in a Keplerian system being equivalent, the target orbit set to be equatorial, using the same modified states as above (2.27) and goal states given by the entry for a circular orbit with $r = 0.2$ in Table 2.2

Figure 2.14 displays the trajectory of such an orbit transfer. The transfer is performed in two phase. In the beginning, the particle stays approximately in the original plane and approaches the body to gain kinetic energy (Figure 2.16), similarly as in previous examples. Once it is carried by its extra energy beyond its initial radius, angular control input in the polar direction is fired to redress the orbit and regain the equatorial plane. Although the total energies of the initial and final orbit are equal, a transfer manoeuvre between them is costly compared to transfers in a plane. For comparison, this transfer between two inclined orbits of radius $r = 0.2$ is about 10 times more expensive in terms of performance index than a manoeuvre between two orbits in the same plane of $r = 0.2$ and $r = 0.3$ respectively, assuming the same transfer time T was considered (Figure 2.4)

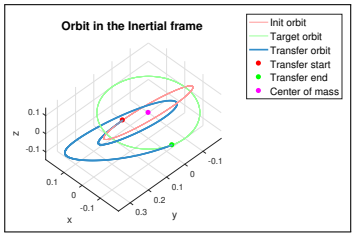

Figure 2.14: Trajectory of a transfer orbit between two Cartesian circular orbits mutually inclined. $T = 1.0$

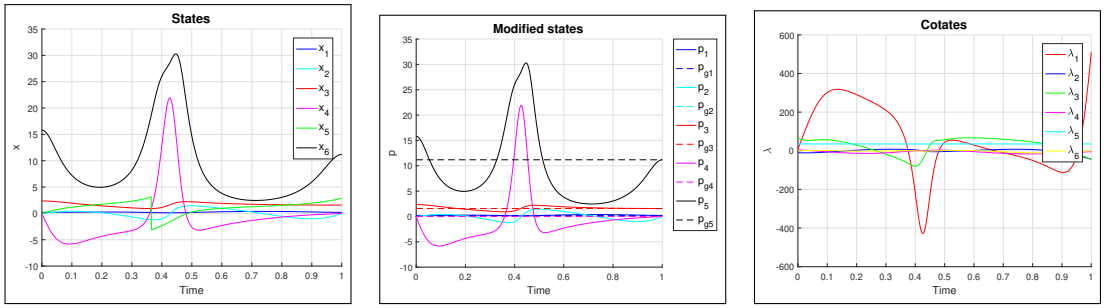

Figure 2.15: States, modified states and costates of a transfer orbit between two Cartesian circular orbits mutually inclined. $T = 1.0$

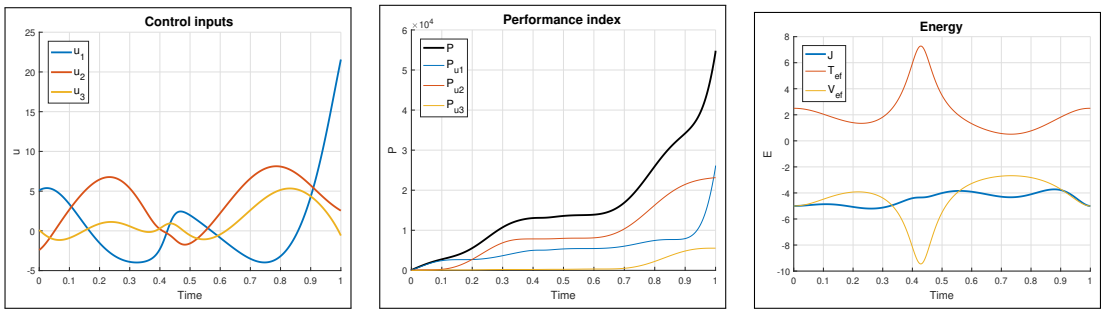

Figure 2.16: Control input, performance index and energy during a transfer orbit between two Cartesian circular orbits mutually inclined. $T = 1.0$

2.3.1.3 Transfer between two circular orbits of different radii in the Hill's system

Basic orbit transfers in the Kepler system were explored in the last section. We will now use the model derived in Section 2.2.3 to compare them to manoeuvres attempting to solve a similar task in the Hill's system, taking into account perturbations from the second body. As in Section 1.4.3, the reduced mass considered is set to $\mu = 0.15$. This value exaggerated with regards to most real-world applications allows for a better visualization of the perturbing effects of the second body.

Initial states	x_{01}	x_{02}	x_{03}	x_{04}	x_{05}	x_{06}	J_0
Circular $r = 0.2$	0.2	0	$\pi/2$	0	0	9.3078	-5.4121
Circular inclined $r = 0.2$	0.2	0	$3\pi/4$	0	0	13.1632	-5.3795

Table 2.3: Table of initial states for transfers between orbits in the Hill's system

Goal modified state	p_{g1}	p_{g2}	p_{g3}	p_{g4}	p_{g5}	J_g
Circular $r = 0.2$	0.3	0	$\pi/2$	0	9.3078	-5.4121
Circular $r = 0.3$	0.3	0	$\pi/2$	0	4.6108	-4.2044

Table 2.4: Table of goal modified states for transfers between orbits in the Hill's system

The first orbit transfer task requires the particle to reach a circular orbit in the principal plane of the Hill's system from another circular orbit in that same

plane. The initial states for a circular orbit of radius $r = 0.2$ are given in Table 2.3. The target orbit of radius $r = 0.3$ is defined using modified states (2.27) listed in Table 2.4. Note that the orbits we refer to as circular are perturbed by the second body and hence their shape is irregular, when treating trajectories close to the principal, larger, body these orbits maintain an approximately circular shape however (as explained in Section 1.4.3).

As in the case of transfers in the Keplerian system, we perform an analysis of the dependency of the performance index on the final time T of the executed transfer. Compared to the almost perfectly exponential curve on Figure 2.4, the relation appears to be more complex in the Hill's system (Figure 2.17). Apart from the exponentially decreasing tendency of the performance index with increasing transfer time, regular deviations from an exponential curve are observable. Indeed, there can be a significant difference in cost between two transfer of similar time. This is due to the second body being in a position where it can either facilitate the manoeuvre by pulling the particle towards the desired higher orbit, or alternatively pulling it in the other direction, forcing it to apply additional control input to counteract it.

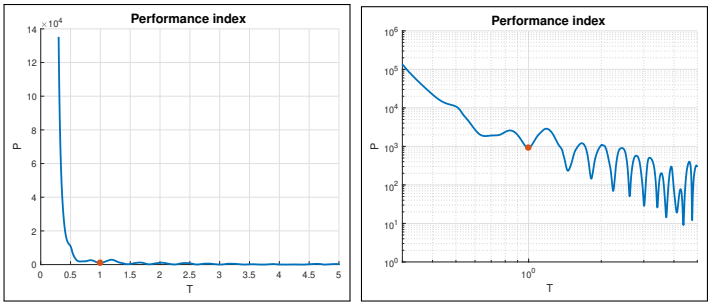

Figure 2.17: Performance index as a function of transfer time T for a transfer between two circular orbits of different radii in the Hill's system, displayed in both a linear an logarithmic scale

The non-monotonic relation of the performance index on transfer time in the Hill's system (Figure 2.17) indicates one has to be careful while setting transfer parameters, as better solutions might be available in the immediate neighbourhood of a chosen time T. Alternatively, the optimization of the transfer over multiple positions on the initial orbit might also improve the solution.

To demonstrate an optimal transfer in the Hill's system between two circular orbits in the principal plane, a transfer time $T = 1.0$ lying in a local minimum on Figure 2.17 is chosen. Its trajectory is depicted in rotating and non-rotating coordinates centred at the principal body as well as in inertial coordinates centred at the barycentre on Figure 2.18. The transfer is performed along similar lines as its counterpart in the Keplerian system. We can best see the favourable influence of the second body on the graph of control inputs on 2.20. When the particle passes between the two bodies ($x_5 = 0$ at around $t = 0.0$ and $t = 0.65$), the radial control is maximal and the otherwise linear increase of angular control is halted to ensure a maximal acceleration away from the principal mass as a result of exposure to the pull of the second body.

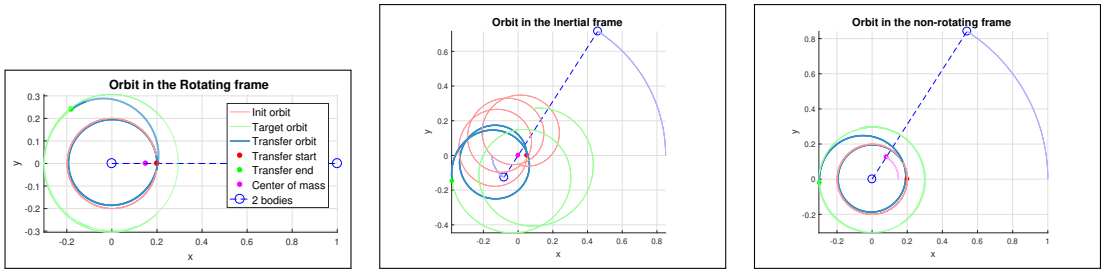

Figure 2.18: Trajectory of a transfer orbit between two circular orbits of different radii in the Hill's system. $T = 1.0$

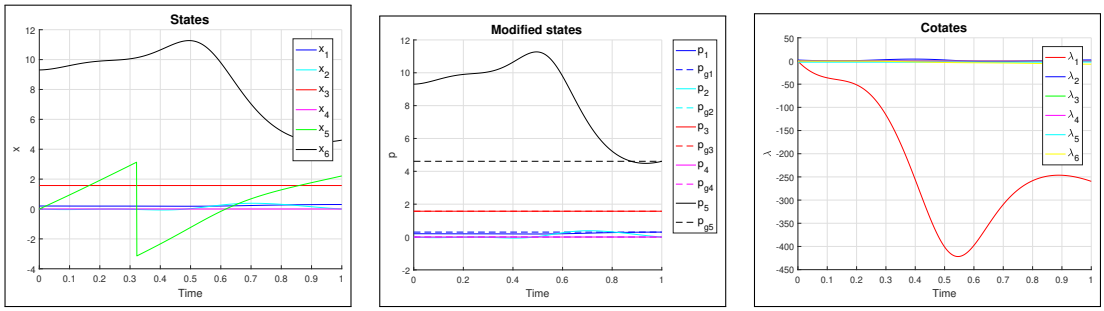

Figure 2.19: States, modified states and costates of a transfer orbit between two circular orbits of different radii in the Hill's system. $T = 1.0$

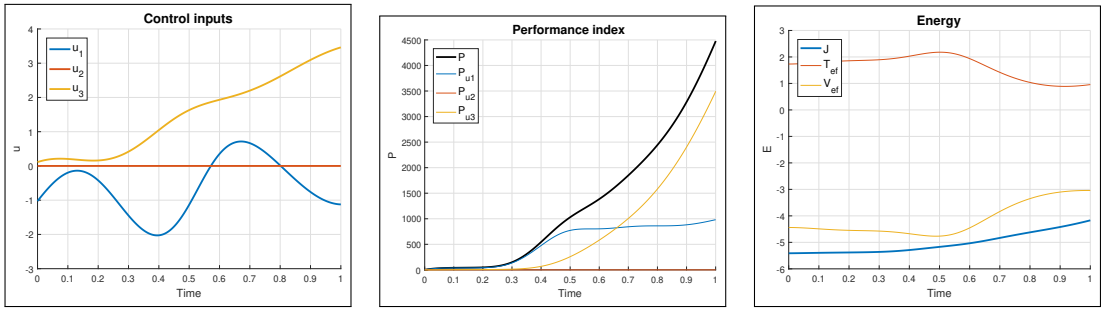

Figure 2.20: Control input, performance index and energy during a transfer orbit between two circular orbits of different radii in the Hill's system. $T = 1.0$

2.3.1.4 Transfer between two mutually inclined circular orbits in the Hill's system

An assignment for an orbit transfer between to circular orbits of the same radius ($r = 0.2$) whose plane are mutually inclined can also be given in the Hill's system. The initial states and goal costates of defining both ends of the transfer are given in Table 2.3 and 2.4 respectively. It is important to note that, in general, inclined orbits in the rotating frame see their orbital plane rotate due to the frame rotation, as explained in Section 1.4.3.2. If a specific line of nodes (the direction of the axis of intersection of the orbital plane with the principal) is desired, it should be specified in the non-rotating frame, as it is fixed there unless the perturbations from the second body are too significant.

Figures 2.21, 2.22 and 2.23 display the specifications of an orbit transfer of final time $T = 1.0$ between two mutually inclined orbits.

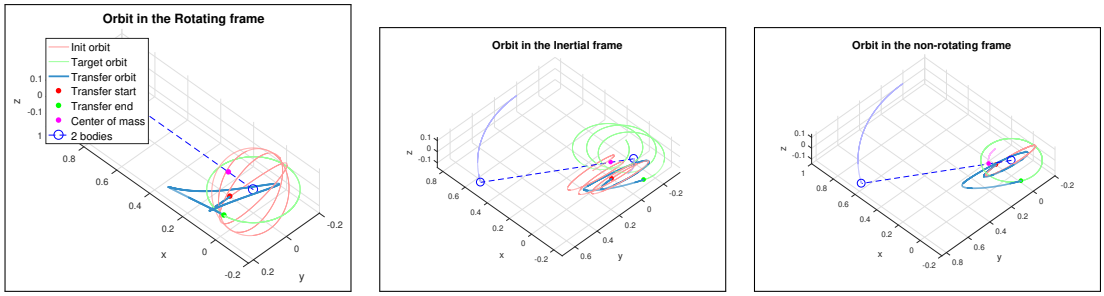

Figure 2.21: Trajectory of a transfer orbit between two circular orbits mutually inclined in the Hill's system. $T = 1.0$

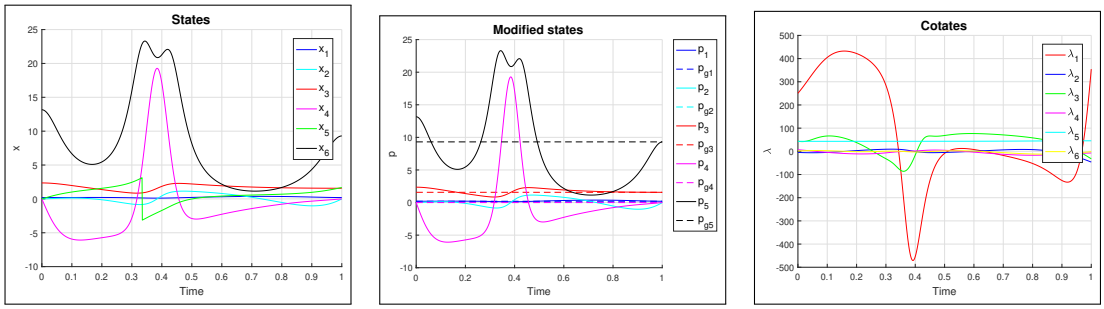

Figure 2.22: States, modified states and costates of a transfer orbit between two circular orbits mutually inclined in the Hill's system. $T = 1.0$

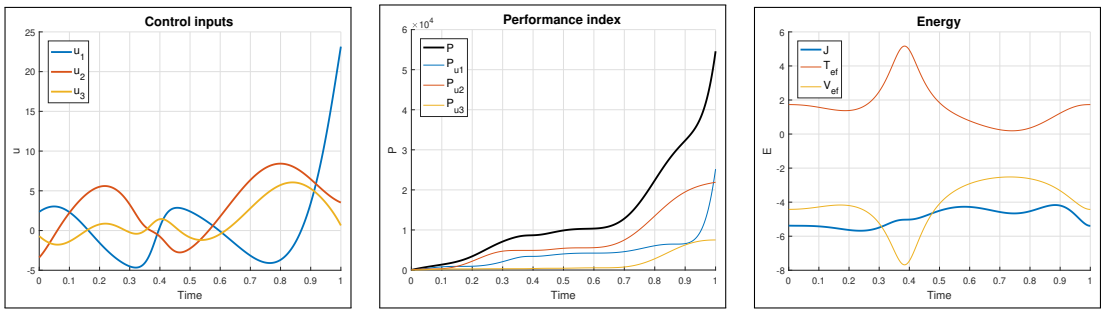

Figure 2.23: Control input, performance index and energy during a transfer orbit between two circular orbits mutually inclined in the Hill's system. $T = 1.0$

2.3.2 Transfers to orbits around the second body

In this section, the transfer between an orbit around the principal body and an orbit of the same radius around the second body is discussed. The primal motivation for orbit transfer from a large body to an orbit around a smaller one are lunar missions, where these transfers are called *lunar orbit insertions*. There are no simply theoretical solutions to transfers to a different body as the Hohmann method is to transfers between orbits around the same body. As mentioned at the beginning of this chapter, it was precisely the solving of this problem by the space agencies during the Space Race that led to the establishment of the optimal control field. Examples of such transfers effectuated by the Apollo mission and a recent Indian lunar mission are depicted on Figure 2.24

In Section 2.3.1, the gravitational pull from the second body has been considered only as a source of perturbation for the transfer orbit, sometimes beneficial, sometimes detrimental as seen on Figure 2.17. The use of the orbit placement

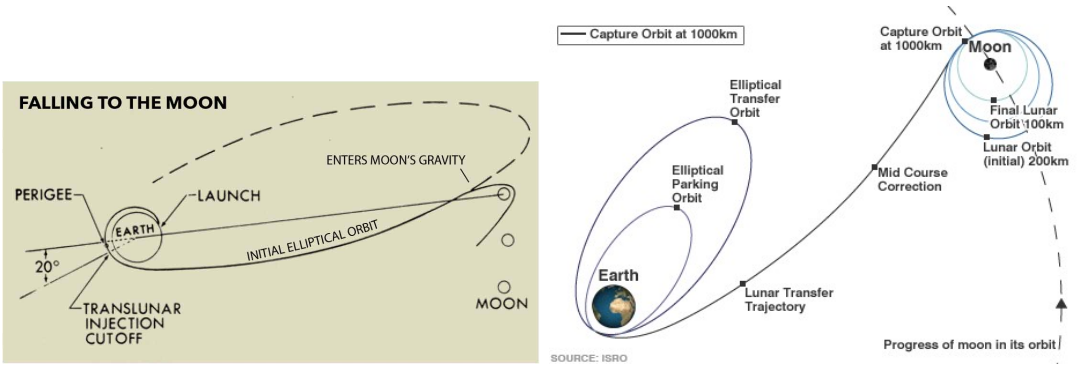

Figure 2.24: Sketches of Lunar orbit insertion manoeuvres performed during real mission. The first figure shows the orbit transfer trajectory used during the Apollo mission (source: `https://www.space.com/26572-how-it-worked-the-apollo-spacecraft-infographic.html`). The graphic on the right depicts the Lunar orbit insertion performed by the Chandrayaan 1 spacecraft during the first successful lunar mission of the Indian Space Research Organisation in 2008 (source: `http://news.bbc.co.uk/2/hi/7679818.stm`)

optimization tools introduced in Section 2.1 is however not limited to transfers between orbits around the principal body.

The initial conditions are chosen similarly as in the previous sections, a circular orbit around the principal mass, given in terms of initial states in Table 2.5. The modified states in this case are chosen as

$$\boldsymbol{p} = \begin{bmatrix} x_1 \\ x_2 \\ x_3 \\ x_4 \\ x_6 \end{bmatrix}_{M2} \tag{2.29}$$

equivalently to (2.27) but is spherical coordinates centred at the second body instead of the first. The target orbit is defined in terms of these modified states is given in Table 2.6.

Initial states	x_{01}	x_{02}	x_{03}	x_{04}	x_{05}	x_{06}	J_0
Circular	0.2	0	$\pi/2$	0	$3\pi/4$	9.3078	−5.4004

Table 2.5: Table of initial states for transfers between orbits in the Hill's system around different bodies

Goal modified state	p_{g1}	p_{g2}	p_{g3}	p_{g4}	p_{g5}	J_g
Circular	0.2	0	$\pi/2$	0	−5.3301	−2.8828
Circular inclined	0.2	0	$\pi/2$	0	−5.3301	−2.8000

Table 2.6: Table of goal modified states for transfers between orbits in the Hill's system around different bodies

An orbit transfer obtain with our optimization method according to the specifications stated above if described on Figures 2.25, 2.26 and 2.27. We can immediately see that the transfer orbit is very similar in shape to the lunar orbit

insertion manoeuvres on Figure 2.24. The particle first increases its altitude with respect to the first body, then uses a swing by to gather kinetic energy and is propulsed to a position in front of the second body. It lets itself get caught up by the body and smoothly enters the desired circular orbit around it.

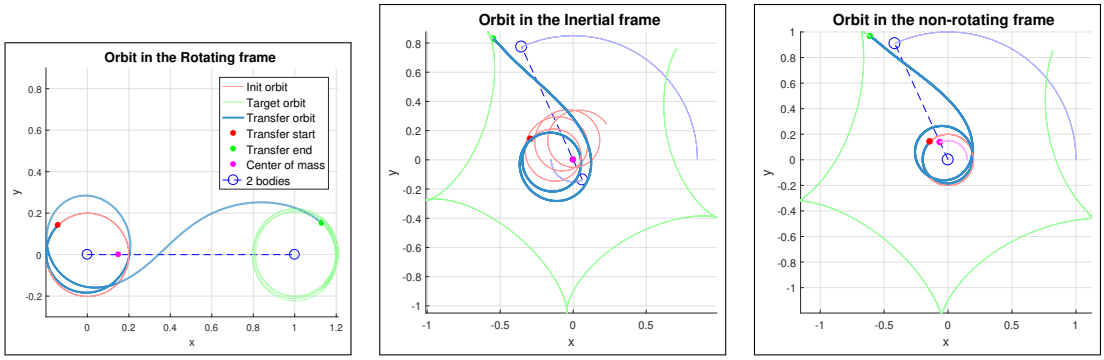

Figure 2.25: Trajectory of a transfer orbit between circular orbits around different bodies in the Hill's system. $T = 2.0$

The Jacobi integral is not monotonic during this transfer (Figure 2.27). This is to be expected as it is a phenomenon that could not be altered by choosing a greater transfer time T as it is done in case of transfers between orbits around the same body in Section 2.3.1.1. The initial and final orbit both lie in distinct valleys of the level set plot 1.5 representing the effective potential in the Hill's system. This signifies the controlled particle has to increase its energy in order to reach the desired region around the second orbit, then decrease it to regain the circular orbit lying inside that potential valley.

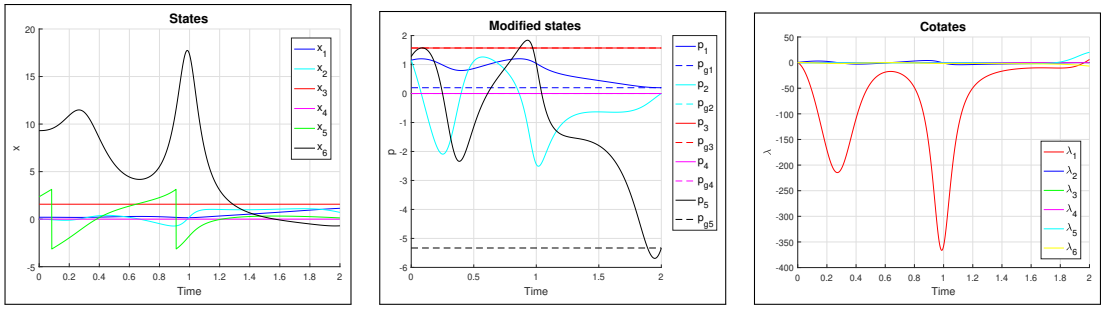

Figure 2.26: States, modified states and costates of a transfer orbit between circular orbits around different bodies in the Hill's system. $T = 2.0$

It has been seen in Section 2.3.1.2 that transfers between two mutually inclined orbits of the same radius around the same body is expensive. If a specific orbit around the second body inclined with regards to the principal plane is targeted, it will be more cost-effective to try to reach this orbit directly from the initial position at the first body. This is the case for example if equatorial lunar orbits are targeted during a lunar orbit insertion task, as the Moon's polar axis is not perpendicular to its revolution plane.

A circular orbit around the second body inclined by 45° with respect to the principal plane is set as the goal of the transfer described by Figure 2.28, 2.29 and 2.30. The modified states are defined in this case are obtained from the original

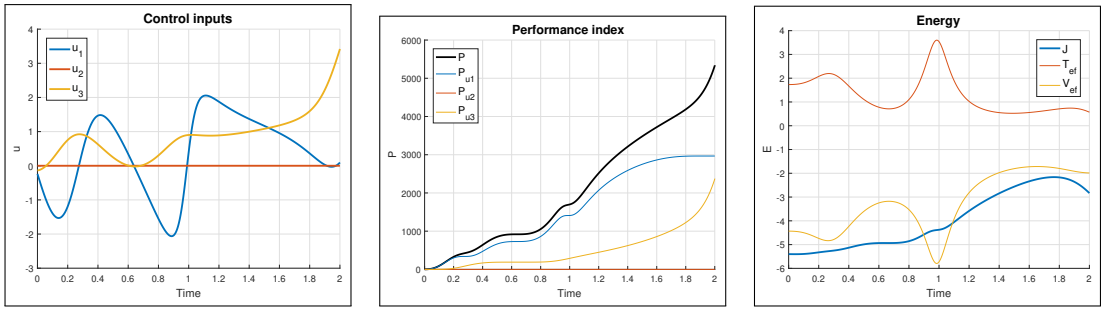

Figure 2.27: Control input, performance index and energy during a transfer orbit between circular orbits around different bodies in the Hill's system. $T = 2.0$

states by not only translating the origin of the coordinate system to the second body but also inclining it by the appropriate angle.

$$\boldsymbol{p} = \begin{bmatrix} x_1 \\ x_2 \\ x_3 \\ x_4 \\ x_6 \end{bmatrix}_{M2, i=45°} \tag{2.30}$$

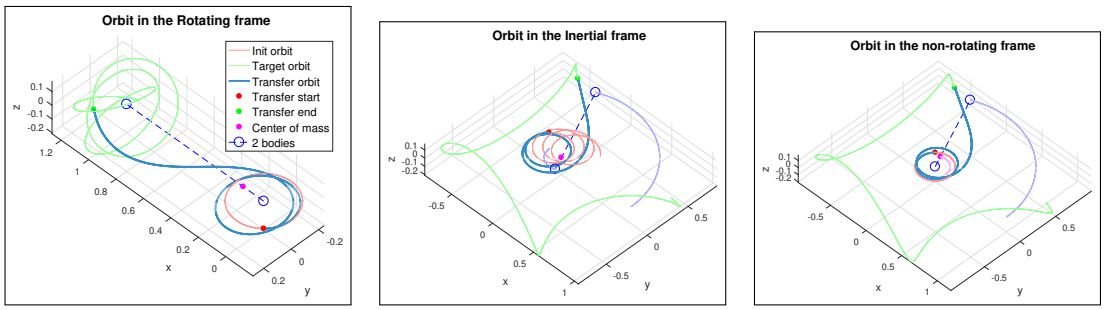

Figure 2.28: Trajectory of a transfer orbit between mutually inclined circular orbits around different bodies in the Hill's system. $T = 2.0$

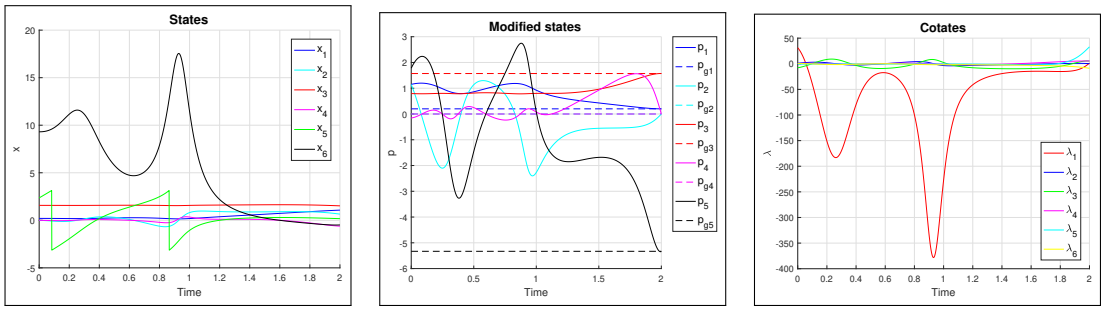

Figure 2.29: States, modified states and costates of a transfer orbit between mutually inclined circular orbits around different bodies in the Hill's system. $T = 2.0$

2.3.3 Transfers to Lagrange points

It was explained in Section 1.3.3.5 that Lagrange points are equilibria in the two-body Hill's system. As such placing a satellite in one of them has many

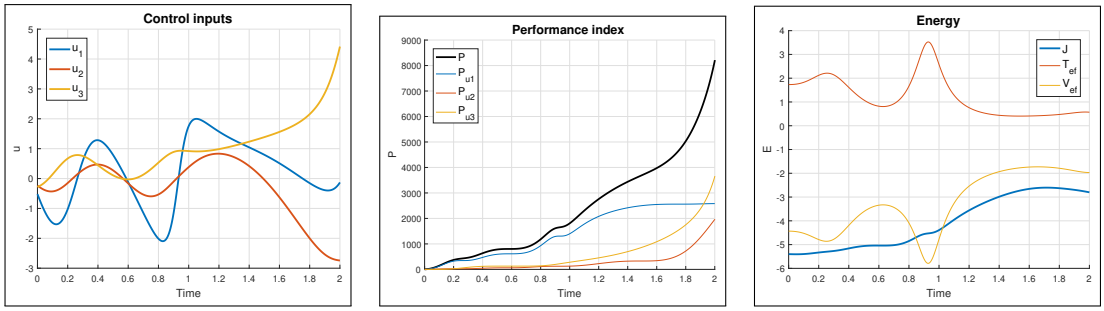

Figure 2.30: Control input, performance index and energy during a transfer orbit between mutually inclined circular orbits around different bodies in the Hill's system. $T = 2.0$

practical applications, as it would place it in a fixed position with regards to the two bodies. This section treats orbit transfers to those Lagrange points from a circular parking orbit around the principal body. As Lagrange points in the rotating coordinates are exact positions, its modified states correspond to the actual states.

$$\boldsymbol{p} = \boldsymbol{x} = \begin{bmatrix} x_1 \\ x_2 \\ x_3 \\ x_4 \\ x_5 \\ x_6 \end{bmatrix} \tag{2.31}$$

As the initial orbit is located at the larger body of the pair, the following transfer will be most relevant to applications in the Earth-Moon system. Transfers to Lagrange points in the Sun-Earth system could similarly be treated just by placing the initial orbit at the smaller body.

2.3.3.1 Transfer to L1

As seen in Section 1.3.3.5, the unstable equilibrium at L1 is located on the segment between the two bodies, closer to the second one. The transfer manoeuvre to it (Figures 2.31, 2.32 and 2.33) is performed along similar lines as the transfer to an orbit around the second body above, with the particle gathering energy around the principal body before being propulsed by a swing by towards L1. As L1 is an unstable equilibrium, a particle only slightly misplaced will eventually drift apart from it. The study of relative stability of Lagrange points is out of the scope of this thesis, but [3] argues L1 is the most unstable of all Lagrange points. This is confirmed in 2.31, as the particle placed by our orbit transfer to L1 stays only about half a period of revolution of the bodies before diverging from it and falling into an elliptic orbit around the second body.

Finding appropriate trajectories for transfers to L1 is relevant in the Earth-Moon system as this equilibrium position could be used as a half-way station for lunar missions.

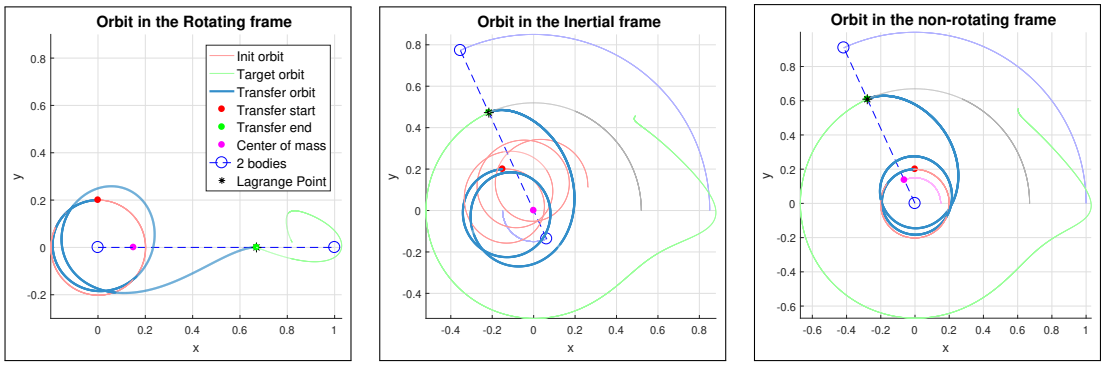

Figure 2.31: Trajectory of a transfer orbit to L1. $T = 2.0$

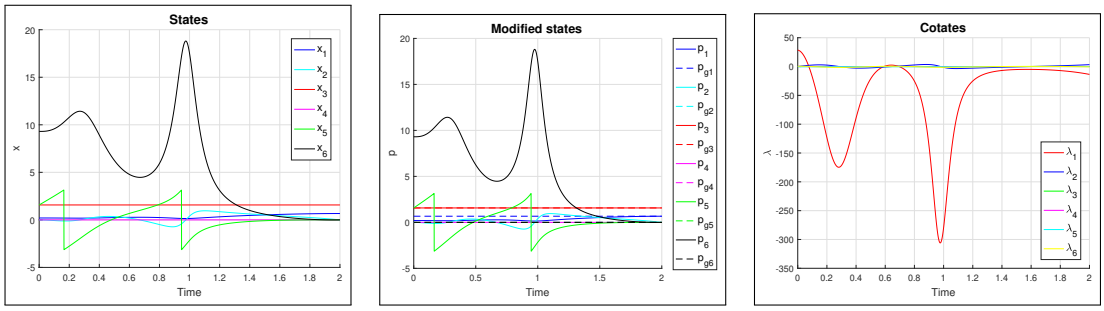

Figure 2.32: States, modified states and costates of a transfer orbit to L1. $T = 2.0$

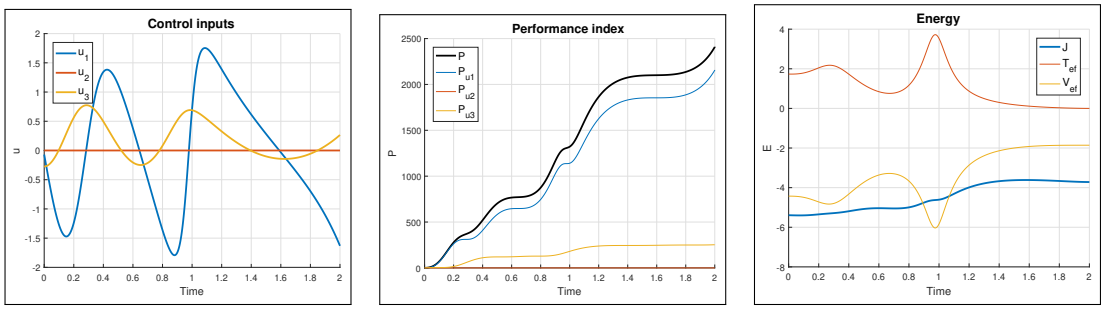

Figure 2.33: Control input, performance index and energy during a transfer orbit to L1. $T = 2.0$

2.3.3.2 Transfer to L2

The Lagrange point L2 lies on the axis of the bodies as well, but this time beyond the second body. The transfer to this location (Figures 2.34, 2.35 and 2.36) uses a close swing by around the second body to give it additional energy in order to reach it.

In the Earth-Moon system, a satellite placed at L2 could be a good observation post or communication relay for the dark side of the moon.

2.3.3.3 Transfer to L3

Like L1 and L2, the Lagrange point L4 lies on the principal axis of the Hill's system. Unlike the previous two however, it is located in the direction opposite to the second body. A transfer orbit to this equilibrium position is displayed on Figures 2.37, 2.38 and 2.39

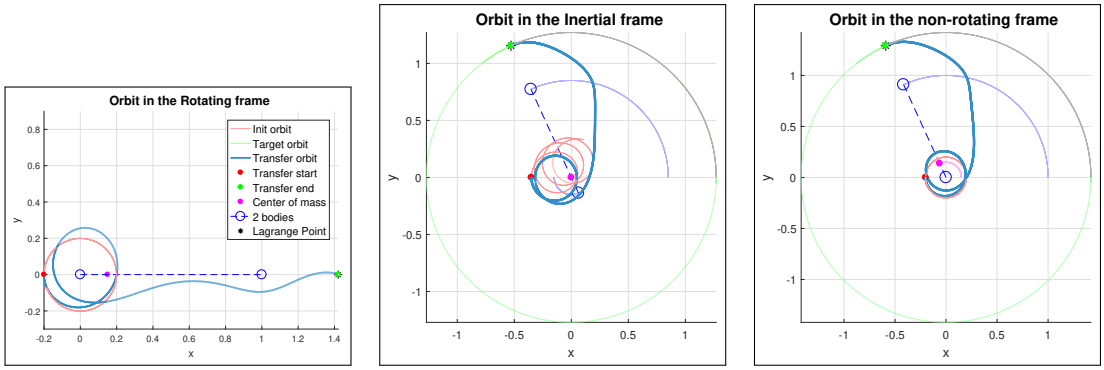

Figure 2.34: Trajectory of a transfer orbit to L2. $T = 2.0$

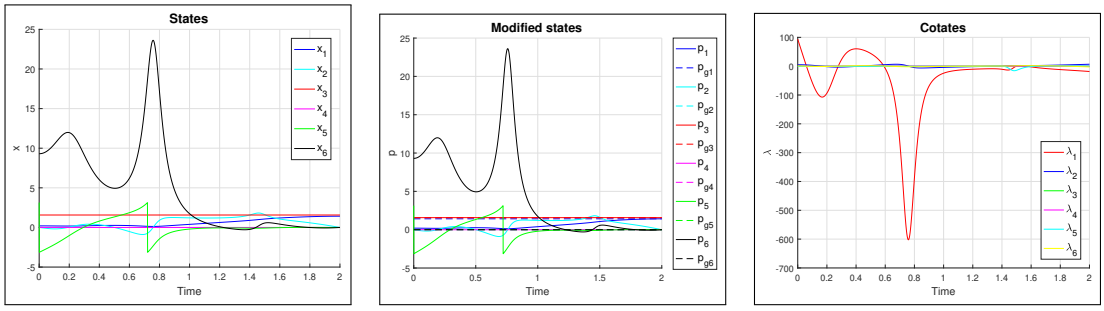

Figure 2.35: States, modified states and costates of a transfer orbit to L2. $T = 2.0$

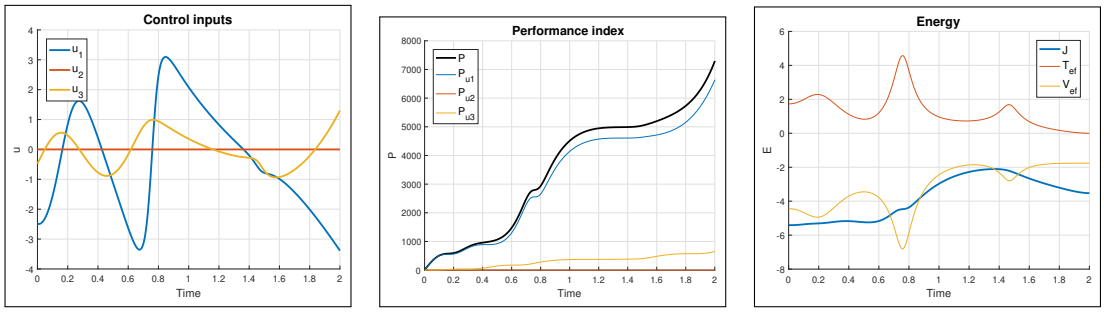

Figure 2.36: Control input, performance index and energy during a transfer orbit to L2. $T = 2.0$

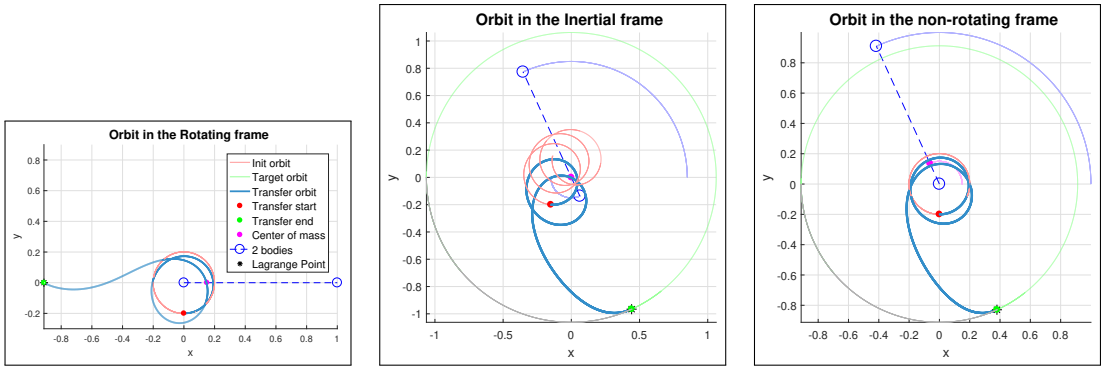

Figure 2.37: Trajectory of a transfer orbit to L3. $T = 2.0$

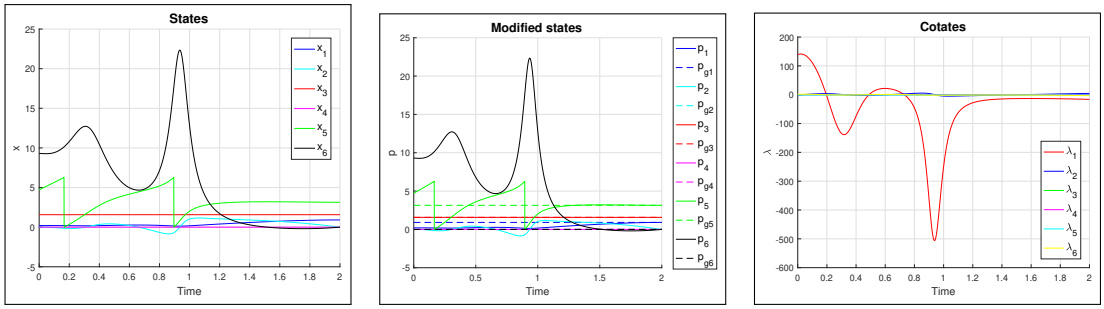

Figure 2.38: States, modified states and costates of a transfer orbit to L3. $T = 2.0$

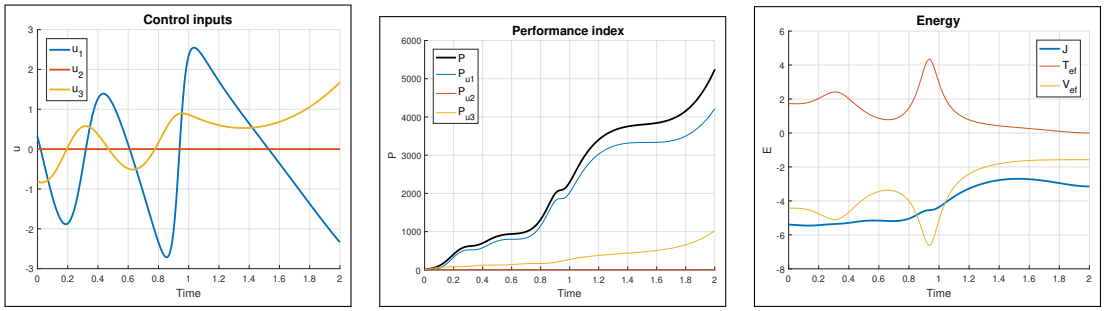

Figure 2.39: Control input, performance index and energy during a transfer orbit to L3. $T = 2.0$

2.3.3.4 Transfer to L4

Lagrange points L4 and L5 are located at the extremities of equilateral triangles formed by themselves and the two bodies. Figures 2.40, 2.41 and 2.42 depicts a transfer to the L4 equilibrium from a circular initial orbit around the main body. A manoeuvre to L5 is not displayed as it is performed along similar lines.

The natural stability of these Lagrange points allows for only minimal station keeping requirement for satellites placed there.

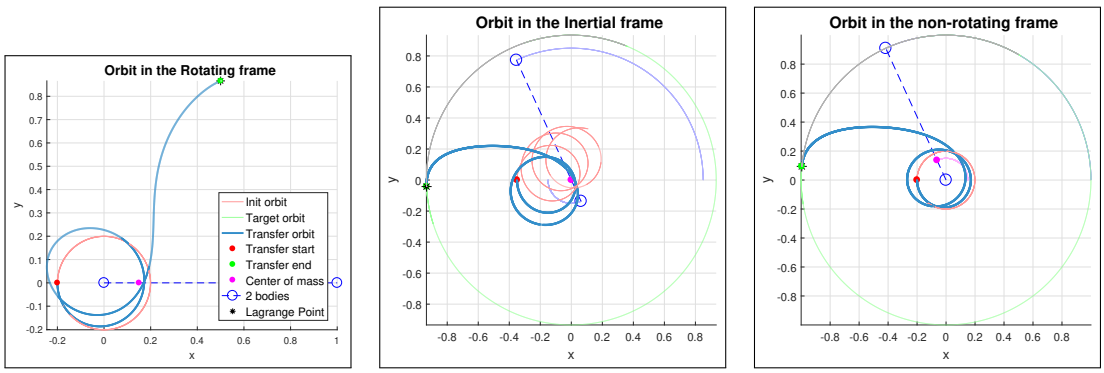

Figure 2.40: Trajectory of a transfer orbit to L4. $T = 2.0$

2.3.4 Transfers to Halo orbits

Halo orbits are defined in Section 1.4.5.2 as orbits that maintain their shape in the rotating frame of the Hill's system. Unfortunately, as their shape is not

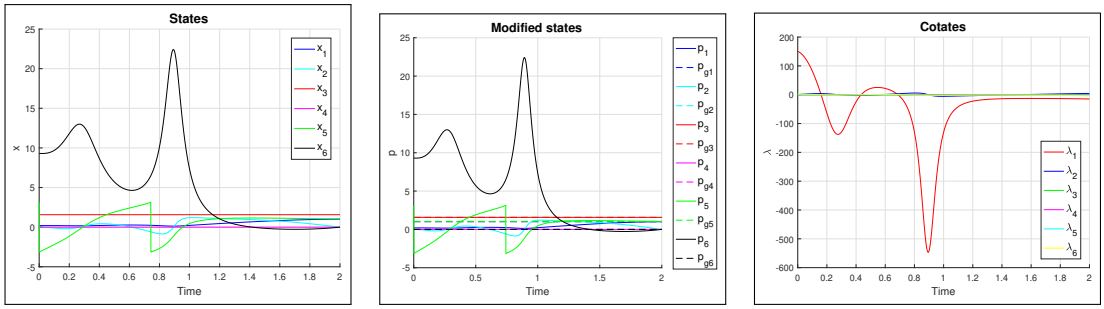

Figure 2.41: States, modified states and costates of a transfer orbit to L4. $T = 2.0$

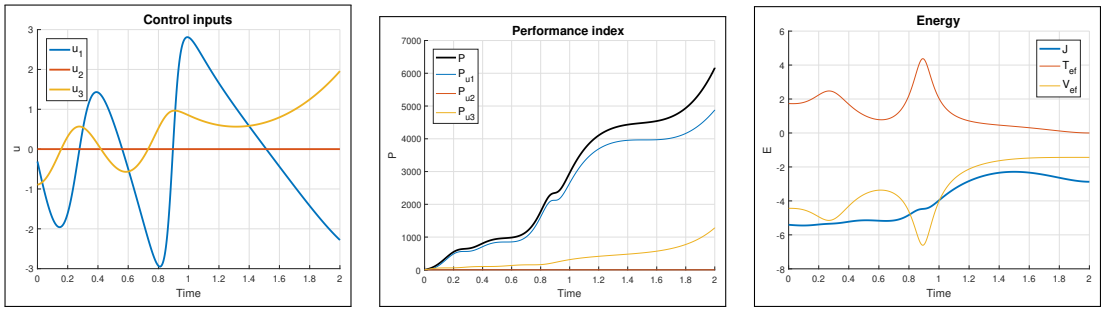

Figure 2.42: Control input, performance index and energy during a transfer orbit to L4. $T = 2.0$

regular, it is difficult to parametrize these orbits in terms of modified states in order to stir the particle to any point laying on them. We therefore use modified state similarly as in the previous section to mirror the actual states.

$$\boldsymbol{p} = \boldsymbol{x} = \begin{bmatrix} x_1 \\ x_2 \\ x_3 \\ x_4 \\ x_5 \\ x_6 \end{bmatrix} \tag{2.32}$$

This allows to express the goal state as a single target point in the rotating frame giving the initial conditions for halo orbits shown in Section 1.4.5.2. This method might lead to suboptimal solutions however, as the particle is allowed to enter the orbit at only a single point.

2.3.4.1 Transfer to a Lyapunov orbit around L3

The first halo orbit chosen as target of an optimal transfer is a Lyapunov orbit at L3. Halo orbits of the Lyapunov type lie in the principal plane of the Hill's system. The transfer orbit is performed similarly as the transfer to L3 (Section 2.3.3.3), which lies nearby. Figures 2.43, 2.44 and 2.45 show the trajectory of this manoeuvre as well as information about the evolution of its states and the control applied.

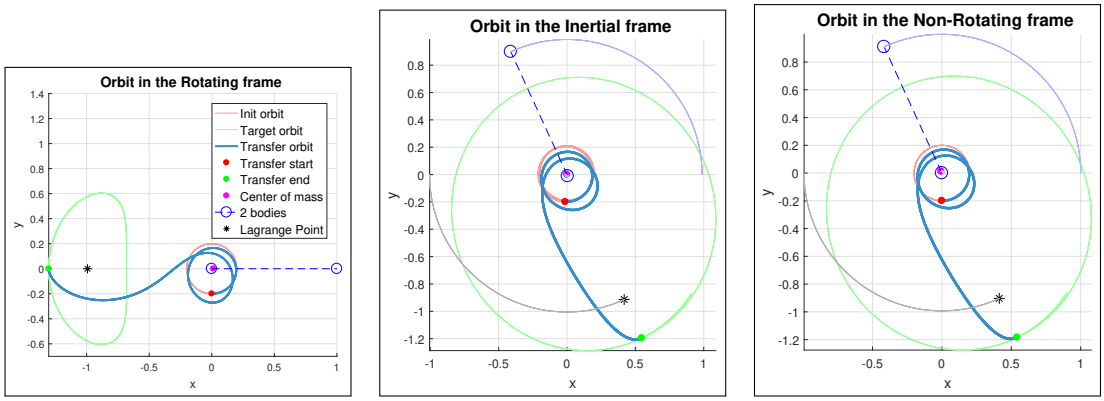

Figure 2.43: Trajectory of a transfer orbit to a L3 Lyapunov orbit. $T = 2.0$

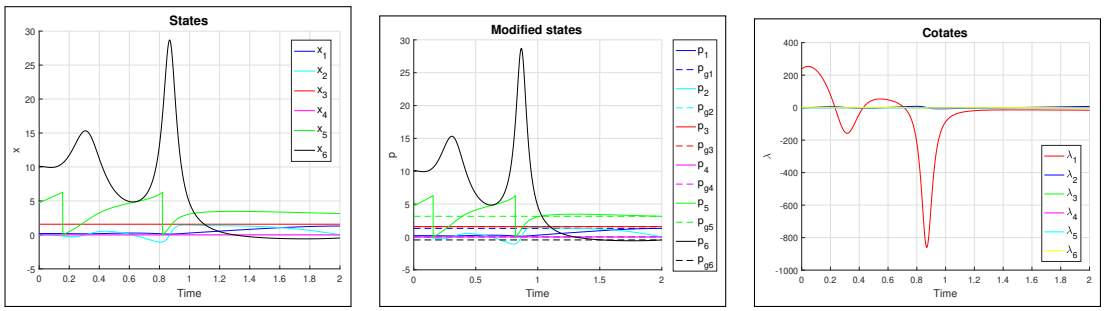

Figure 2.44: States, modified states and costates of a transfer orbit to a L3 Lyapunov orbit. $T = 2.0$

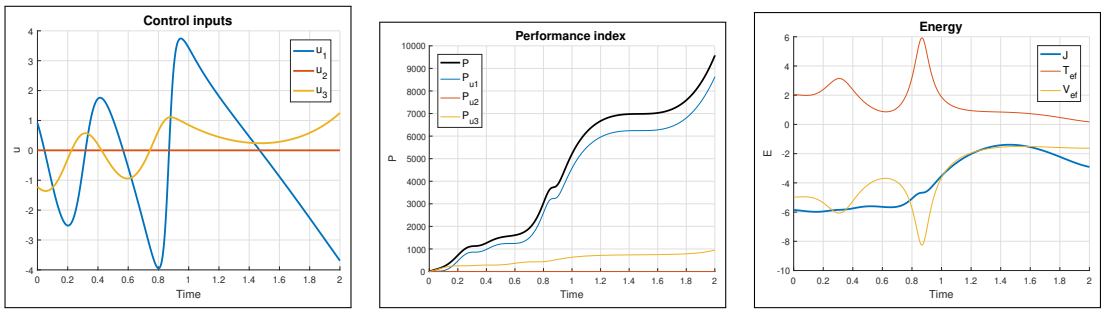

Figure 2.45: Control input, performance index and energy during a transfer orbit to a L3 Lyapunov orbit. $T = 2.0$

2.3.4.2 Transfer to a vertical orbit around L1

The previous section showed a transfer manoeuvre to a halo orbit in the revolution plane of the two bodies. As discussed in Section 1.4.5.2, there are however other classes of orbits that are periodic around a Lagrange point and lie outside the principal plane. On Figures 2.46, 2.47 and 2.48 an example of a transfer to a vertical halo orbit at L1 is presented.

2.3.5 Transfer to a chaotic orbit

As discussed in Section 1.4.4, chaotic orbits are a special class of orbits whose trajectories are highly unpredictable. This makes intercepting a body on a chaotic orbit very challenging, especially with open-loop methods. The chaotic trajec-

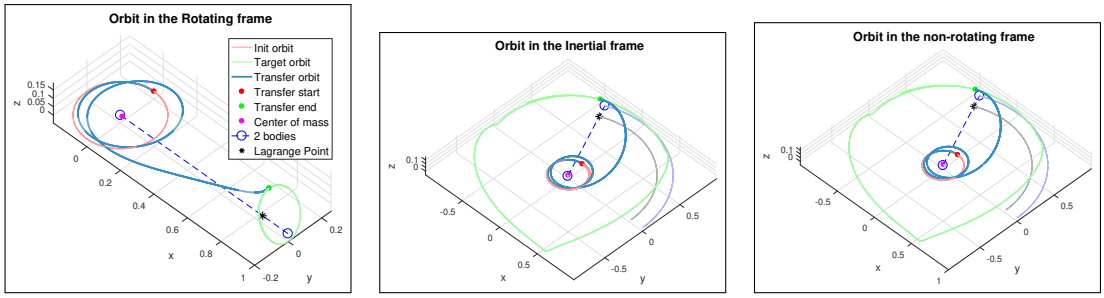

Figure 2.46: Trajectory of a transfer orbit to a L1 vertical halo orbit. $T = 2.0$

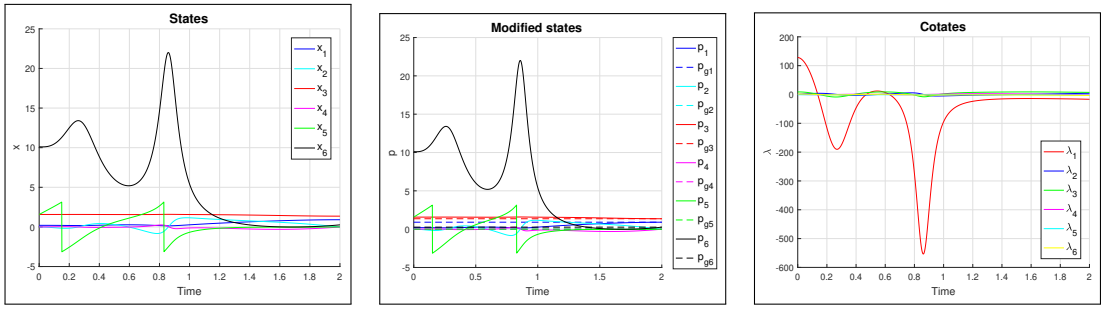

Figure 2.47: States, modified states and costates of a transfer orbit to a L1 vertical halo orbit. $T = 2.0$

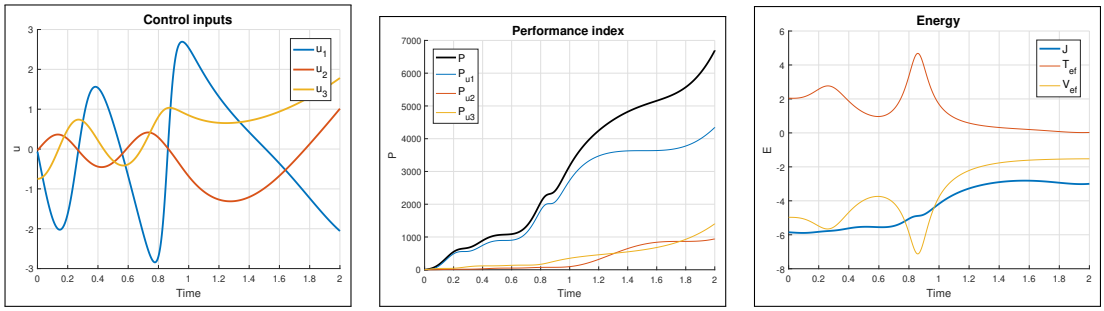

Figure 2.48: Control input, performance index and energy during a transfer orbit to a L1 vertical halo orbit. $T = 2.0$

tory must be known with enough confidence to ensure the final error will stay within a reasonable bound during the transfer time T. For this type of task, just as for the formation reconfiguration manoeuvres in Chapter 3, the optimal controller can serve as a first stage of approach to the desired position. Close-loop methods should take over once the optimal transfer has taken the spacecraft to a location close to the goal. With a feedback controller, modelling or measurement imprecision can be overcome and the satellite can be made to converge on its target.

The chaotic orbit used in this example is the same presented in Section 1.4.4. The initial orbit of the controlled particle is the same circular orbit as the one used it the section 2.3.1 on transfers between circular orbits (Table 2.3). The chaotic orbit is specified in terms of modified states in Table 2.7. The transfer manoeuvre is described by Figures 2.49, 2.50 and 2.51.

Goal modified state	p_{g1}	p_{g2}	p_{g3}	p_{g4}	p_{g5}	J_g
Chaotic	0.8424	0	$\pi/2$	0	0.1187	-3.1788

Table 2.7: Table of goal modified states for a transfer to a chaotic orbit

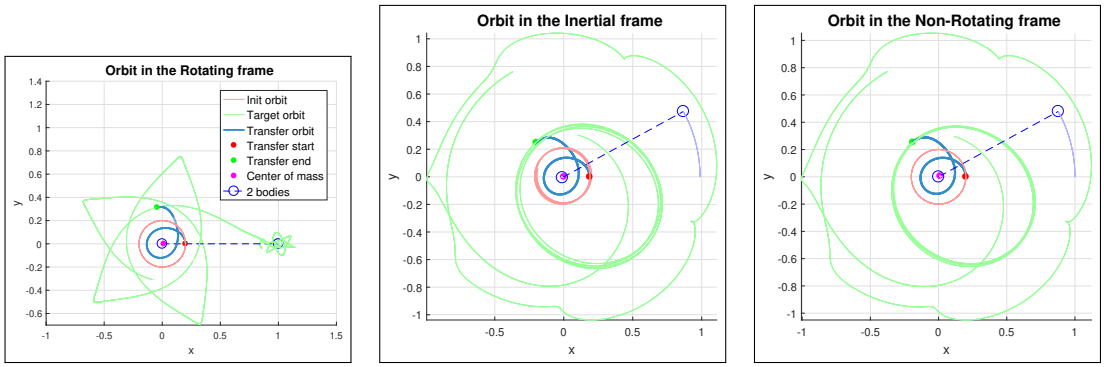

Figure 2.49: Trajectory of a transfer orbit to a chaotic orbit. $T = 0.5$

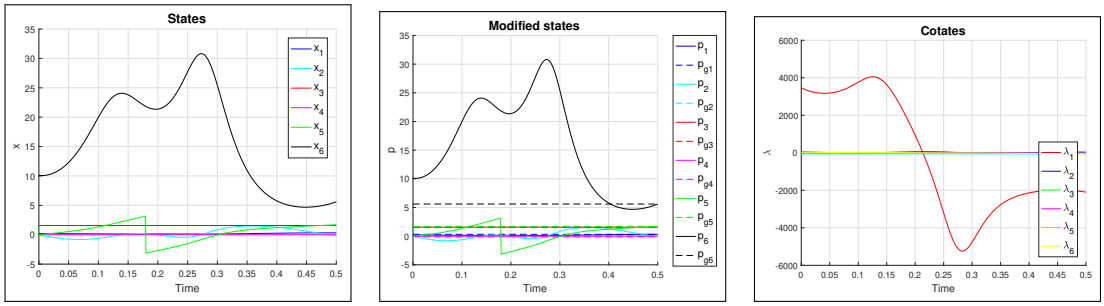

Figure 2.50: States, modified states and costates of a transfer orbit to a chaotic orbit. $T = 0.5$

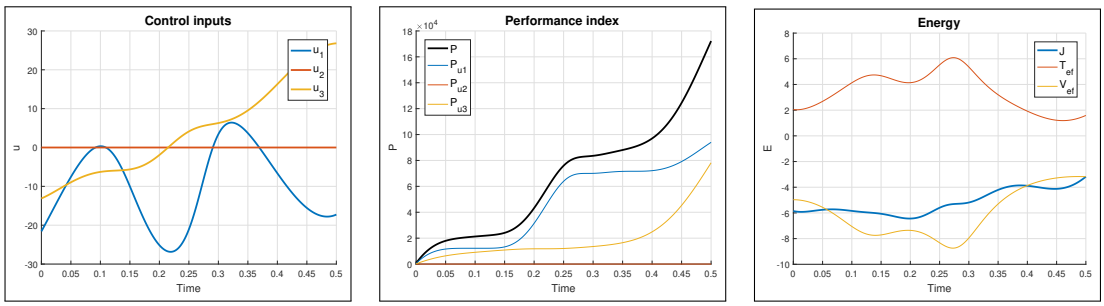

Figure 2.51: Control input, performance index and energy during a transfer orbit to a chaotic orbit. $T = 0.5$

2.4 Conclusion

In the previous chapter, the dynamics of a single particle in a gravitational field were derived. This chapter builds on the obtained model to design an optimal controller allowing for cost-effective transfers between different orbits.

The theory behind this technique as well as a description of the optimization algorithm was described in Section 2.1. This theory was then applied in Section 2.2 to derive the controlled models in a two-body Keplerian and three-body Hill's setup. In Section 2.3, we presented solutions for orbit transfer problems between pairs of orbits described in the last chapter. Our optimal controller proved to be an effective tool for generating efficient transfer trajectories.

In the next chapter, satellite formation flying problems will be introduced. The optimal control approach designed in this chapter will be applied to them and its strengths and weaknesses will be assessed in comparison to a close-loop cooperative controller.

Chapter 3

Formation dynamics and control

Distributed control of multi-agent systems is a rapidly developing field of control engineering, with many applications in both science and industry. Deploying an array of agents solving a task cooperatively has many potential advantages over using only a single agent working independently. Some assignments, such as mapping an unknown terrain or completing a multitude of simple tasks, are performed with greater efficiency when done in parallel, with assignments and results shared among nodes of the network of agents. Moreover, multi-agent systems offer new possibilities, such as complex behaviour emerging from the interactions of simple individuals, and enables to solving problems unmanageable by single-agent systems, such as distributed sensing tasks. Among the primary advantages of distributed systems are their flexibility, robustness to agent failure and reduced complexity of individual agents. These perks come at a price of requiring reliable communication and cooperation between agents.

Communication capacities of spacecraft are severely constrained by a restricted power supply and antenna size while still being required to deliver communication over hundreds to millions of kilometres. Recent developments in this field, along with advancements in other areas, have made communication cheaper and more reliable. This has in turn opened new possibilities in satellite formation flying. A satellite formation is a group of satellites working together to achieve a common goal through cooperation. They are often required to maintain a particular spatial configuration, as one of the main purposes of a multi-satellite system is its ability to simulate a larger installation with a network of agents.

A simple example of satellite formation is a trailing formation, describing multiple satellites on a single orbit successively separated by a, usually small, trailing angle. An example of a system in a trailing formation is the A-train [12], a formation of heterogeneous Earth-observing satellites in Low Earth orbit. As they observe a given area at the same time each from a slightly different position, their observations can be merged into high-definition three-dimensional images of the Earth's atmosphere and surface. A schematic view of the A-train and its member satellites is displayed on Figure 3.1

Another well-known type of satellite formation is the constellation. Satellite constellations are orbiting a body on multiple planes and try to achieve a maximal ground coverage. Global navigation satellite system, such as the Global Positioning System, GLONASS, Galileo or BeiDou-2, all use constellation formations to provide geospatial positioning at all times across the entire globe.

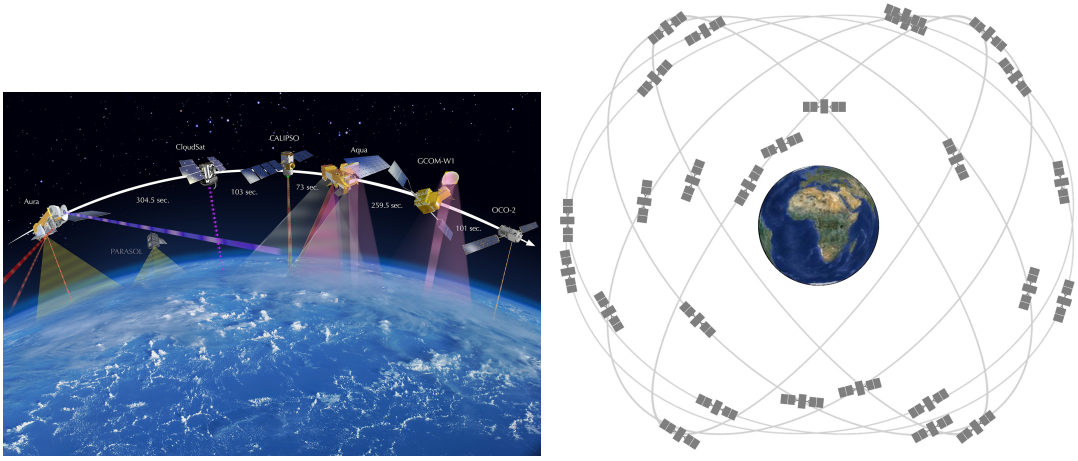

Figure 3.1: On the left: A-train system formation with its member satellites. Figure taken from `https://atrain.nasa.gov/taking.php`. On the right: Constellation formation of the GPS system. Figure taken from `https://www.gps.gov/systems/gps/space/`.

In Chapter 1, the dynamics of a single test particle in the gravitational field of two bodies were derived. The reciprocal gravitational effect of the particle on the bodies was neglected. Likewise, it is a common assumption in satellite formation flying that satellites are considered massless particles that do not exert any gravitational pull on each other. This is a reasonable assumption, as the mass of man-made satellites is much smaller than that of celestial bodies they orbit. This means that all members of a satellite formation are governed by the same set of equations of motion discussed in Chapter 1, independent of each other.

In this chapter, shape-invariant formations are discussed, along with relevant formation reconfiguration and formation keeping tasks. First, the mathematical condition indicating a pair of particles on circular orbits maintains a constant distance is derived. Then, the general methods for optimal control presented in Chapter 2 are applied to formation flying tasks and their potential uses and drawbacks are discussed. Two approaches in applying the optimal controller are described, one fully decentralized treating each particle individually and the other centralized, attempting to optimize the formation jointly as a whole. Finally, an alternative linear feedback controller is designed and compared to the open-loop optimal control strategy.

3.1 Shape invariant formations in circular orbits

In a circular Keplerian orbit, a particle follows a circular trajectory around a massive body with a constant angular velocity, as confirmed by the simulations in Section 1.4.1.1. The following properties hold for circular trajectories:

$$\dot{\boldsymbol{r}} = \boldsymbol{\omega} \times \boldsymbol{r} \qquad \boldsymbol{\omega} \cdot \boldsymbol{r} = 0 \tag{3.1}$$

where $\boldsymbol{r}$ is the position vector of the particle relative to the body and $\boldsymbol{\omega}$ is its angular velocity vector around that body.

If a formation of two particle i and j is to be shape-invariant, meaning the distance between the two is constant, the scalar product of their two position

vectors is also constant in time. This means their spacial angle is constant in time, as the magnitude of both radius vectors is the same, which is necessary for the same period, or angular velocity Ω, of the circular orbit.

$$\boldsymbol{r}_i \cdot \boldsymbol{r}_j = const \tag{3.2}$$

In other words, the derivative of the expression above equals zero.

$$\begin{aligned} \frac{\mathrm{d}}{\mathrm{d}t}\left(\boldsymbol{r}_i \cdot \boldsymbol{r}_j\right) =& \dot{\boldsymbol{r}}_i \cdot \boldsymbol{r}_j + \boldsymbol{r}_i \cdot \dot{\boldsymbol{r}}_j \\ =& \left(\boldsymbol{\omega}_i \times \boldsymbol{r}_i\right) \cdot \boldsymbol{r}_j + \boldsymbol{r}_i \cdot \left(\boldsymbol{\omega}_j \times \boldsymbol{r}_j\right) \\ =& \boldsymbol{\omega}_i \cdot \left(\boldsymbol{r}_i \times \boldsymbol{r}_j\right) + \boldsymbol{\omega}_j \cdot \left(\boldsymbol{r}_j \times \boldsymbol{r}_i\right) \\ =& \left(\boldsymbol{\omega}_i - \boldsymbol{\omega}_j\right) \cdot \left(\boldsymbol{r}_i \times \boldsymbol{r}_j\right) = 0 \end{aligned} \tag{3.3}$$

To assure (3.3) holds at all times, all higher degree derivatives of (3.2) must also equal zero.

$$\begin{aligned} \frac{\mathrm{d}^2}{\mathrm{d}t^2}\left(\boldsymbol{r}_i \cdot \boldsymbol{r}_j\right) =& \left(\boldsymbol{\omega}_i - \boldsymbol{\omega}_j\right) \cdot \frac{\mathrm{d}}{\mathrm{d}t}\left(\boldsymbol{r}_i \times \boldsymbol{r}_j\right) \\ =& \left(\boldsymbol{\omega}_i - \boldsymbol{\omega}_j\right) \cdot \left(\dot{\boldsymbol{r}}_i \times \boldsymbol{r}_j + \boldsymbol{r}_i \times \dot{\boldsymbol{r}}_j\right) \\ =& \left(\boldsymbol{\omega}_i - \boldsymbol{\omega}_j\right) \cdot \left(\boldsymbol{\omega}_i - \boldsymbol{\omega}_j\right) \times \left(\boldsymbol{r}_i \times \boldsymbol{r}_j\right) = 0 \end{aligned} \tag{3.4}$$

If (3.3) is true, the expression above is identically zero, due to the properties of the triple product. The equation (3.4) also indicates all higher derivatives are likewise zero, as the cross product term $\boldsymbol{r}_i \times \boldsymbol{r}_j$ will be repeated with only the constant term $\boldsymbol{\omega}_i - \boldsymbol{\omega}_j$ popping up at each derivative.

3.2 Optimal control

As the dynamics of every particle in the gravitational field are independent of each other, problems of formation control can be also treated by controlling each particle independently to place or maintain it in a position within the formation. As such, techniques of single body orbit placement like the ones derived in Chapter 2 can be applied. If we know the desired formation configuration at a future time T, we can set for each particle as target its goal position and let the entire formation converge. This strategy, however, has a number of downsides.

For example, in formation flying, relative distances are often more important than absolute ones. By controlling each particle individually, absolute distances are used. The problem with this approach is that in the context of celestial mechanics, absolute distances are often orders of magnitude larger than relative ones. Any imprecision in the absolute coordinate will translate to large errors in the relative coordinates. This is especially relevant if the model used is not precise, which is always the case in realistic applications, with the gravitational effects of other bodies, time-varying space weather or satellite system defects are all sources of additional perturbations. As our optimal control method is an open-loop one, it is sensitive to these unexpected effects.

In formation flying, maintaining a formation is a task equally important as forming one. The optimal control method introduced in Chapter 2 allows to ensure the formation has the correct shape at time T, but not before or after. It is unable to continually manage perturbations to the formation with sustained control.

3.2.1 Trailing formation

The equations (3.3) offer a trivial solution where $\boldsymbol{\omega}_i = \boldsymbol{\omega}_j$, meaning the revolution of both particles around the massive body is performed in the same plane with the same angular velocity. If this equality holds at all time, this signifies they share the same circular orbit, trailing one behind the other. This section will treat task of optimal formation reconfiguration and formation keeping for two particles in trailing formation on a circular orbit.

3.2.1.1 Change in trailing angle in the Kepler system

As a simple but practically important example of formation reconfiguration, two particles on the same circular orbit in the equatorial plane of a single body are tasked with changing the angle that separates them. Particle A is considered to be the leader and remains uncontrolled for now. Particle B is the follower and must use optimal control to reduce its trailing angle relative to the leader from an initial $\Delta\varphi_0 = -\pi/2$ to a final $\Delta\varphi_T = -\pi/4$. In order to perform this transfer, the uncontrolled leader's dynamics are simulated for the time of the transfer T, and its final position offset by the desired trailing angle is fed to the follower as goal state.

The orbits of both the leader and the follower during this reconfiguration are shown on Figure 3.2. The orbits are displayed both in inertial coordinates centred at the body and in the pulsating LHLV coordinates introduced in Section 1.1 centred at the leader A. In the leader frame, all distances are rescaled so that the distance from the leader to the body is always 1. Note that as the leader is uncontrolled on a circular orbit, the proportions stay constant in this case.

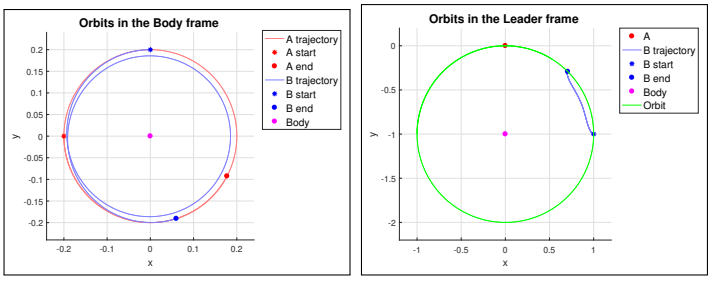

Figure 3.2: Trajectories of an optimal formation reconfiguration manoeuvre changing the trailing angle

Figure 3.3 represent the difference in states between the two particles. For greater clarity, the difference in the radius and radial velocity has been separated from the angular states. Also the states x_3 and x_4 are disregarded here, as it has been shown on multiple occasions in Section 2.3 that an optimal transfer between two Keplerian orbits in the same plane also lies in that plane.

On Figure 3.4 the control input component of both particles is displayed, as well as the plot of the performance index. The performance index is calculated for both particles according to Equation (2.2). Then, a combined performance index $P_{total} = P_A + P_B$ is computed to depict the total cost of the reconfiguration. As in this case only the follower is controlled, the control input vector for the leader is null, as well as its performance index.

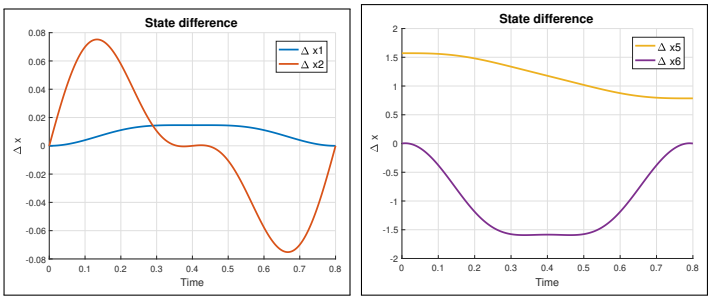

Figure 3.3: Differences in states between the leader and follower particles during an optimal formation reconfiguration manoeuvre changing the trailing angle

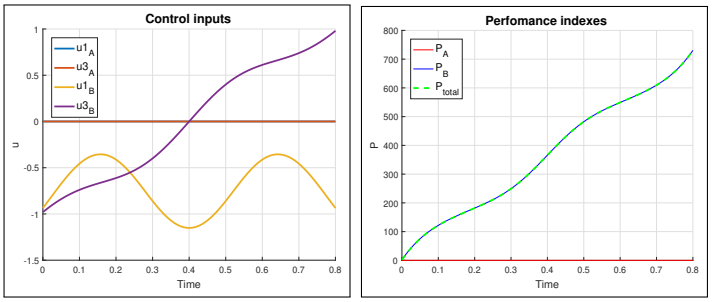

Figure 3.4: Applied control inputs and performance indices during an optimal formation reconfiguration manoeuvre changing the trailing angle

To reconfigure the formation, the follower particle descends to an orbit with a smaller radius, which boosts its angular velocity and allows it to catch up to the leader. This is done, counter-intuitively, by applying a negative angular thrust. By doing so, the particles absolute velocity decreases, allowing it to approach the body. Indeed, close inspection of the orbit in the leader frame (Figure 3.2) as well as the angular difference (Figure 3.3) reveals that the initial motion of the controlled particle is opposite to the direction of its final destination. Likewise, in order to reach the leader's orbit on the appropriate position, positive angular acceleration is applied in order to bring the particle back to the higher orbit and decrease its angular velocity to its initial cruising value.

3.2.1.2 Swap leader and follower position in the Kepler system

A similar manoeuvre as in the previous section can be used to swap the relative position of the leader and the follower on a circular Keplerian orbit. If the leader is still uncontrolled, it remains the task of the follower to perform this reconfiguration. Its goal state is set to lay on the leader's orbit, with an angular offset opposite to its initial value. Such a transfer is described by Figures 3.2, 3.3 and 3.4. The task is similar to the reducing trailing angle transfer above, except the angular difference to bridge is twice as large. The manoeuvre is compared with the previous one in terms of performance index cost per amplitude of the angle difference between the initial and final formation in Table 3.1. We can see that the relative cost of the reconfiguration is twice as higher in this case compared to the trailing angle reduction treated above.

In order to mitigate the increased cost of the swapping reconfiguration manoeuvre described above, a longer time frame can be allocated to the transfer. As

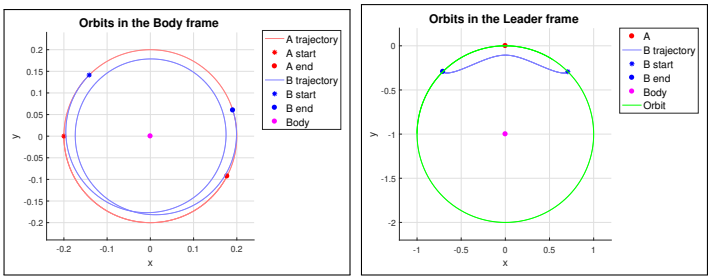

Figure 3.5: Trajectories of an optimal formation reconfiguration manoeuvre swapping the leader and the follower

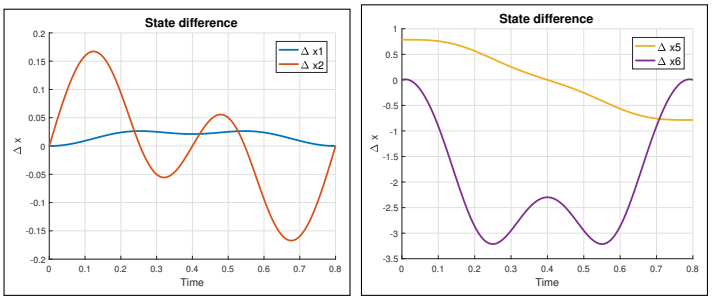

Figure 3.6: Differences in states between the leader and follower particles during an optimal formation reconfiguration manoeuvre swapping the leader and the follower

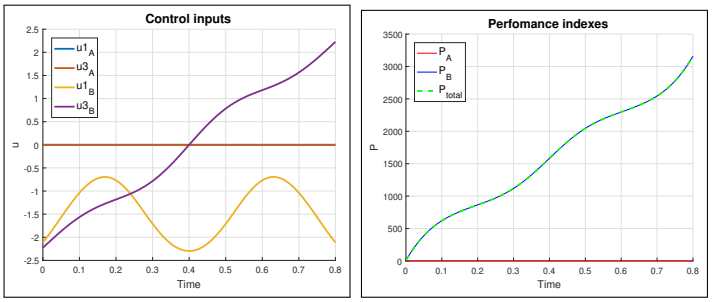

Figure 3.7: Applied control inputs and performance indices during optimal formation reconfiguration manoeuvre swapping the leader and the follower

Reconfiguration task	Angle	Cost	Cost per Angle
B reduces trailing angle	$\pi/4$	730	929
Swap performed by B	$\pi/2$	3160	2012
Swap in coordination by A and B	$\pi/2$	1247	794

Table 3.1: Cost comparison for different optimal reconfiguration manoeuvres

seen in Section 2.3.1.1 Figure 2.4, there is an approximately exponential relation between the transfer time T and the performance index P.

Another solution might be controlling both particles in a more coordinated reconfiguration manoeuvre. In order to do that, we slightly modified the optimal control method from Chapter 2 to be able to control both particles at the same time. The modified state vectors of the leader and follower particles are defined

as

$$\boldsymbol{p_A} = \begin{bmatrix} x_{A1} \\ x_{A2} \\ x_{A3} \\ x_{A4} \\ x_{A5} - x_{B5} \\ x_{A6} \end{bmatrix} \qquad \boldsymbol{p_B} = \begin{bmatrix} x_{B1} \\ x_{B2} \\ x_{B3} \\ x_{B4} \\ x_{B5} - x_{A5} \\ x_{B6} \end{bmatrix} \tag{3.5}$$

The angular modified state is set in relative rather than absolute terms. This system becomes centralize, as both particles are controlled together and not independently as before. With the leader particle being controlled, we displayed the reconfiguration orbits in an additional, virtual leader centred frame in Figure 3.8. This frame is an LVLH frame following a virtual particle on an orbit corresponding to the leader's if it had remained uncontrolled. It allows visualizing the motion of both particles in a rotating frame.

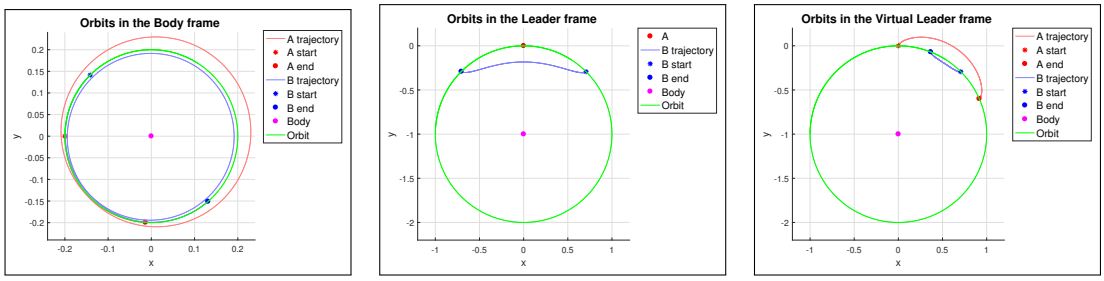

Figure 3.8: Trajectories of a jointly optimal formation reconfiguration manoeuvre swapping the leader and the follower

In the coordinated manoeuvre found according to the joined optimal control technique described above, the overall amplitude of the control assigned to the leader particle A is much greater than for the follower B (Figure 3.10). We suspect this is due to the fact that decreasing a leading angle is cheaper than reducing the trailing angle, because of the smaller force required for performing a desired motion in higher orbits compared to orbits closer to the body. The reduction of a leading angle involve a manoeuvre mirroring the one used to increase it. The particle is first angularly accelerated to gain energy and a higher radius, where its angular velocity is lower. When the follower particle passes under it (on a trajectory similar to the one in both of the previous examples), angular thrust in the opposite direction is applied to decrease it and realign it to the original orbit.

By controlling both particles using their relative angular difference, the overall cost of the swapping manoeuvre is much smaller than by only letting the follower be controlled (Table 3.1).

The leader and follower satellites can be heterogeneous, with different masses and propulsion systems, this can be taken into account by assigning appropriate weights to the controls of both particles, usually to model a higher manoeuvrability of the follower compared to the leader. This allows to prioritize the control of one particle over the other.

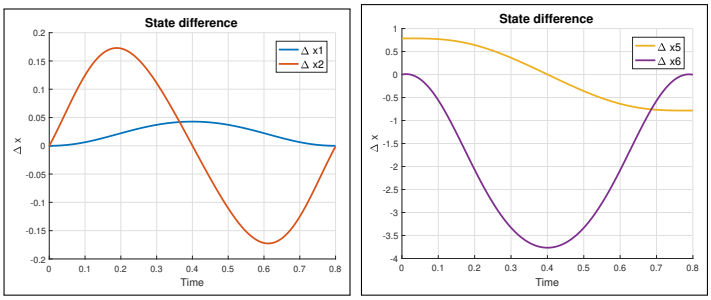

Figure 3.9: Differences in states between the leader and follower particles during a jointly optimal formation reconfiguration manoeuvre swapping the leader and the follower

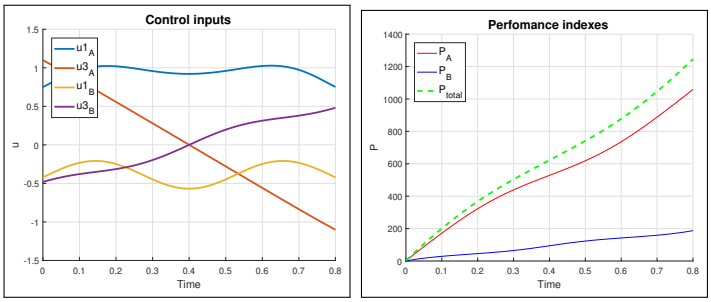

Figure 3.10: Applied control inputs and performance indices during a jointly optimal formation reconfiguration manoeuvre swapping the leader and the follower

3.2.1.3 Compensate for perturbations in the Hill's system

The optimal control tool presented in Chapter 2 is an open-loop method that allows to steer the system into a desired state at a fixed final time T. As mentioned earlier, this method is not well suited for coping with unexpected perturbations and imprecisions of the model. On the other hand, if the perturbations are known and precisely modelled, it can take them into account in its control scheme, potentially even taking advantage of them.

If a formation flying on a circular orbit is subjected to perturbations from a second massive body or the oblateness of the first one it soon becomes deformed or breaks apart completely. This is depicted on Figure 3.11, where the formation is shown to grow apart over time due to these perturbations. Large values of both the oblateness parameter $a = 0.002$ and the reduced mass $\mu = 0.15$ are used in order for the deformation to be noticeable within a short time span.

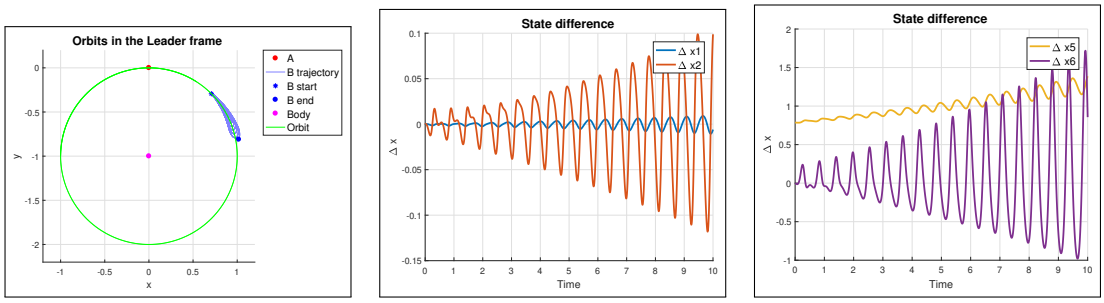

Figure 3.11: Drift caused by perturbations to the Keplerian model

If the formation is to maintain its shape and size continuously, feedback solu-

tions reacting to immediate deviations from the desired configuration are better suited. In some applications however, satellites might only be required to come together into formation at discrete moments, for example to carry out a measurement that is possible or sufficient to be performed only once in a time interval. In this case, the joined optimal control method presented in the previous example can be used to ensure the formation is reassembled at the required time, before letting it drift freely. On Figures 3.12, 3.13 and 3.14, both particles are allowed to be perturbed from their initial formation, but are continuously controlled in order to ensure the formation is reassembled at time T.

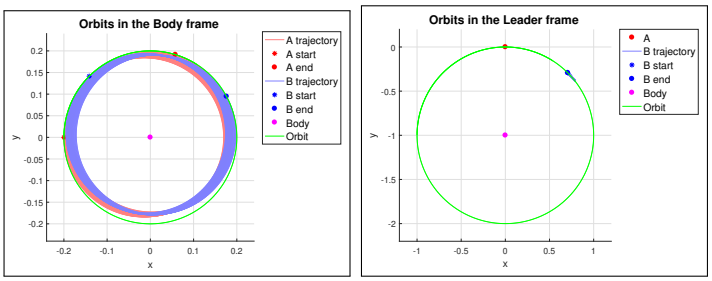

Figure 3.12: Trajectories of an optimal formation maintenance manoeuvre

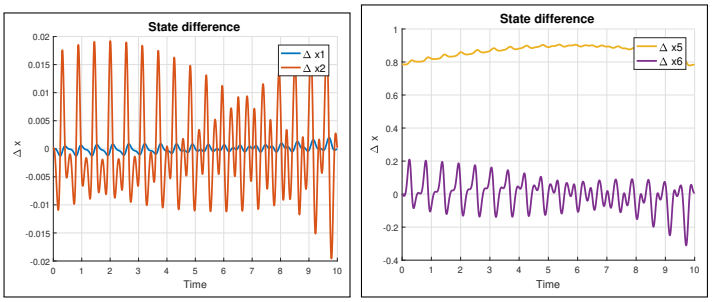

Figure 3.13: Differences in states between the leader and follower particles during an optimal formation maintenance manoeuvre

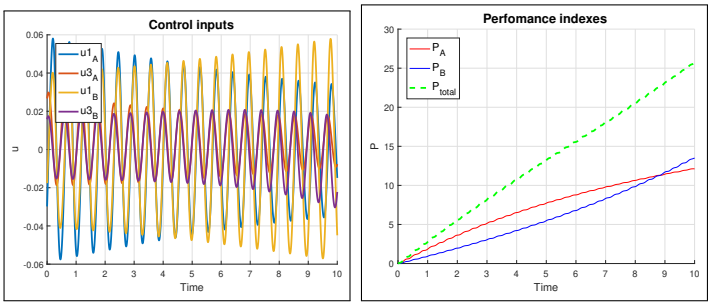

Figure 3.14: Applied control inputs and performance indices during an optimal formation maintenance manoeuvre

3.2.2 LISA formation

There exist solutions to Equation (3.3) where $\boldsymbol{\omega}_i \neq \boldsymbol{\omega}_j$, indicating formations where particles maintain a constant mutual distance without sharing the same

orbit. Maintaining constant distances between more than two particles orbiting a body on different planes allows a formation to maintain a certain geometric shape. An example of such a formation is the planned Laser Interferometer Space Antenna (or LISA) mission of the European Space Agency. The LISA formation is composed of three satellites in mutually inclined quasi-circular heliocentric orbits. The satellites form an equilateral triangle whose shape is time-invariant with arm lengths measured in millions of kilometres. The goal of the mission is to create an interferometer sensor to measure gravitational waves from distant black holes. As the wavelength of gravitational waves is very large, an appropriately large measuring instrument is required for their measurement, or, as in this case, a formation of satellites mimicking a single instrument. An artistic rendering of the LISA formation orbiting the Sun is displayed on 3.15.

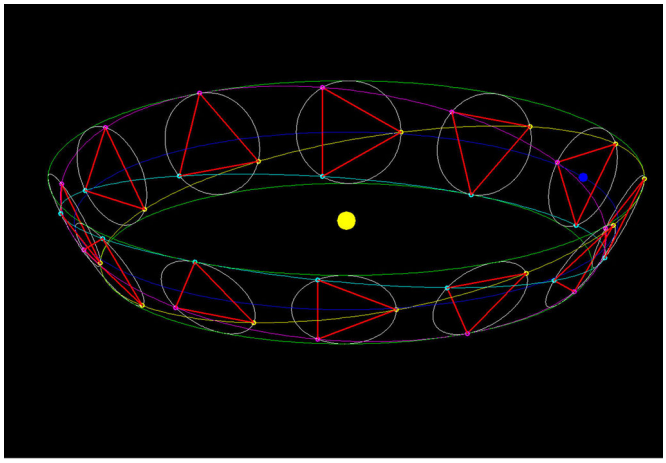

Figure 3.15: Schematic of the LISA formation orbiting around the Sun. Figure taken from `https://hepl.stanford.edu/news_stories/uv-led/index.html`

To faithfully recreate formation reconfiguration of the LISA multi-satellite system, initial conditions for the formation are taken from [13], where multiple configuration specifications are given in terms of initial states of each satellite. The initial states of satellites A, B and C corresponding to triangular configurations of arm length $1Gm$ and $6Gm$ is given in Table 3.2. These initial conditions are converted into the position and velocity vectors in Cartesian coordinates and inserted into Equation 3.3 to check if each pair of particles of the formation is shape-invariant. We consider the results listed in Table 3.3 sufficiently close to zero to conclude a formation of particles placed on orbits defined by their initial states from Table 3.2 will remain in a formation in the shape of an equilateral triangle.

The trajectory of particles A, B and C forming the triangular LISA formation with arm length $6Gm$ during one of its revolution in the inertial body-centred frame is shown on Figure 3.16.

For a better visualization of the relative motion of the three particles, Figure 3.17 displays their motion in a frame centred at the immediate centre of the formation. In this frame, the particles move on recurved 8-shape trajectories while maintaining a triangular configuration.

Illustrative reconfiguration manoeuvres for the LISA formation will now be discussed. First, the transfer from a trailing formation on a circular orbit into a

	x_{01}	x_{02}	x_{03}	x_{04}	x_{05}	x_{06}
A_1	0.9978	0.0005	1.4316	0.3802	2.8145	0.9353
B_1	0.9989	0.0036	1.4323	0.3751	2.8211	0.9348
C_1	0.9956	0.0030	1.4371	0.3782	2.8178	0.9401
A_6	0.9996	−0.0090	1.4211	0.3916	2.7980	0.9279
B_6	1.0063	0.0098	1.4251	0.3620	2.8376	0.9254
C_6	0.9866	0.0063	1.4541	0.3800	2.8180	0.9576

Table 3.2: Initial conditions for LISA formations of arm lengths $1AU$ and $6AU$[13]

A_1B_1	$(\boldsymbol{\omega}_{A_1} - \boldsymbol{\omega}_{B_1}) \cdot (\boldsymbol{r}_{A_1} \times \boldsymbol{r}_{B_1})$	$-1.0274 \cdot 10^{-5}$
B_1C_1	$(\boldsymbol{\omega}_{B_1} - \boldsymbol{\omega}_{C_1}) \cdot (\boldsymbol{r}_{B_1} \times \boldsymbol{r}_{C_1})$	$-6.0426 \cdot 10^{-6}$
C_1A_1	$(\boldsymbol{\omega}_{C_1} - \boldsymbol{\omega}_{A_1}) \cdot (\boldsymbol{r}_{C_1} \times \boldsymbol{r}_{A_1})$	$1.6367 \cdot 10^{-5}$
A_6B_6	$(\boldsymbol{\omega}_{A_6} - \boldsymbol{\omega}_{B_6}) \cdot (\boldsymbol{r}_{A_6} \times \boldsymbol{r}_{B_6})$	$-3.7007 \cdot 10^{-4}$
B_6C_6	$(\boldsymbol{\omega}_{B_6} - \boldsymbol{\omega}_{C_6}) \cdot (\boldsymbol{r}_{B_6} \times \boldsymbol{r}_{C_6})$	$-2.0656 \cdot 10^{-4}$
C_6A_6	$(\boldsymbol{\omega}_{C_6} - \boldsymbol{\omega}_{A_6}) \cdot (\boldsymbol{r}_{C_6} \times \boldsymbol{r}_{A_6})$	$5.8585 \cdot 10^{-4}$

Table 3.3: Check for the shape-invariance condition (3.3) for the values from Table 3.2

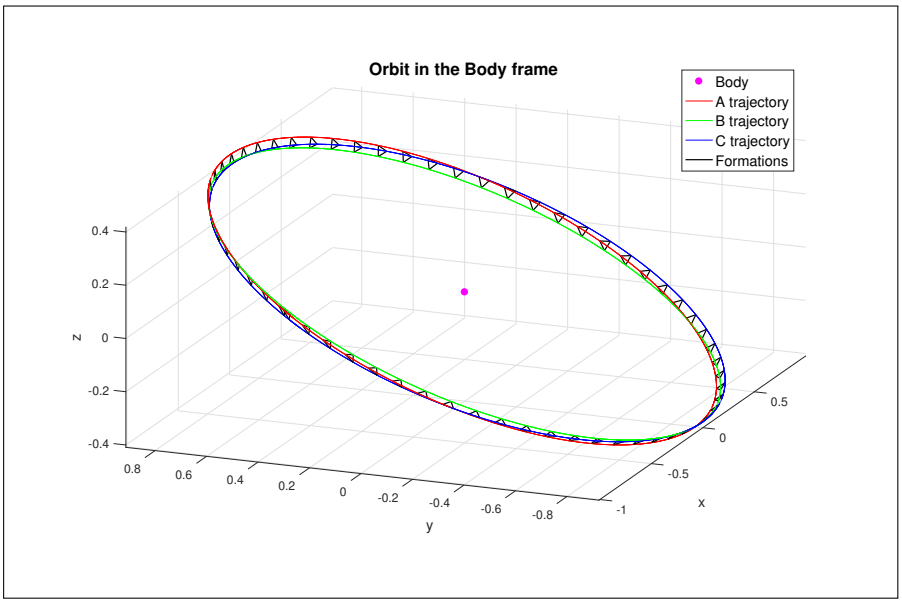

Figure 3.16: Trajectory of an unperturbed LISA formation of arm length $6AU$ in an inertial frame

triangular one to simulate the initial placement of the LISA system from a circular parking orbit. Second, the rescaling of the formation to modify the length of the triangle's arms.

3.2.2.1 Transfer from trailing to triangle formation

We have seen in the previous section that particles sharing the same Keplerian circular orbit maintain identically a shape-invariant trailing formation. When setting up the LISA satellite system, it might be a good idea to first place all three spacecraft on a single circular orbit close to the intended orbit before placing them in the triangular formation.

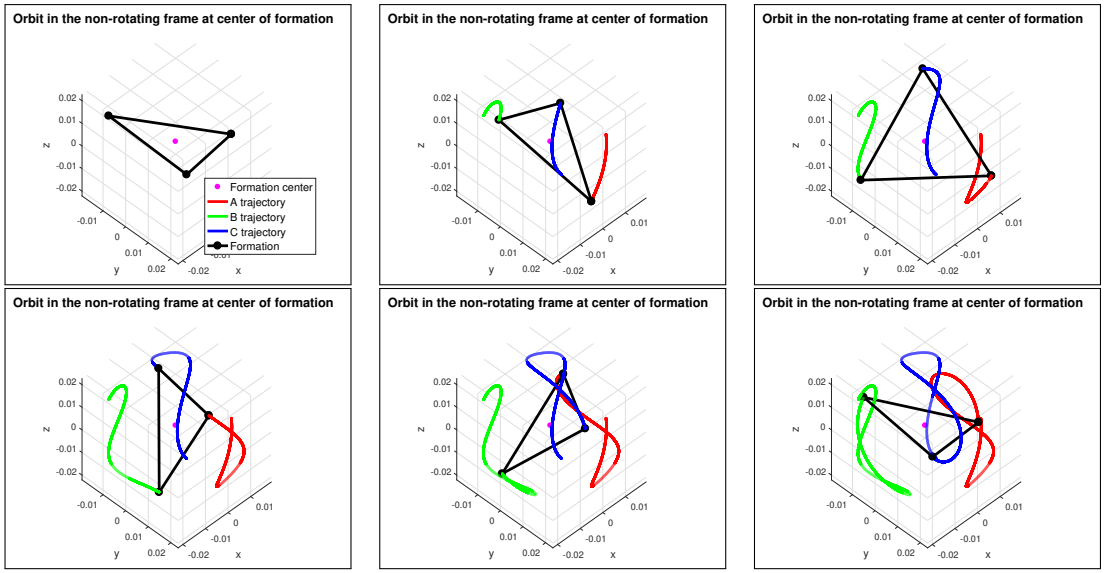

Figure 3.17: Evolution of the trajectory of an unperturbed LISA formation of arm length $6AU$ in the formation frame

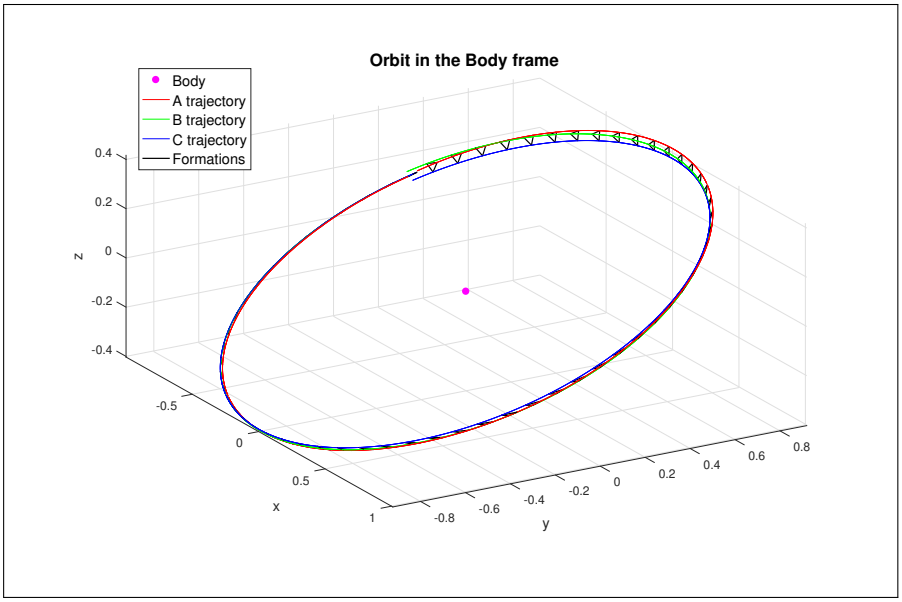

Figure 3.18: Trajectory of an optimal transfer form a circular trailing formation to a LISA formation of arm length $6AU$ in an inertial frame

Initially, particles are placed in a trailing formation on a circular orbit, successively offset by a constant angle. Figure 3.18 shows the reconfiguration of a three-particle formation from its initial state into a shape-invariant triangular configuration. Figure 3.19 shows this transfer in the formation frame.

3.2.2.2 Triangle reconfiguration

The sensitivity of the LISA sensor to gravitational waves of various wavelength is dependent on the arm length of its triangular formation. It is therefore useful to develop a controller enabling the reconfiguration of the formation between triangles of different scales. In this example, we reconfigure the LISA formation

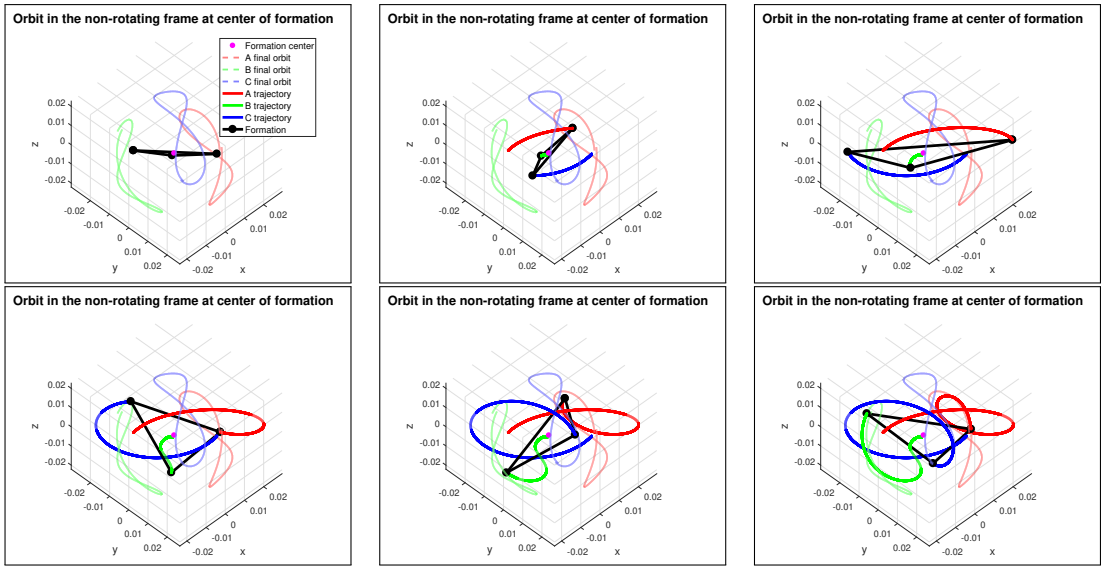

Figure 3.19: Evolution of the trajectory of an optimal transfer form a circular trailing formation to LISA formation of arm length $6AU$ in the formation frame

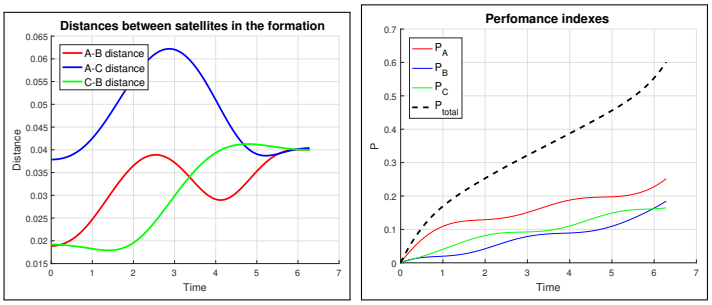

Figure 3.20: Evolution of the distances between satellites and performance indices during an optimal transfer form a circular trailing formation to LISA formation of arm length $6AU$

in order to achieve a triangular configuration six times larger than the initial. Figure 3.22 shows the transfer of each particle from its initial 8-shaped orbit to the larger final one in the formation frame. The same reconfiguration is displayed in an inertial frame on Figure 3.21.

Figure 3.23 informs us that the triangular formation is not maintained throughout the reconfiguration manoeuvre, as the distances between the particles are equal at the beginning and end of the transfer, but not in between. This is not surprising, as every particle is controlled independently on a trajectory that minimizes its cost in terms of fuel spent, only the initial and final positions can be specified.

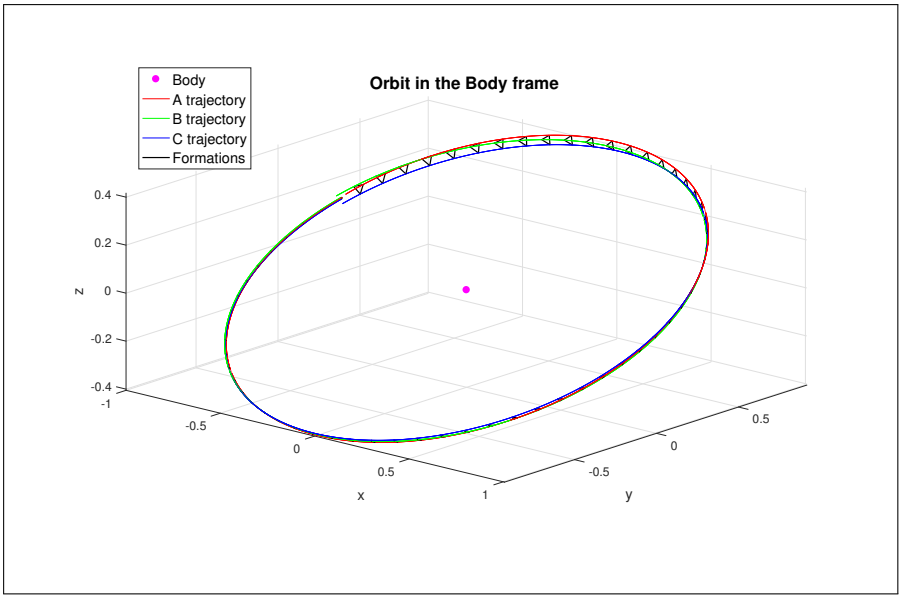

Figure 3.21: Trajectory of an optimal transfer between LISA formations of different arm lengths in an inertial frame

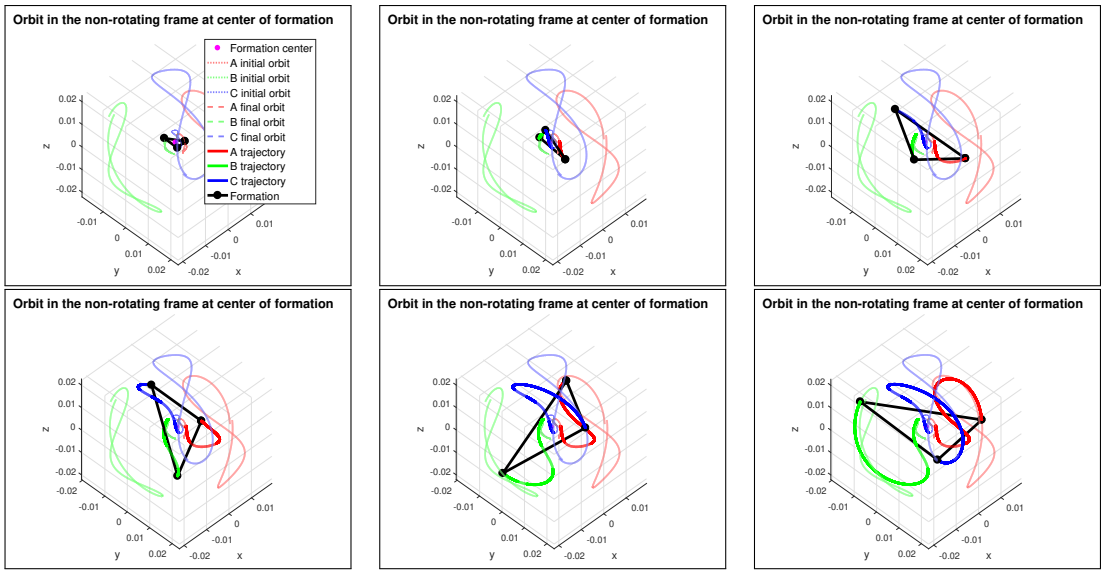

Figure 3.22: Evolution of the trajectory of an optimal transfer between LISA formations of different arm lengths in the formation frame

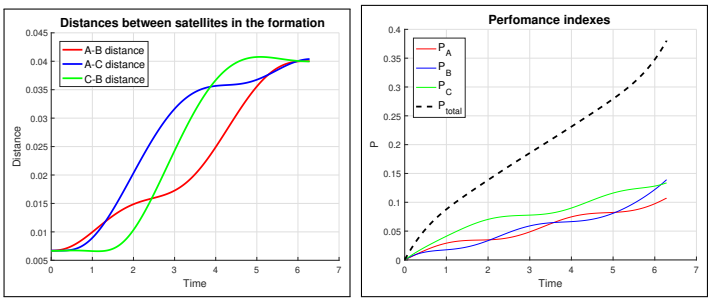

Figure 3.23: Evolution of the distances between satellites and performance indices during an optimal transfer between LISA formations of different arm lengths

3.3 Cooperative control

The optimal control scheme introduced in Chapter 2 has a number of disadvantages when applied to formation flying problems. Common features of distributed systems include simple reactive behaviour and robustness to unexpected perturbations. We have seen in Section 3.2 that using an optimal controller on a formation reconfiguration task involves either controlling each particle independently in a fully decentralized way or the entire formation jointly. Either way, the control is applied in open-loop, so errors in the final state are likely to appear in realistic applications. Moreover, the optimization process described in Section 2.1 is computationally expensive and would likely have to be performed on a ground station and the resulting control sequence communicated to the satellite.

In this section, we will introduce an alternative autonomous feedback controller that, though suboptimal in terms of fuel costs, is robust, cooperative and scalable. We will first present the theoretical background and design method for this cooperative controller. Then, the task of formation reconfiguration and maintenance similar to the ones in Section 3.2.1 will be solved to compare it to the optimal controller.

3.3.1 Theory

Consensus dynamics is a discipline at the intersection of systems theory and graph theory [7]. It involves nodes of a network exchanging information with their neighbours to reach an agreement in their states. The formation is represented by a directed graph, where nodes represent satellites and edges are communication links between them. In order for the method to be scalable, the formation graph should not be complete. This is especially true for satellite systems, where maintaining a communication link between every pair of satellites in a large formation would constitute a significant load on the limited communication capacity of individual satellites. The *adjacency matrix* E of the formation graph assigns connections between members of the network. For large formations, the adjacency matrix is usually sparse, as every satellite is generally assigned only a handful of neighbours, with every particle tasked with reaching consensus only with its immediate neighbourhood. With the adjacency matrix and the *degree matrix* D (diagonal matrix indicating the number of connections of each node), the graph Laplacian matrix can be calculated:

$$L = D - E \tag{3.6}$$

The dynamics of particle i of the formation generally can be written as

$$\dot{\boldsymbol{x}}_i = f\left(\boldsymbol{x}_i\right) + g\left(\boldsymbol{x}_i\right)\boldsymbol{u}_i \tag{3.7}$$

where $f\left(\boldsymbol{x}_i\right)$ is its uncontrolled dynamics and $\boldsymbol{u}_i$ the control input vector. The above dynamics can be simplified by assuming the control-state coupling independent on the current state $g\left(\boldsymbol{x}_i\right) = B$.

As we only consider linear distributed control, the design of which is based mainly on linear time-invariant dynamics, we linearize the dynamics:

$$f\left(\boldsymbol{x}_i\right) = A\boldsymbol{x}_i + h\left(\boldsymbol{x}_i\right) \tag{3.8}$$

where $h(\boldsymbol{x}_i)$ are the higher order non-linear terms that are omitted for purposes of design. The system matrix is obtained from the Jacobian of the dynamics $A = \frac{\partial f(\boldsymbol{x})}{\partial \boldsymbol{x}}$. For the equations of motion (1.30) in the Keplerian system (derived in Section 1.3.1), the state matrix is as follows:

$$A = \begin{bmatrix} 0 & 1 & 0 & 0 & 0 & 0 \\ {x_6}^2 \sin^2 x_3 + \frac{2}{x_1^3} + x_4^2 & 0 & x_1 x_6^2 \sin(2x_3) & 2x_1 x_4 & 0 & 2x_1 x_6 \sin^2 x_3 \\ 0 & 0 & 0 & 1 & 0 & 0 \\ \frac{2x_2 x_4}{x_1^2} & -\frac{2x_4}{x_1} & x_6^2 \cos(2x_3) & -\frac{2x_2}{x_1} & 0 & x_6 \sin(2x_3) \\ 0 & 0 & 0 & 0 & 0 & 1 \\ \frac{2x_2 x_6}{x_1^2} & -\frac{2x_6}{x_1} & \frac{2x_4 x_6}{\sin^2 x_3} & -\frac{2x_6 \cos x_3}{\sin x_3} & 0 & -\frac{2x_2}{x_1} - \frac{2x_4 \cos x_3}{\sin x_3} \end{bmatrix} \tag{3.9}$$

By aligning the frame of reference with the orbital plane, we can simplify the relation:

$$A = \begin{bmatrix} 0 & 1 & 0 & 0 & 0 & 0 \\ \frac{2}{x_1^3} + x_6^2 & 0 & 0 & 0 & 0 & 2x_1 x_6 \\ 0 & 0 & 0 & 1 & 0 & 0 \\ 0 & 0 & -x_6^2 & -\frac{2x_2}{x_1} & 0 & 0 \\ 0 & 0 & 0 & 0 & 0 & 1 \\ \frac{2x_2 x_6}{x_1^2} & -\frac{2x_6}{x_1} & 0 & 0 & 0 & -\frac{2x_2}{x_1} \end{bmatrix} \tag{3.10}$$

As has been seen in Section 1.4.1, in a circular orbit states x_1, x_2 and x_6 remain constant, while only x_5 grows linearly. As A is independent of x_5, by linearising at a Keplerian circular orbit the system matrix is time-invariant.

State consensus can only be posed on homogeneous networks, where all nodes are governed by the same equations of motion. This is indeed true for all objects, natural and man-made, of negligible mass in a gravitational field, as the dynamics derived in Chapter 1 depends on the properties of massive bodies and states of the particles. Alternatively , in the case of heterogeneous networks, other techniques, such as output synchronization, can be applied.

As we explained above, we simplified the system to a linear time-invariant problem

$$\dot{\boldsymbol{x}}_i = A\boldsymbol{x}_i + B\boldsymbol{u}_i \tag{3.11}$$

The control input sufficient to achieve state consensus is

$$\boldsymbol{u}_i = cK\boldsymbol{e}_i \tag{3.12}$$

with c being a scalar gain, K a gain matrix and the local neighbourhood error

$$\boldsymbol{e}_i = \sum_j e_{ij} (\boldsymbol{x}_j - \boldsymbol{x}_i) \tag{3.13}$$

where e_{ij} is the element of the adjacency matrix indicating the presence of a communication link from i to j. The total controlled dynamics for the entire formation can be written in vector form:

$$\dot{\boldsymbol{x}} = (I_N \otimes A)\boldsymbol{x} + (I_N \otimes B)\boldsymbol{u} = (I_N \otimes A - cL \otimes BK)\boldsymbol{x} \tag{3.14}$$

where I_N is an identity matrix of size N - the number of nodes in the network, and $\otimes$ denotes the Kronecker product.

With the above-described control, all members of the formation will converge to a single, time-varying position, given by their share orbital dynamics. The

shape of this final orbit is however not specified and depends in general on initial conditions. To ensure the formation's final trajectory lies on the circular orbit around which we have linearised, we introduce a leader particle. This leader remains uncontrolled and serves to pin the formation to its orbit. Pinning is the action of letting information about the uncontrolled leader available to some nodes of the network [7]. A leader can be chosen among nodes of the network or it can be another object, real or virtual, the formation should converge to, like an asteroid we want to intercept. The only constraint with the choice of a leader is that it should have the same dynamics as the satellites of the formation. As we mentioned earlier, this holds true for all bodies in the gravitational field. If the leader is another spacecraft, it can be controlled by any other method. We can imagine a formation performing a coordinated orbit transfer with the leader deriving an optimal control sequence according to the method presented in Chapter 2 and the remaining satellites following autonomously. In order for the formation to converge to the leader, not all of its members have to be pinned by it, as long as this information propagates through the entire graph. We can introduce the diagonal pinning matrix G indicating which nodes of the network are attracted toward the leader. Just like with the adjacency matrix, the pinning matrix can be sparse. It is enough for only a few satellites to know the location of the leader for the whole formation to be pinned. The control of particles toward the leader is accomplished by adding a pinning term in the local neighbourhood error equation:

$$\boldsymbol{e}_i = \sum_j e_{ij} \left(\boldsymbol{x}_j - \boldsymbol{x}_i \right) + g_i \left(\boldsymbol{x}_0 - \boldsymbol{x}_i \right) \tag{3.15}$$

where $\boldsymbol{x}_0$ is the state vector of the leader and g_i indicate diagonal elements of the pinning matrix G.

The leader pinning can be added by shifting the states:

$$\boldsymbol{\delta} = \boldsymbol{x} - \mathbb{1} \otimes \boldsymbol{x}_0 \qquad \boldsymbol{\delta}_i = \boldsymbol{x}_i - \boldsymbol{x}_0 \tag{3.16}$$

The relation (3.14) can now include the pinning of the leader

$$\dot{\boldsymbol{\delta}} = \left(I_N \otimes A - c \left(L + G \right) \otimes BK \right) \boldsymbol{\delta} \tag{3.17}$$

We apply on (3.17) above the transformation T such that

$$T^{-1} \left(L + G \right) T = \Lambda \tag{3.18}$$

is upper triangular, with the eigenvalues of $(L + G)$ on its main diagonal. Then

$$\left(T^{-1} \otimes I_N \right) \left(I_N \otimes A - c \left(L + G \right) \otimes BK \right) \left(T \otimes I_N \right) = I_N \otimes A - c\Lambda \otimes BK \tag{3.19}$$

The stability of the total system is determined by the stability of the diagonal blocks in (3.19) having the form

$$A - c\lambda_j \left(L + G \right) \otimes BK \tag{3.20}$$

If all eigenvalues of $(L + G)$ are such that all such diagonal blocks are stable then the entire system is stable in a sense that it reaches synchronization to the leader's trajectory $\dot{\boldsymbol{x}}_0 = A\boldsymbol{x}_0$.

To ensure this, the matrix K is chosen as

$$K = R^{-1}B^T P \tag{3.21}$$

with P satisfying the Algebraic Riccati Equation:

$$A^T P + PA + Q - PBR^{-1}B^T P = 0 \tag{3.22}$$

where $Q = Q^T > 0$ and $R = R^T > 0$ are design parameters. With K chosen in this manner, the *synchronizing region*, the area of stability of the complex matrix pencil $A - \sigma BK$, is an unbounded right half-plane. The coupling gain c is chosen so as to push the eigenvalues $\lambda_j (L + G)$ into the synchronizing region:

$$\Re (c\lambda_i) > \frac{1}{2} \tag{3.23}$$

A cooperative controller for formation state consensus linearised around a circular leader trajectory designed according to the instructions above should make the entire formation converge toward the moving leader. The non-linearities of the system should be overcome by the feedback gain provided the particles' initial states are not too far from the linearised orbit. Particles approaching too close to a massive body might see their non-linear dynamics grow too large for the controller to handle and the cooperative stability might become compromised. On the other hand, particles moving too far from the body and the linearisation orbit are guaranteed not to fail.

A consensus controller such as described above is useful when contact or collision with the leader is desired. Often however, the required behaviour of a formation is maintaining a particular rigid shape, with stable distances between satellites, as explained in Section 3.1. In that section, particles sharing a common circular Keplerian orbit were proven to maintain such a shape-invariant formation. Indeed, when the reference frame is correctly aligned with the orbital plane, the Keplerian dynamics (1.30) become independent of the angular position x_5, meaning

$$f(\boldsymbol{x}_i) = f(\boldsymbol{x}_i + \delta\boldsymbol{x}_\varphi) \tag{3.24}$$

where $\delta\boldsymbol{x}_\varphi$ is an offset in the φ angle

$$\delta\boldsymbol{x}_\varphi = \begin{bmatrix} 0 \\ 0 \\ 0 \\ 0 \\ \Delta\varphi \\ 0 \end{bmatrix} \tag{3.25}$$

The local neighbourhood error vector (3.15) with the above offset becomes

$$\boldsymbol{e}_i = \sum_j e_{ij} \begin{bmatrix} x_{j1} - x_{i1} \\ x_{j2} - x_{i2} \\ x_{j3} - x_{i3} \\ x_{j4} - x_{i4} \\ x_{j5} - x_{i5} + \Delta\varphi_{ij} \\ x_{j6} - x_{i6} \end{bmatrix} + g_i \begin{bmatrix} x_{01} - x_{i1} \\ x_{02} - x_{i2} \\ x_{03} - x_{i3} \\ x_{04} - x_{i4} \\ x_{05} - x_{i5} + \Delta\varphi_{i0} \\ x_{06} - x_{i6} \end{bmatrix} \tag{3.26}$$

This allows to set arbitrary offsets between the nodes of the network as well as between them and the leader. The formation cooperatively controlled in this manner will converge toward the leader's orbit, on positions defined by their mutual offsets.

3.3.2 Trailing formation

3.3.2.1 Change in trailing angle in the Kepler system

In Section 3.2.1.1, a simple example of formation reconfiguration was introduced. Two particles, one leader and one follower, orbit a massive body on a shared circular orbit in a trailing formation. The reconfiguration manoeuvre involves the follower reducing its trailing angle with respect to the leader from an initial $\pi/2$ to $\pi/4$.

On Figures 3.24, 3.25 and 3.26 the same task is performed using the feedback controller described in Section 3.3.1. With only one follower, its control input is calculated only from the leader's pinning, with adjacency and pinning matrices

$$A = [0] \qquad G = [1] \tag{3.27}$$

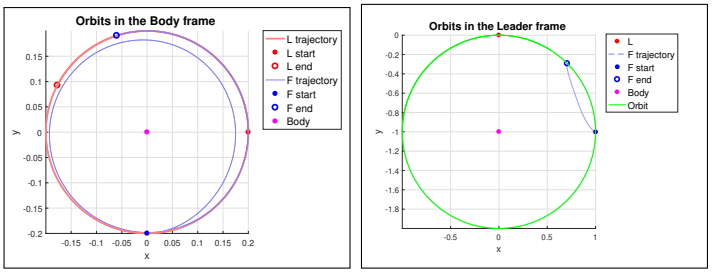

Figure 3.24: Trajectory of a cooperative formation reconfiguration manoeuvre changing the trailing angle

The shape of the transfer orbit employed by the follower particle in order to perform the desired reconfiguration is similar as in the case where the optimal controller was used (Figure 3.2). The particle plunges towards the body in order to gain angular velocity and catch up to the leader, before regaining its goal position on the formation orbit.

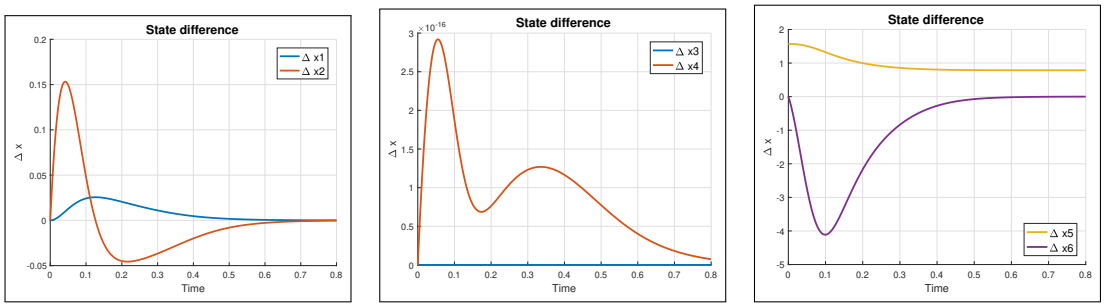

Figure 3.25: Differences in states between the leader and follower particles during a cooperative formation reconfiguration manoeuvre changing the trailing angle

Inspection of the figures comparing the states of the two particles (Figure 3.25) reveal the follower approaches its goal state asymptotically, as it is the case with

continuous feedback controllers. Another feature of proportional feedback control is that the controlled input applied is proportional to the difference in states from a goal position, given by Equation (3.15). As a result, the control amplitude is maximal at the beginning of the manoeuvre and diminishes to zero as the particle approaches its final position in the formation (Figure 3.26). This causes the performance index, calculated according to Equation (2.2), to increase rapidly at the beginning before settling as control is attenuated. In the optimally controlled scenario, the control input was applied more evenly (Figure 3.4), as a result the performance index grew gradually.

It is also notable that if the initial states of the follower are in the leader's orbital plane, the entire transfer will be performed in this plane due to the differences in states x_4 and x_5 (the polar angular states) being zero. We will therefore not display any more the values of those states in the subsequent examples.

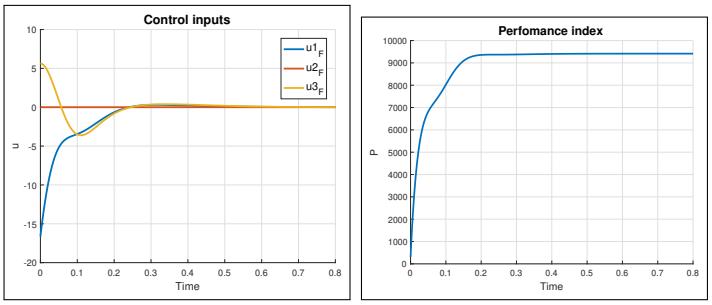

Figure 3.26: Applied control inputs and performance indices during a cooperative formation reconfiguration manoeuvre changing the trailing angle

Comparing the cost of the reconfiguration manoeuvre in terms of the performance index for both types of controllers solving the same task reveals the optimal open-loop method is about 13 times cheaper. This difference is attributed in part to the fact the performance index (2.2) is calculated using the square of control inputs, thus penalizing short peaks in amplitude such as those seen on Figure 3.26. Mostly however, it is due to the fact that optimal control is designed to find trajectories that minimize the control applied. The used feedback controllers, on the other hand, do not make any effort in this direction.

3.3.2.2 Cooperative reconfiguration

As explained in Section 3.3.1, the cooperative controller introduced enables the convergence of a numerous formation of satellites while keeping communication costs low. In this example, we will show a coordinated reconfiguration manoeuvre, where a network of four satellites in a trailing circular formation is tasked with changing their mutual trailing angles. To maintain as few communications links as possible, the formation is set up in such a way that every member synchronizes with only one other, or expressed in terms of adjacency and pinning matrices

$$A = \begin{bmatrix} 0 & 0 & 0 \\ 1 & 0 & 0 \\ 0 & 1 & 0 \end{bmatrix} \qquad G = \begin{bmatrix} 1 \\ 0 \\ 0 \end{bmatrix} \tag{3.28}$$

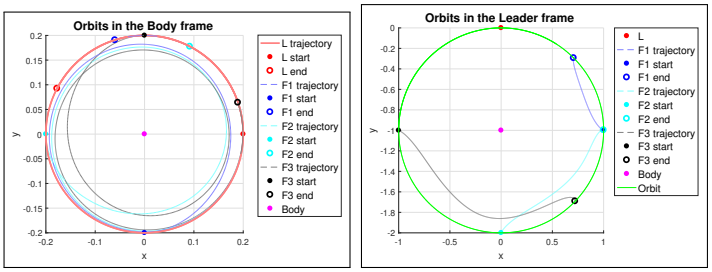

Figure 3.27: Trajectory of a cooperative formation reconfiguration manoeuvre changing the trailing angle

meaning the first follower is only pinned by the leader as in the previous example, the second tries to achieve consensus with the first and the third with the second.

Figure 3.27 and 3.28 show that in the initial state, the formation is shape-invariant on a shared circular orbit with the leader, trailing mutually by $\pi/2$. During the reconfiguration, all three particles move closer to the body to get closer to the leader, as explained in the previous examples, before returning to the leader's orbit on positions determined by the desired final offset $\pi/4$.

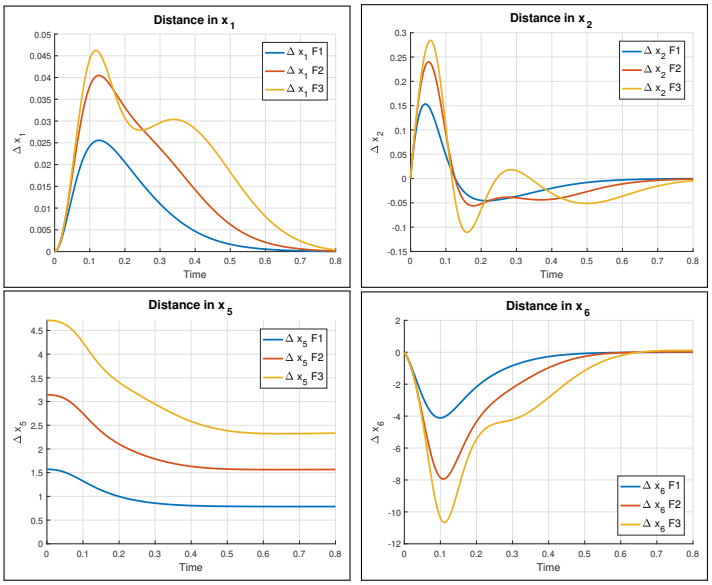

Figure 3.28: Differences in states between the leader and follower particles during a cooperative formation reconfiguration manoeuvre changing the trailing angle

The last follower clearly spends the most fuel in its manoeuvre (Figure 3.29), as the distance between its initial and final state relative is the greatest, as confirmed by the orbit trajectory graph in the leader frame. Because of the structure of the communication network, all followers must wait for their neighbours to stabilize first before being able to reach their steady states. This causes the third follower to attain its finals state as last.

3.3.2.3 Swap follower positions

In Section 3.2.1.2, the trajectories of two particles were jointly optimized to exchange their mutual positions on a circular orbit. The same manoeuvre can be performed in the cooperative scheme. Starting with the final configuration from

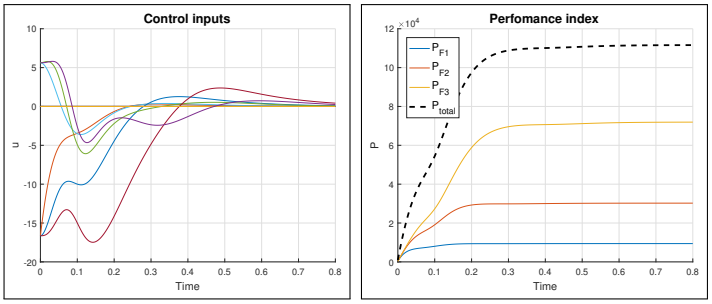

Figure 3.29: Applied control inputs and performance indices during a cooperative formation reconfiguration manoeuvre changing the trailing angle

the last example, four satellites on the same circular orbit mutually offset by $\pi/2$, the two last followers are tasked with exchanging positions.

This reconfiguration cast is performed very easily by swapping reassigning the satellite's indices in the adjacency and pinning matrices (3.28). The third follower's steady state position will be offset with regard to the first follower F_1, not F_2. Similarly, the second follower will try to reach a position offset from $F3$ instead of F_1. This swap manoeuvre is depicted on Figures 3.30, 3.31 and 3.32.

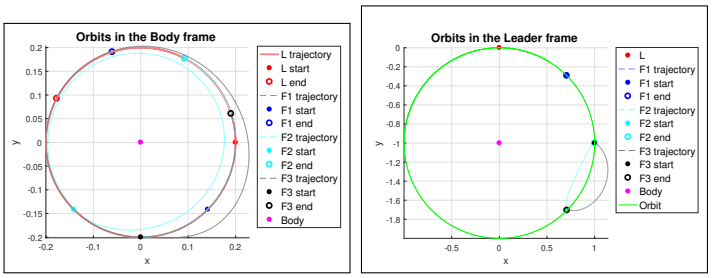

Figure 3.30: Trajectory of a cooperative formation reconfiguration manoeuvre swapping two follower positions

In the case the optimal controller is used, we noticed how the increasing the trailing angle is cheaper in terms of performance index than decreasing it. Using cooperative control, the opposite is true, as indicated by Figure 3.32. As we explained earlier, the control input magnitude is proportional to the error in states and decreases as the goal state is approached. For the follower F_2, the initial angular error is $\pi/4$. For F_3, it is $\pi/2$ however, leading to a stronger initial control thrust. If additional communication links were added to the network, the transition might be smoother, as the satellite at the tail of the formation would be less sensitive to initial errors in the formation configuration.

3.3.2.4 Compensate for perturbations in the Hill's system

One of the perks of feedback control systems is their robustness to unmodelled perturbations. And, contrary to the optimal controller (Section 3.2.1.3), it should be able to track a desired state continuously, instead of just ensuring it is reached after some time T. The result of a formation maintenance task using a cooperative controller on the above described trailing formation is shown on Figures 3.33, 3.34 and 3.35. As in Section 3.2.1.3, perturbations from the presence of the second body and the oblateness of the principal are included with the same values

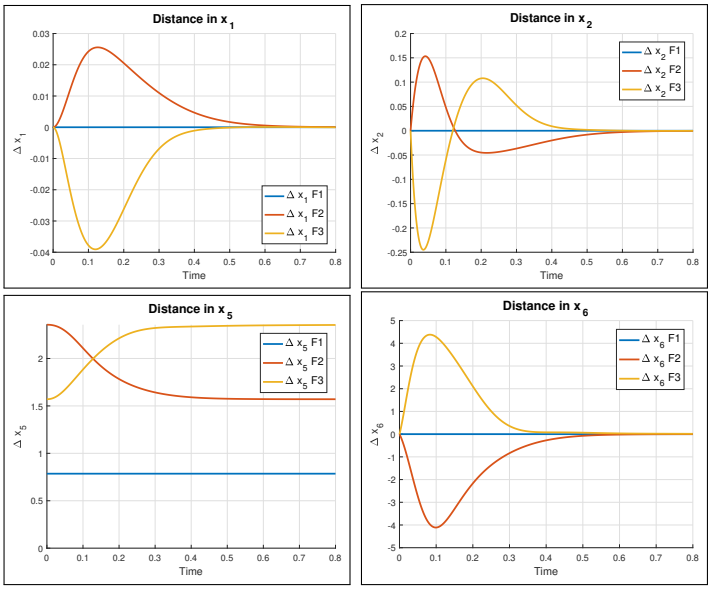

Figure 3.31: Differences in states between the leader and follower particles during a cooperative formation reconfiguration manoeuvre swapping two follower positions

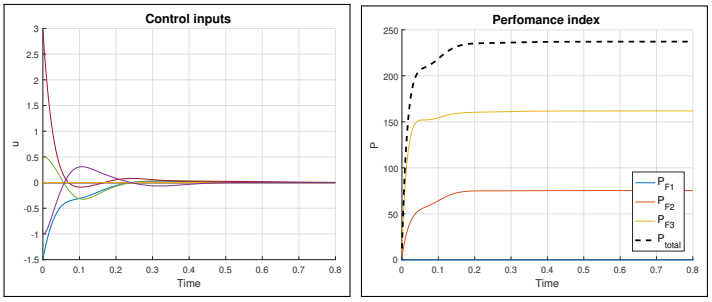

Figure 3.32: Applied control inputs and performance indices during a cooperative formation reconfiguration manoeuvre swapping two follower positions

of parameters (reduced mass $\mu = 0.15$ and oblateness parameter $a = 0.002$). The controller however remains linearised around a Keplerian circular orbit to demonstrate it can deal with precisions of the model. It is important to note that in the Hill's system, the shape-invariance condition (3.4) does not hold any more.

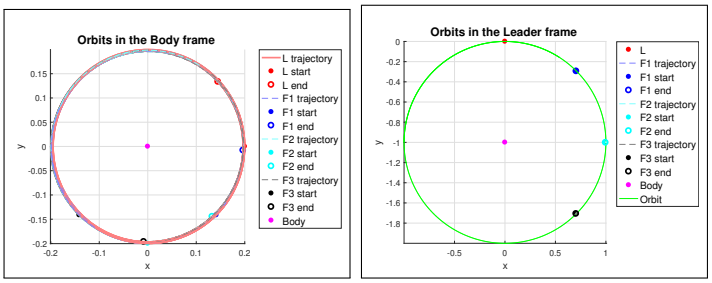

Figure 3.33: Trajectory of a cooperative formation maintenance manoeuvre

Contrary to the Keplerian model, dynamics in the Hill's system do not satisfy (3.24), as even if the orbit lies in the frame's principal plane

$$f(\boldsymbol{x}_i) \neq f(\boldsymbol{x}_i + \delta\boldsymbol{x}_\varphi) \tag{3.29}$$

This signifies that a trailing formation on a circular orbit is no longer stable. This is confirmed in this experiment, with follower satellites oscillating around their target positions. However, we consider the oscillations of low amplitude and the controller successful in maintaining the formation in place with an on average constant control input applied, as testified by the linearly growing performance index.

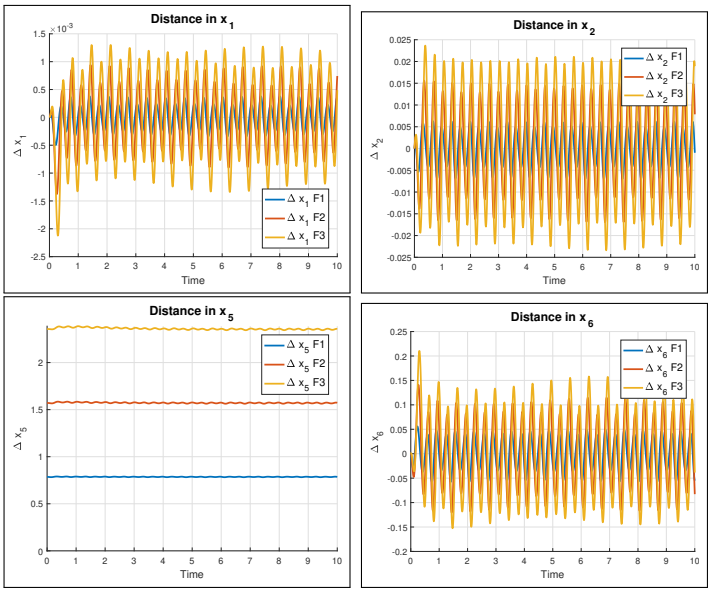

Figure 3.34: Differences in states between the leader and follower particles during a cooperative formation maintenance manoeuvre

Similarly to the last example, the last link in the trailing formation F_4 is perturbed the most, as deviations of all other particles accumulate. Indeed, the last follower's deviations from the target state have the highest amplitude, leading to more control input being spent on its maintenance.

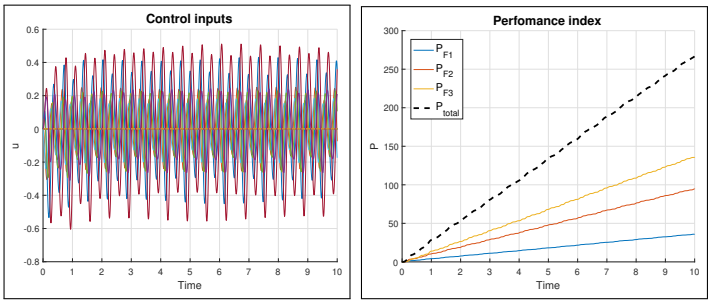

Figure 3.35: Applied control inputs and performance indices during a cooperative formation maintenance manoeuvre

3.3.2.5 Interception of a chaotic orbit

Section 1.4.4 presented the notion of chaotic orbits in the Hill's system. In Section 2.3.5, a transfer to one such orbit using an open-loop optimal control scheme was discussed. Chaotic trajectories are inherently difficult to predict, as arbitrary small errors in state measurement grow exponentially. This makes

open-loop techniques ill-suited for interception tasks, as they rely on their initial estimation of the future states of an object on a chaotic orbit. closed-loop methods however can continuously update their estimations of the target's position.

This experiment also serves to confirm if the controller derived in Section 3.3.1 is capable to make a formation converge to a leader position that does not lie on a circular orbit. The controller's parameters were however linearised around a Keplerian circular orbit. The linearization of the uncontrolled dynamics with the Jacobian (3.10) around the chaotic leader would result in a time-varying linear system. As the states of the chaotic orbit are heavily oscillating but bounded, we insert their average value (Figure 3.36) in the system matrix (3.10) to obtain an LTI system.

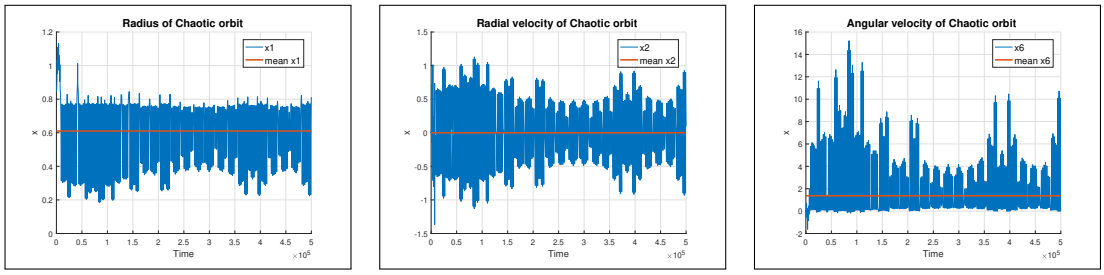

Figure 3.36: Variations in states x_1, x_2 and x_6 in a chaotic orbit

The communication graph of the formation has the same topology as before (3.28)

$$A = \begin{bmatrix} 0 & 0 & 0 \\ 1 & 0 & 0 \\ 0 & 1 & 0 \end{bmatrix} \qquad G = \begin{bmatrix} 1 \\ 0 \\ 0 \end{bmatrix} \tag{3.30}$$

with only the first satellite being pinned by the chaotic leader, and the other followers successively following it. As seen of Figure 3.37 and 3.38, the chaotic particle is cooperatively converged to by the formation.

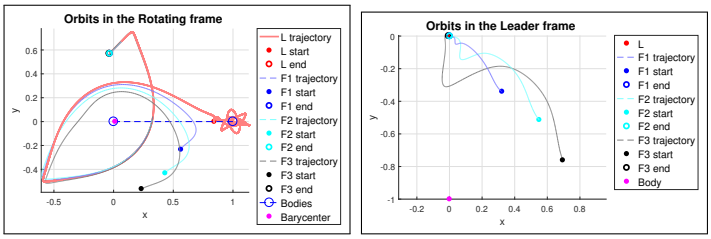

Figure 3.37: Trajectory of a cooperative interception manoeuvre

This example also shows the limits of the linearised control scheme. As the formation passes close to a massive body (around $t = 1.7$), the omitted non-linear terms of the uncontrolled dynamics grow in significance and perturb the converging particles. These non-linearities have to be compensated by a feedback control of higher amplitude than is necessary for reaching the chaotic leader itself (especially for the last follower F_3 that passes the closest to the body - Figure 3.39). Choosing a lower coupling gain c during the controller design might result in these non-linearities overcoming the linear controller and compromising

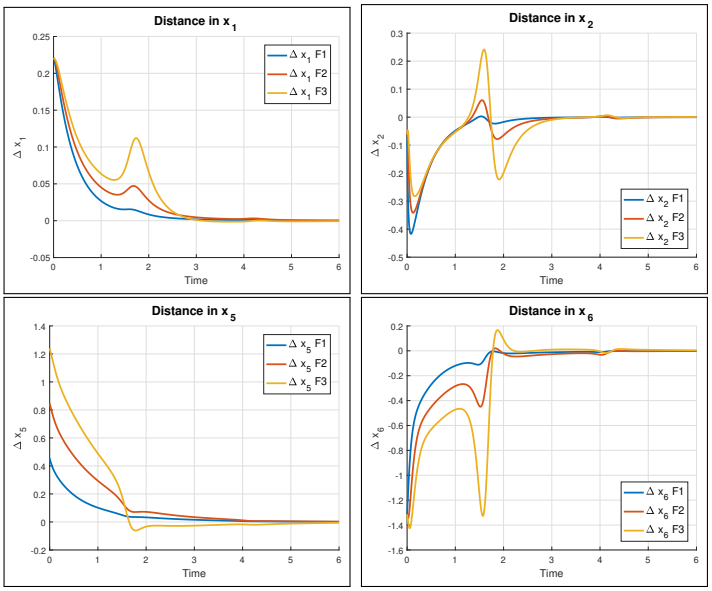

Figure 3.38: Differences in states between the leader and follower particles during a cooperative interception manoeuvre

the system's stability. On the other hand, a higher gain increases the system's robustness to these perturbations and enables a faster convergence toward the target, at a cost of higher amplitudes in the control inputs.

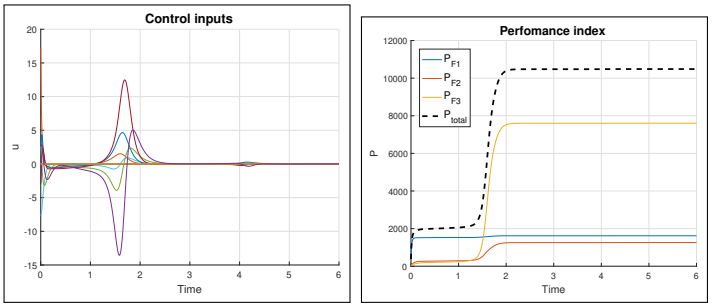

Figure 3.39: Applied control inputs and performance indices during a cooperative interception manoeuvre

The cooperative intercept of the asteroid on the chaotic orbit is also of particular practical importance. The close-Earth passing asteroid usually orbit on chaotic trajectories and the developments presented in this section relate to any formation mission that would involve such a body as its target. We showed the capability of the autonomous system of space-borne crafts to cooperatively converge to the position of such an object even if it is being tracked by only some of the crafts.

3.4 Conclusion

Satellite formation flying is a new field of space engineering studying multi-agent formations of satellites working in cooperation to achieve a given task. It has many potential advantages over single-satellite solutions but comes at the price of having to design a control scheme for formation setup, maintenance and reconfiguration.

In this chapter, two alternative controller solutions were discussed. The first applied the principles of optimal control introduced in Chapter 2 to solve various reconfiguration problems in a trailing and LISA formation (in in Section 3.2). It achieved its goal efficiently but has shown to be sensitive to unmodelled perturbations and not well scalable.

An alternative closed-loop cooperative controller was designed in Section 3.3. With the design linearised around a certain circular orbit, it had to compensate for known non-linearities instead of fully embracing them. With an increased control cost compared to the optimal controller, this cooperative one has however significant advantages. Using feedback enables to compensate for unexpected perturbations and allows to continuously track a goal state position. Its reduced complexity and robustness to incomplete information indicates it could more easily be performed onboard, without relying on ground stations. Plus, by limiting the communications links between members of the formation, scalability can be ensured and large groups of satellites can be controlled autonomously.

Conclusion

The design of controller of satellites is a crucial aspect of space engineering since the very beginning of this field. Constraints in fuel supply, communication and computation capacities together with the impossibility of resupply or maintenance of most satellite systems leads to the need for highly robust and efficient controllers.

Before designing the controllers, the dynamics of uncontrolled bodies in a gravitational field were thoroughly analysed in Chapter 1. Using the tools of Lagrangian mechanics introduced in Section 1.2, perturbation from the oblateness of the central body and the presence of a second mass where added to the basic Keplerian model in Section 1.3. Orbital trajectories were presented in Section 1.4 to demonstrate the variety of solutions to the non-linear equations of motion.

This thesis aimed at comparing two control approaches for satellite formation reconfiguration and maintenance task. The optimal controller presented in Chapter 2 is an open-loop method attempting to minimize the control input applied during the manoeuvre. It can serve as a benchmark for other approaches, giving an idea of a lower bound on the required control input cost of a transfer. Open-loop approaches are however sensitive to unmodelled disturbances and cannot be used on continuous formation keeping tasks. The cooperative control approach introduced in Section 3.3, on the other hand uses, feedback to compensate for perturbations and maintain a desired formation configuration. The simplicity of this close-loop control scheme indicates it could be more easily performed autonomously on-board using only local information. Its inability to make predictions based on its of knowledge of the dynamics model makes it inefficient, especially if the goal state is far from the initial.

A combination of both techniques would allow to make use of strengths of both while bypassing their weaknesses. In an initial phase, the formation is approached to its target position with a precomputed cost-efficient optimal manoeuvre. The inevitable unexpected perturbations will accumulate and introduce an error in the end state. This deviation can be autonomously corrected by the cooperative feedback controller, which might also take care of subsequently maintaining the final formation in place or perform any small reconfiguration task.

Future work

Throughout this thesis, a few issues and experiments have been omitted or only hinted at due to scope restrictions. We will summarise below what we think are the most interesting problems related to this thesis that are worth a deeper examination.

- **Dynamics in elliptic Hill's system**.

  In Section 1.3.4, we derived the equations of motion of a particle in the gravitational field of two masses revolving around each other on elliptic trajectories. We did not expand on this problem by performing simulations in this system or designing a controller as was done for the circular Hill's model.

- **Deformation of bodies**.

  The perturbations arising from the oblateness of the central body were discussed in Section 1.3.2. The inclusion of higher terms of the Legendre polynomial expansion (1.32) could increase the accurateness of modelling particular celestial bodies.

  When merging the perturbation model for an oblate body with the Hill's system, a simplifying assumption was made that the polar axis of the body is perpendicular to the principal plane. In reality, the tilt of planets of the Solar system is not specified in this way [11]. Reconciling this inclination with the rotating frame would also allow to more precisely model known celestial objects.

  On the other hand, small bodies orbiting close to larger ones often experience tidal locking. When tidally locked, the body's rotation speed is synchronized with its revolution, meaning it always faces the large mass with the same hemisphere. Often, those bodies are deformed by *prolateness*, the stretching of a sphere at its poles. This deformation can easily be modelled in the Hill's system, as its orientation is aligned with the principal axis. In the Solar system, most major moons, including the Earth's, are tidally locked to their planets, as well as Mercury with regard to the Sun [4].

- **Free-time optimal control**

  The optimal controller introduced in Chapter 2 used a fixed-time control scheme, meaning the total time T of the transfer is set in advance as a parameter of the controller. If the control is designed as free-time, the final time is not set in advance any-more. The performance index (2.2) does not only include the control inputs but also a time component, such as to optimize jointly a trade-off between the time of transfer and control costs.

- **Cooperative and optimal control in orbital parameters**

  The coordinate system used in our models was chosen spherical, as it allows to express circular orbits in the frame's principal plane with five constant and only one varying state. Expressing the dynamics in terms of orbital elements [1] would enable to express any Keplerian orbit with five stable parameters and the varying true anomaly. The disadvantage of this approach would be a more complicated, possible time-variant, set of equations of motion, making the controller design also harder

Appendix

CD Content

In table 3.4 are listed names of all root directories on the enclosed CD.

Directory name	**Description**
Satellite formation flight: optimal and cooperative control approaches.pdf	Master thesis in pdf format
Matlab Scripts	Matlab scripts used in this thesis
Simulink Models	Simulink models used in this thesis
readme.txt	text file with additional instructions

Table 3.4: Enclosed CD content

Bibliography

[1] J.M.A. Danby. *Fundamentals of celestial mechanics*. Macmillan, 1962.

[2] H. Goldstein, C.P. Poole, and J.L. Safko. *Classical Mechanics*. Addison Wesley, 2002.

[3] Daniel Grebow. Generating periodic orbits in the circular restricted three-body problem with applications to lunar South Pole coverage. Master's thesis, Purdue University, West Lafayette, Ind, USA, 2006.

[4] René Heller, Jérémy Leconte, and Rory Barnes. Tidal obliquity evolution of potentially habitable planets. *Astronomy & Astrophysics - ASTRON ASTROPHYS*, 528, 01 2011.

[5] H. Kwakernaak and R. Sivan. *Linear optimal control systems*. Wiley-Interscience publication. Wiley Interscience, 1972.

[6] F.L. Lewis. *Optimal control*. A Wiley-Interscience publication. Wiley, 1986.

[7] Frank L. Lewis, Hongwei Zhang, Kristian Hengster-Movric, and Abhijit Das. *Cooperative Control of Multi-Agent Systems: Optimal and Adaptive Design Approaches*. Springer Publishing Company, Incorporated, 2014.

[8] W.D. McClain and D.A. Vallado. *Fundamentals of Astrodynamics and Applications*. Space Technology Library. Springer Netherlands, 2001.

[9] F.R. Moulton. *An introduction to celestial mechanics*. The Macmillan company, 1935.

[10] Carl D. Murray and Stanley F. Dermott. *Solar System Dynamics*. Cambridge University Press, 1998.

[11] United States Naval Observatory. Nautical Almanac Office. *Astronomical Almanac for the Year 2010 and Its Companion, the Astronomical Almanac Online*. ASTRONOMICAL ALMANAC FOR THE YEAR. U.S. Government Printing Office, 2009.

[12] Graeme L. Stephens, Deborah G. Vane, Ronald J. Boain, Gerald G. Mace, Kenneth Sassen, Zhien Wang, Anthony J. Illingworth, Ewan J. O'connor, William B. Rossow, Stephen L. Durden, Steven D. Miller, Richard T. Austin, Angela Benedetti, Cristian Mitrescu, and the CloudSat Science Team. The cloudsat mission and the a-train. *Bulletin of the American Meteorological Society*, 83(12):1771–1790, 2002.

[13] Gang Wang and Wei-Tou Ni. Numerical simulation of time delay interferometry for elisa/ngo. *Classical and Quantum Gravity*, 30(6):065011, 2013.